

*Digital Comprehensive Summaries of Uppsala Dissertations
from the Faculty of Science and Technology 2348*

Modeling Vibrational Electron Energy Loss Spectroscopy with the Frequency- Resolved Frozen Phonon Multislice Method

PAUL MICHEL ZEIGER



ACTA UNIVERSITATIS
UPSALIENSIS
2024

ISSN 1651-6214
ISBN 978-91-513-1987-2
urn:nbn:se:uu:diva-517225



UPPSALA
UNIVERSITET

Dissertation presented at Uppsala University to be publicly examined in Högssalen (10132), Ångströmlaboratoriet, Lägerhyddsvägen 1, Uppsala, Friday, 2 February 2024 at 09:15 for the degree of Doctor of Philosophy. The examination will be conducted in English. Faculty examiner: Associate Professor Rebecca Nicholls (University of Oxford).

Abstract

Zeiger, P. M. 2024. Modeling Vibrational Electron Energy Loss Spectroscopy with the Frequency-Resolved Frozen Phonon Multislice Method. *Digital Comprehensive Summaries of Uppsala Dissertations from the Faculty of Science and Technology* 2348. 119 pp. Uppsala: Acta Universitatis Upsaliensis. ISBN 978-91-513-1987-2.

Aberration correctors, improved monochromators, and better detectors have enabled exciting research with nanometer- and Ångström-scale resolution in the Scanning Transmission Electron Microscope (STEM). However the interaction of high-energy electrons with the many-body system of the sample is quite complex and hinders interpretation of experiments. Therefore measurements often need to be informed by extensive modeling of the beam-sample interaction.

In this thesis, we report the development of a model for the computer simulation of vibrational Electron Energy Loss Spectroscopy (EELS) in the STEM, which we call the Frequency Resolved Frozen Phonon Multislice (FRFPMS) method. We motivate the development of the method by reviewing the field of vibrational EELS from the instrumental advances, which enabled it, over experimental progress to a detailed consideration of other theories of vibrational EELS. In the process, we identify the need for a method, which is able to take into account many of the complicating factors of the scattering process, such as multiple elastic interactions, and is computationally feasible today, even for extended structure models.

After a brief overview of necessary computational methods, we showcase that the FRFPMS method satisfies this need by discussing several papers we have published on the method. We demonstrate that the FRFPMS method produces results, which agree very well with published experimental and also theoretical results, both for momentum-resolved as well as high spatial resolution vibrational EELS. Furthermore we compare the FRFPMS method with the Quantum Excitations of Phonons model and the first-order Born approximation for a simple model system. The FRFPMS method matches the predictions of the other theories provided that two small modifications are introduced, which modify the temperature and energy-loss dependent scaling as well as the large momentum-transfer behavior of the modelled cross section.

We then apply such *revised* FRFPMS method to simulations of shifts of optical phonon frequencies in hBN as a function of isotopic composition. The FRFPMS results are in very good agreement with experiments performed by collaborators, demonstrating that vibrational EELS is capable of detecting such isotopic shift of phonon frequencies in a momentum-resolved fashion. In another application of our method we focus on simulating atomically-resolved STEM-EELS experiments on SrTiO₃, which allow to interpret a subtle asymmetry in experimental large detector off-axis vibrational STEM-EELS maps as result of sensitivity to the direction of the phonon eigenvector. This enables imaging of anisotropic displacements of atoms as a function of vibrational frequency.

Keywords: Electron Energy Loss Spectroscopy, Phonons, Scanning Transmission Electron Microscopy, Frozen Phonon Multislice, Molecular Dynamics

Paul Michel Zeiger, Department of Physics and Astronomy, Materials Theory, Box 516, Uppsala University, SE-751 20 Uppsala, Sweden.

© Paul Michel Zeiger 2024

ISSN 1651-6214

ISBN 978-91-513-1987-2

URN urn:nbn:se:uu:diva-517225 (<http://urn.kb.se/resolve?urn=urn:nbn:se:uu:diva-517225>)

To my family and friends

To everyone who will find this text useful

To all microscopists pushing the boundaries of what we can see

List of papers

This thesis is based on the following papers, which are referred to in the text by their Roman numerals.

- I P. M. Zeiger and J. Ruzs, "Efficient and Versatile Model for Vibrational STEM-EELS", *Physical Review Letters* **124**, 025501 (2020)
- II P. M. Zeiger and J. Ruzs, "Frequency-resolved frozen phonon multislice method and its application to vibrational electron energy loss spectroscopy using parallel illumination", *Physical Review B* **104**, 104301 (2021)
- III P. M. Zeiger and J. Ruzs, "Simulations of spatially and angle-resolved vibrational electron energy loss spectroscopy for a system with a planar defect", *Physical Review B* **104**, 094103 (2021)
- IV P. M. Zeiger, J. Barthel, L. J. Allen and J. Ruzs, "Lessons from the harmonic oscillator: Reconciliation of the frequency-resolved frozen phonon multislice method with other theoretical approaches", *Physical Review B* **108**, 094309 (2023)
- V P. Zeiger, J. Hachtel, D. Legut, E. Janzen, J. Barthel, J. H. Edgar, L. J. Allen, J. Ruzs, "Control of the phonon band gap with isotopes in hexagonal boron nitride", *arXiv:2302.13415* (2023)
- VI X. Yan, P. M. Zeiger, Y. Huang, H. Sun, J. Lie, C. A. Gadre, H. Yang, R. He, T. Aoki, Z. Zhong, Y. Nie, R. Wu, J. Ruzs, and X. Pan, "Real-Space Visualization of Frequency-Dependent Anisotropy of Atomic Vibrations", *arXiv:2312.01694* (2023)

Reprints were made with permission from the publishers.

Comments on my contributions to the papers

I was actively involved in conceiving all papers and the final form of all papers has been influenced by my own ideas. I performed all computations and wrote the core of the manuscript of paper I. I performed all of the MD simulations and part of the multislice simulations for papers II and III. I wrote the core of the text of paper II and shared writing of paper III with my coauthor. I performed most of the analytical work and all of the simulations for paper IV and wrote the entire manuscript with input from all coauthors. I performed all MD simulations for paper V and contributed to the writing of the manuscript. I conceived the band-pass filtering idea for paper VI, which enabled our FRFPMS calculations, and performed all MD simulations and the analysis of displacement ellipsoids. I was actively involved in the data analysis and interpretation and gave detailed input on the draft of the manuscript.

Declaration of transparency

This dissertation is based on the Licentiate thesis *The Frequency-resolved Frozen Phonon Method* by P. M. Zeiger, Uppsala University, 2021. All chapters have been edited and updated to varying extents. Chapter 1 has been updated with the newest state of vibrational EELS results. The discussion of theoretical approaches to EELS has been moved from chapter 1 to the new chapter 2 and is substantially expanded. The description of the Frozen Phonon multislice method has been moved from chapter 3 to chapter 2 and rewritten, but chapter 3 is otherwise largely unchanged. Chapters 4 and 5 were rewritten and extended in the light of new results. Chapters 6, 7, and 8 are new.

List of papers not included in this thesis

Apart from the papers included in this thesis, the author has contributed to the following papers and manuscripts:

- J. Barthel, P. Zeiger, J. Ruzs, L. J. Allen, "A simple model for phonon spectroscopy using fast electrons", submitted to *Physical Review B* (2023)
- J. Á. Castellanos-Reyes, P. Zeiger, A. Bergman, D. Kepaptsoglou, Q. M. Ramasse, J. C. Idrobo, and J. Ruzs, "Unveiling the impact of temperature on magnon diffuse scattering detection in the transmission electron microscope", *Physical Review B* **108**, 134435 (2023)
- J. Snarski-Adamski, A. Edström, P. Zeiger, J. Á. Castellanos-Reyes, K. Lyon, M. Werwiński, J. Ruzs, "Simulations of magnetic Bragg scattering in transmission electron microscopy", *Ultramicroscopy* **47**, 113698 (2023)
- K. Lyon, A. Bergman, P. Zeiger, D. Kepaptsoglou, Q. M. Ramasse, J. C. Idrobo, J. Ruzs, "Theory of magnon diffuse scattering in scanning transmission electron microscopy", *Physical Review B* **104**, 214418 (2021)
- D. Negi, P. M. Zeiger, L. Jones, J. C. Idrobo, P. A. van Aken, J. Ruzs, "Prospect for detecting magnetism of a single impurity atom using electron magnetic chiral dichroism", *Physical Review B* **100**, 104434 (2019)
- D. Pohl, S. Schneider, P. Zeiger, J. Ruzs, P. Tiemeijer, S. Lazar, K. Nielsch, B. Rellinghaus, "Atom size electron vortex beams with selectable orbital angular momentum", *Scientific Reports* **7**, 934 (2017)
- A. Löfgren, P. M. Zeiger, V. Kocovski, J. Ruzs, "Influence of nuclear quantum effects on frozen phonon simulations of electron vortex beam HAADF-STEM images", *Ultramicroscopy* **164**, 62 (2016)

Contents

1	Introduction	11
1.1	Basics of Electron Microscopy	11
1.2	Instrumental Advances	15
1.3	Key Experiments in Vibrational EELS	16
2	Theories of Phonon scattering for High-Energy Electrons	21
2.1	Dielectric formalism	21
2.2	The first-order Born approximation	22
2.3	Elastic scattering of high-energy electrons	26
2.4	The Frozen Phonon Multislice Method	29
2.5	The QEP model	31
2.6	Single inelastic scattering theories including multiple elastic scattering	32
2.7	Towards a new method for vibrational EELS	33
3	Simulation Methods	34
3.1	The Multislice Method	34
3.2	Molecular Dynamics Simulations	39
3.3	Phonon theory and calculations	43
4	Summary of Papers	48
4.1	Paper I: Proposal of the FRFPMS Method	48
4.2	Paper II: Details about the FRFPMS Method and Momentum-Resolved Simulations	51
4.3	Paper III: Defect Calculation with Nano- and Atomic-Size Beams	53
4.4	Paper IV: Lessons from the harmonic oscillator	54
4.5	Paper V: Isotope Effects in Momentum-Resolved Vibrational EELS	57
4.6	Paper VI: Imaging Vibrational Anisotropy	59
5	Conclusions and Outlook	63
6	Popular Science Summary	65
7	Populärvetenskaplig Sammanfattning	69
8	Populärwissenschaftliche Zusammenfassung	73
9	Acknowledgements	77

Bibliography	80
Acronyms	93
List of Natural Constants	95
Appendix A: Inelastic quantum mechanical scattering theory	96
Appendix B: Inelastic electron-matter scattering	99
Appendix C: First order Born approximation	101
Appendix D: Thermal averaging of the DDSCS	104
Appendix E: The DDSCS for a crystal	106
Appendix F: The Independent Atom Model	107
Appendix G: The DDSCS of a crystal in the IAM	110
Appendix H: Momentum transfer in z-direction	117
Appendix I: Derivation of MSD in classical statistical mechanics	118

1. Introduction

In this dissertation, we contribute a simulation method for vibrational Electron Energy Loss Spectroscopy (EELS) in the Scanning Transmission Electron Microscope (STEM), a relatively recent field within the broader electron microscopy research community. The main scientific work is thereby found in the attached papers I-V and the purpose of this text is not to reiterate those results in detail, but to reflect on the work that has been done and give additional insight and background information in an attempt to tell a complete and coherent story of the development of the Frequency-Resolved Frozen Phonon Multislice (FRFPMS) method. This dissertation is also intended to provide an introduction to any student or researcher, who wants to pick the FRFPMS method up for their own work.

To that end we have organized the text in the following way: we introduce basic concepts of STEM and the field of vibrational EELS in this chapter, chapter 1. In chapter 2, we give an overview of vibrational EELS theories and identify a need for the FRFPMS method. Chapter 3 deals with an explanation of the computational methods we have used to carry out FRFPMS calculations. Chapter 4 is then dedicated to the summary of what we have achieved and learnt about the FRFPMS method in each of the papers I-VI. We draw conclusions from this learning process in chapter 5 and outline possible future directions of research with and about the FRFPMS method. Last but not least, we summarize our work in a manner amiable to a general audience in chapters 6-8.

As hinted at above, we give in this chapter a *theorist's* overview of the basic principles of STEM in section 1.1, the instrumental developments, which enabled the field of vibrational EELS, in section 1.2, and a review of recent state-of-the-art experimental work in section 1.3.

1.1 Basics of Electron Microscopy

The Transmission Electron Microscope (TEM) was invented by Ernst Ruska and Max Knoll in 1931 in pursuit of greater spatial resolution than it is possible with light-based microscopies [1]. This came after the electron was shown to have wave character with De Broglie wavelength [2-5]

$$\lambda = \frac{h}{p}, \quad (1.1)$$

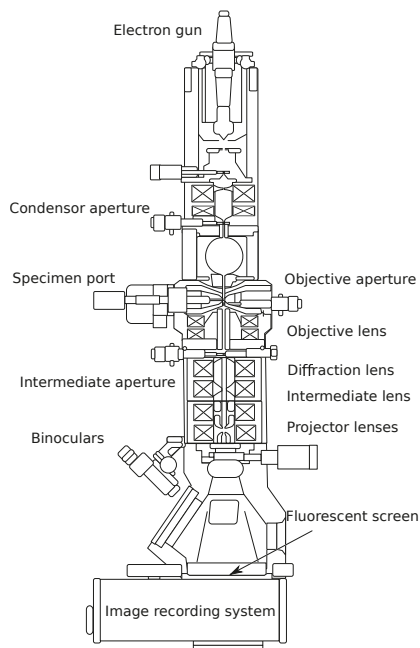


Figure 1.1. Schematic showing the main components of a STEM. Figure reprinted from Ref. [6].

where h is the Planck constant and p the momentum of the electron. The TEM leverages high-energy electrons through an intricate arrangement of electron optical elements to produce diffraction patterns or images of the specimen. Figure 1.1 displays a schematic of a TEM with many components explicitly labeled.

Adding the functionality of scanning the beam to build a STEM required more time to fully develop. In 1935 Max Knoll was the first to operate a machine using a scanning electron beam with a beam diameter of around $100\text{ }\mu\text{m}$ [7]. The first functional STEM was introduced by Manfred von Ardenne in 1938 [8, 9], which was, however, at the time vastly inferior to contemporary TEMs in terms of resolution. Later Albert V. Crewe improved the STEM with the invention of the cold field-emission gun [10, 11] and a better objective lens, enabling to discriminate between single heavy atoms in a molecule [12]. Modern TEMs can often be operated in both, TEM and STEM mode. The main difference between these modes is that the incident beam is static in the TEM mode, while it is scanned over the specimen in STEM mode using deflection scan coils.

The electron beam produced by the electron gun, can be shaped in two different ways by the electron lenses located before the specimen in beam direction: it can consist of essentially a single plane wave in beam direction and illuminate the sample homogeneously over a comparably large area,

which is also called *parallel illumination*, or it can be focused on a spot and form a so-called *convergent beam*. In the convergent case, the beam can be visualized as a cone and the angle describing the cone of possible incident wavevectors is known as the *convergence semi-angle* α ¹. Spatial resolution is fundamentally limited in the STEM by the *diffraction-limited* diameter of the convergent beam [13]

$$d = \frac{1.22 \lambda}{\sin(\alpha)}, \quad (1.2)$$

which shows that the resolution improves with a larger convergence semi-angle α and that parallel illumination produces no image contrast in the STEM. In the following, we will focus on the STEM as most modern EELS capabilities are used in this mode.

Once the initial beam has been shaped by the electron optics behind the electron gun, it interacts with the specimen in a multitude of ways, all of which are some form of scattering. We will come back to this point in the following paragraph and focus here on a brief description of the remaining components of the STEM. After the interaction with the specimen, further electron lenses guide the beam to the analysis stage marked as *Image recording system* in Fig. 1.1, which is comprised of one or more detectors in a modern STEM. Examples of such detectors are pixelated detectors such as a Charge-Coupled Device (CCD) camera or direct-electron detectors (we will return to this point below), and Annular Dark Field (ADF) and High Angle Annular Dark Field (HAADF) detectors, which cover a certain annular range of scattering angles. Furthermore the kinetic energy of electrons in the beam can be analysed with an Electron Energy Loss (EEL) spectrometer in many STEMs.

A pixelated detector can be used to capture diffraction patterns in TEM and STEM, and images in TEM mode. Atomically resolved STEM images are often formed using ADF or HAADF detectors, which allow for the simultaneous acquisition of on-axis EELS using the EEL spectrometer. Often the acceptance angle of imaging detectors and EEL spectrometers is described in terms of the so-called *collection semi-angle* β , the angle between the direct beam and the beams accepted by the analyzer.

In a so-called *on-axis* scattering geometry, all beams scattered under angles β' , which satisfy $0 \leq \beta' \leq \beta$ mrad, are collected.

In an *off-axis* geometry, one typically distinguishes two cases: ADF and HAADF detectors accept all beams scattered under angles β' , which satisfy $\beta_{\text{inner}} \leq \beta' \leq \beta_{\text{outer}}$, where β_{inner} is the inner detector angle and β_{outer} is the outer angle of the detector. Alternatively, one can also create an *off-axis* geometry with a detector, which is physically placed in the same spot as an

¹The convergence angle is usually measured in milli-radian (mrad) and we have $\alpha \approx 0$ mrad for parallel illumination and $\alpha > 0$ mrad for a convergent beam.

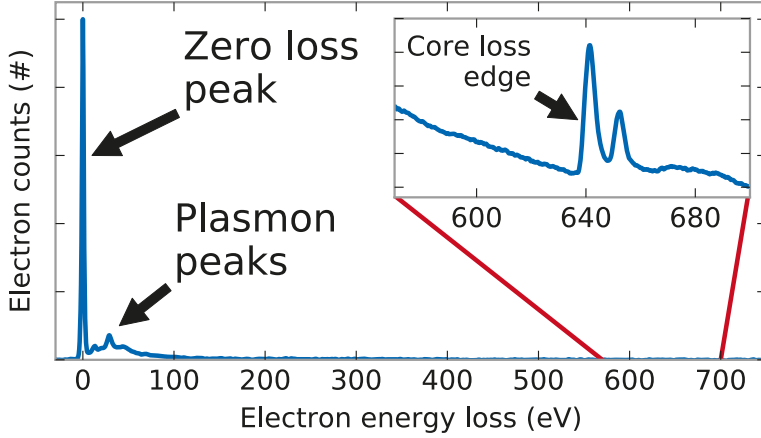


Figure 1.2. Schematic of a full EEL spectrum with the major energy loss regimes indicated. The zero-loss peak constitutes elastic scattering, whereas plasmon scattering originates from collective excitations of the electron gas. Core-loss peaks are due to beam electrons losing energy to electrons in the sample, which are promoted to higher energy levels from electronic states closely bound to the nucleus. Not indicated is the recently opened up phonon loss region on the flank of the zero-loss peak (see section 1.2 for further information). Figure reprinted from Ref. [14].

on-axis detector by deflecting the diffraction pattern by an angle β_0 with respect to the detector. Under such conditions only those beams, which were scattered under angles β' , which satisfy $|\beta_0 - \beta'| < \beta$ are collected².

We distinguish the interaction between beam and specimen as *elastic* and *inelastic* scattering. In elastic scattering the energy of the beam electrons is unchanged, while the beam electrons loose energy in inelastic scattering processes. We display a typical EEL spectrum in Fig. 1.2, where the primary feature of the spectrum, the so-called Zero-loss Peak (ZLP) has historically been regarded as elastically scattered electrons. The predominant source of elastic scattering in the STEM is *Rutherford scattering* off of the (screened) atomic nuclei of the specimen. The energy transfer is thereby near zero, due to the large difference in mass between both objects, while considerable momentum transfer can occur. Elastic scattering gives thus information about the atomic structure of matter and is primarily used for high resolution imaging and diffraction.

The primary origin of inelastic scattering on the other hand are interactions between the beam electron and the electronic structure of the specimen, which give rise to the plasmon peaks and core-loss edges in Fig. 1.2. Historically inelastic scattering has therefore enabled to study the elec-

²Note here the use of vector notation $\beta_0 = (\beta_{0x}, \beta_{0y})$ and $\beta' = (\beta'_x, \beta'_y)$.

tronic structure of matter and provides, among others, elemental identification, information about atomic bonding and also more recently magnetic information [15].

Figure 1.2 shows that the elastic interaction of electrons with matter is very strong, much stronger, than the inelastic interactions and it is this circumstance, which complicates the theoretical treatment of inelastic scattering in the STEM considerably. Furthermore we will see in section 1.2, that the tails of the zero-loss peak also contain information about inelastic scattering processes. It is this regime, that we will be mainly concerned with in this thesis.

1.2 Instrumental Advances

Since the times of Ernst Ruska, the quest for better spatial resolution has been one of the main drivers in the design of new microscopes. Richard Feynman famously challenged the microscopy community more than 60 years ago to make the electron microscope 100 times better and STEMs have since come very close to completing the challenge [16, 17].

According to eq. (1.2), the fundamental diffraction-limit to spatial resolution can be improved in one of two ways in the STEM: by reducing the wavelength λ or by increasing the convergence semi-angle α . The former is tantamount to an increase of the momentum and thus the kinetic energy of the electrons according to equation (1.1) and can be achieved by increasing the accelerating voltage of the microscope. However, with increasing acceleration voltage, the issue of beam damage becomes aggravated and the size of the microscope increases, too, which both limit the practice. Increasing the convergence angle is limited by the strong aberrations of electron lenses and spatial resolution had to be eventually improved by decreasing the lens aberrations.

Around the turn of the last millenium, aberration correctors were developed for both the TEM and the STEM [18, 19]. These allow for routine atomic resolution imaging in STEMs and today's records in spatial resolution are at the sub-Å scale in both the TEM and STEM [17, 20–23]. A great review on the topic is Ref. [24].

Aberration correction fundamentally enabled also the design of a new electron beam monochromator [25], which essentially consists of two EEL spectrometers run back-to-back. The first spectrometer disperses the beam using electron optical elements and creates an intermediate EELS, which is projected onto a slit. In this way the slit lets only electrons pass, whose kinetic energies is within a certain range given by the width of the slit. The second spectrometer undisperses the beam such that a monochromated, convergent beam interacts with the sample. This monochromator has very recently enabled to resolve peaks in EELS corresponding to excitations of

few tens of meV [25]. Routinely an energy resolution of 10-20 meV is achieved while the record stands at about 4.2 meV at 30 keV beam energy and 2.9 meV at 20 keV [26, 27]. These new capabilities allow spectroscopy of vibrational excitations, known as phonons in crystals, and perhaps soon also magnons [28–31], the quasi-particles associated with collective excitations of magnetic structures.

We use in this thesis the term High Energy Resolution Electron Energy Loss Spectroscopy (HERE) to refer to EELS performed with high energy resolution for the study of low energy excitations. It should be noted, that the energy resolution alone is not unprecedented in EELS, but has already been achieved in the 1960s and 1970s for high-energy electrons [32–36]. However, the setup used in these experiments had no spatial resolution and it is the *combination* of high spatial resolution with high energy resolution, which enables today’s amazing possibilities in the STEM and promise a bright future for localized vibrational spectroscopy [37].

Aberration correction and better monochromators are not the only tools the most technologically advanced STEMs for EELS sport today. Recently a direct electron detector was introduced, which has much improved noise levels, is resistant to beam damage, and has a wide dynamic range [38]. This detector simplifies and enables new experimental designs, since it allows to capture weak signals with a sufficient Signal-to-Noise Ratio (SNR) in the presence of strong signals at different energies.

We have set in this section the stage for experiments in the fields of vibrational spectroscopy in the STEM. We will review key results of these experiments in the following section.

1.3 Key Experiments in Vibrational EELS

Most vibrational EELS experiments have been performed on organic compounds and single layer as well as multi-layer van der Waals materials owing to their relatively large vibrational frequencies, which enhances SNR in HERE and facilitates experiments. Of such materials hexagonal Boron Nitride (hBN) is the most popular, likely because it exhibits strong anisotropy between out-of-plane and in-plane components of many properties, which is of interest for functional applications. The bonds making up hBN are furthermore highly polar and the material features therefore significant charge transfer between B and N atoms.

Recent work has paid close attention to the spatial resolution of vibrational STEM-EELS and it was shown, that the beam electrons interact via two scattering mechanisms with the specimen, whose signals have very different characteristics [39]: The electron can excite vibrational modes in materials containing polarizable bonds via a long-range Coulomb interaction or through a large momentum transfer, small impact parameter in-

teraction near the atom's nucleus. The first mode of scattering is called *dipole scattering* or *dipolar scattering* and is largely delocalized, since very little momentum is transferred in the process, but its contribution to vibrational EELS is significant in the forward direction. It requires vibrations involving bond polarization such that a macroscopic polarization can arise, which limits dipolar scattering to long wavelength (short momentum $q \rightarrow 0$) optical phonons in crystals [40]. The second scattering mechanism, called *impact scattering*, is associated with highly localized large angle scattering, due to the large momentum transferred. Impact scattering is also the mechanism behind atomic-resolution HAADF-STEM images [41, 42]. These two scattering mechanisms are exploited in vibrational EELS in different ways and have enabled a multitude of exciting measurement techniques, which can be broadly categorized by the scattering geometry in the following way: damage-free aloof vibrational EELS of beam-sensitive materials, vibrational EELS at high spatial resolution and vibrational EELS with high momentum resolution.

In aloof vibrational EELS experiments the delocalized, long-range dipolar interaction is exploited, which allows the electron beam to pass through vacuum tens of nanometers outside of the specimen in an effort to avoid beam damage [43]. Biological molecules and crystals are the prime candidates for such experiments and it is thus no surprise, that the technique was demonstrated by measuring the vibrational EELS of guanine crystals [44], but it was also proposed as an ideal tool for characterization of nanoparticle surfaces [45]. Other applications include the detection of water and oxygen-hydrogen bonds [46], nano-scale temperature measurement based on the principle of detailed balance [47, 48], determining the presence of water at the nanometer-scale and its isotopic composition [49], as well as the identification of isotopic composition of molecules [50].

In crystals and in the context of vibrational EELS, dipolar scattering is often cast in the language of Phonon Polaritons (PhPs), which are quasiparticles due to the hybridization between an optical phonon and a photon. Fundamentally a small wavevector (long wavelength) optical phonon produces an electric field in a polar material, giving rise to the hybridization with photons forming the PhPs. In materials with an isotropic dielectric function $\epsilon(\omega)$, such as cubic materials, the PhPs are purely transverse excitations, so only coupling between Transverse Optical (TO)-phonons and photons is possible [51]. In bulk crystals of such materials lower and upper PhP branches are observed below and above the so-called *Reststrahlen band*, which is the region forbidden for light propagation between the frequency ω_{TO} of the TO phonon and the frequency ω_{LO} of the Longitudinal Optical (LO) phonon [52, 53]. In layered van der Waals (vdW) materials, such as hBN, the strong anisotropy of the dielectric permittivity leads to the appearance of so-called Hyperbolic Phonon Polaritons (HPhPs), which exhibit a hyperbolic dispersion [53]. Furthermore, polaritonic modes are

sensitive to shape and size effects [54] and in materials of finite thickness, guided and surface PhP modes are observed in addition to bulk modes. HERE has developed into an extremely useful tool to study these polari-tonic excitations at the nano-scale [55–58]. We will not go into further de-tail here, since we will focus on larger momentum transfers and impact scattering for most parts of this thesis. The main fact to keep in mind for our purposes is, that EELS is dominated by the excitation of PhPs or HPhPs at small momentum transfers in polar materials rather than by bulk pho-nons [55].

Vibrational EELS at high spatial resolution requires a highly focused electron beam, i.e., a large convergence angle α , similar to conventional HAADF-STEM imaging. In this mode, the trademark feature of the STEM, high spatial resolution, is really combined with the new capability of high energy resolution. Under these conditions, but without the newest mono-chromators, it was shown, that localized atomic-scale spectroscopic infor-mation could be extracted by careful analysis of the flanks of the zero-loss peak (ZLP), which was attributed to phonon scattering, at an energy res-olution of only around 100 meV [59]. Using the new monochromators, impact scattering vibrational EELS exhibits atomic resolution in on- and off-axis geometries for large collection angle β [60, 61].

In polar materials one needs to overcome the aforementioned delocal-ized dipolar scattering when pushing for spatial resolution. Since dipolar scattering involves small scattering angles, elastic scattering will distribute the dipolar signal to all angles, permitted by elastic scattering, i.e., the posi-tions of Bragg spots in the diffraction plane for a sufficiently small conver-gence angle. Under these conditions it was demonstrated that the impact signal, located in between Bragg spots and collected in such a way as to avoid the Bragg spots entirely, permits for nanometer resolution in vibra-tional EELS [62]. For a large convergence angle, Bragg spots overlap in the diffraction plane and the dipolar signal is distributed throughout the diffraction plane. Under these conditions it was shown that on-axis vibra-tional EELS contains no atomic-scale contrast [63]. However, shifting the EEL spectrometer entrance aperture to a large-angle off-axis position al-lows for an atomic-scale contrast in phonon spectrum images [60]. This demonstrates that dipolar scattering is strongly reduced in the high-angle off-axis spectra in comparison with impact scattering. It is furthermore possible to spectroscopically separate impact and dipolar scattering under certain conditions due to the selection rules of dipolar scattering [40, 61].

Furthermore both optical and acoustical modes contribute to high-angle off-axis vibrational EELS and spectrum images formed by either of these modes show essentially identical contrast [60]. Additionally, in the on-axis geometry, significant spectral changes were observed as the beam is scanned across neighboring atomic columns for $\beta < \alpha$ [61]. On-axis im-pact scattering is prone to contrast reversal, which can be explained by elec-

tron channeling effects and can be mitigated by an appropriate underfocus of the probe or avoided entirely by using high-angle detectors [63]. Spatial resolution was pushed to the limit by demonstrating, that it is possible to distinguish a single Silicon impurity in a graphene sheet by its localized vibrational signature [64]. More recently also chemical-bonding sensitivity has been demonstrated on the same system [65]. Defect systems are of large interest for technological applications, since these control many important thermal properties at the nanoscale. Vibrational EELS at high spatial resolution is a powerful technique for this purpose due to the unique combination of high spatial resolution and sufficient energy resolution. It has been shown to allow spatial mapping of the modifications of phonons induced by a planar defect, interfaces, superlattices, and grain boundaries [66–70], thus enabling engineering of heat management at the nanoscale. Another interesting application of vibrational EELS at high spatial resolution is the imaging of isotope diffusion during annealing in a monolayer of graphene [71].

However, the large convergence angle used for high spatial resolution experiments prohibits the extraction of momentum information, since individual Bragg disks due to elastic scattering overlap in the diffraction pattern and prevent therefore an unambiguous mapping of certain scattering angles to a certain momentum transfer. Instead, the large convergence angle should effectively integrate the vibrational EELS signal over reciprocal space at individual points in the diffraction plane in a single inelastic scattering picture. The collection angle has a similar effect, yet the relative excitation of different modes depends strongly on the choice of convergence and collection angles in on-axis vibrational EELS [40], which suggests, that the on-axis spectrum is not a simple function of the total range of contributing momentum transfers.

Therefore experiments requiring momentum resolution in the diffraction plane necessarily need to reduce the convergence angle α as well as the collection angle β . Initial high momentum resolution experiments adopted a strategy to form the diffraction pattern in such a way, that only a small range of momentum transfers (scattering angles) is accepted by the EEL spectrometer. By shifting the diffraction pattern relative to the EELS aperture, one can select the momentum transfer, at which the HERE should be obtained. Then, the vibrational EELS recorded at different momentum transfers reveals the phonon dispersion, when individual measurements are stitched together in a so-called (q, E) map [72–74]. Using newly developed hybrid-pixel detectors and a slit aperture, however, it is now also possible to record the phonon dispersion along a certain direction in the diffraction plane in a single measurement instead of a series of measurements at different momentum transfers [38]. These capabilities have already been used to measure the phonon dispersion in Boron Nitride (BN) nanotubes [75] and at interfaces [76]. It is also possible to obtain a spatially

localized signal of defects in momentum-resolved measurements by allowing only momentum transfers to contribute to the spectra, for which strong spectral modifications are observed as a function of beam position [66]. Furthermore imaging of phonon dynamics using momentum-resolved vibrational EELS near a quantum dot was reported [77].

Exciting experiments combining several of these techniques have also been reported. For example, vibrational surface states were mapped using both dipolar scattering as well as high resolution off-axis vibrational EELS [78]. Large, temperature-dependent energy shifts in phonon modes were observed in on-axis EELS as well as dipolar scattering, which allows for temperature measurement and in the case of high spatial resolution on-axis vibrational EELS also mapping of temperature in a nanoparticle [79]. Furthermore it was reported, that on-axis vibrational EELS allows to extract nanometer-scale vibrational information from interfaces, even if dipolar scattering dominates [80]. In a similar geometry, but using a larger collection angle, mapping of functional groups of molecules was demonstrated with a spatial resolution of better than 15 nm [81]. The origin of the spatial resolution in these results is still not entirely understood due to a lack of theories treating dipolar and impact scattering on an equal footing for a penetrating beam geometry [81].

After reviewing current experimental techniques and results in vibrational EELS, we proceed in the following chapter with an overview of vibrational EELS theories and make the case why there is a space for another model.

2. Theories of Phonon scattering for High-Energy Electrons

In this chapter we describe the theoretical underpinnings of the theory of high-energy electron scattering by vibrational excitations. Historically, research has mostly focused on the effect of so-called *Thermal Diffuse Scattering* (TDS) on images and diffraction patterns, since vibrational losses were not accessible to EELS [82–84]. TDS is the total inelastic scattering associated with all possible vibrational losses throughout the diffraction plane. This has changed with the advent of monochromators capable of reducing the width of the zero-loss peak to around or below 10 meV (c.f. section 1.2). Today vibrational EELS experiments are interpreted using a variety of approaches, which we will briefly review here. We will see that all of these approaches are partial solutions to the general problem of describing vibrational EELS and there is to this date no tractable simulation method, which can fully describe all regimes and experiments, for the challenges are immense: vibrational EELS experiments are sensitive to properties over a large range of length scales, from dipole scattering on macroscopic fields to impact scattering at the atomic scale. Therefore multi-scale modelling approaches are likely required to treat both modes of scattering on a more equal footing. Furthermore we will see that the large number of possible initial and final states, the requirement of thermally averaging over initial states, and the possibility of the electron undergoing multiple elastic and inelastic events complicate the modelling of vibrational EELS in the impact scattering regime.

2.1 Dielectric formalism

Vibrational EELS can be modeled using a semi-classical electrodynamics based description, in which the EEL probability $\Gamma_{\text{EELS}}(\omega)$ is related to the work performed by the electron against the induced electrical field along a straight trajectory [85, 86], i.e., the total energy loss is written as

$$\begin{aligned}\Delta E &= e \int_{-\infty}^{\infty} dt \mathbf{v} \cdot \mathbf{E}_{\text{ind}}(\mathbf{r}(t), t) \\ &= \int_0^{\infty} d\omega \hbar\omega \Gamma_{\text{EELS}}(\omega)\end{aligned}$$

where \mathbf{E}_{ind} is the field induced by the electron moving along a straight trajectory $\mathbf{r}(t)$ with velocity \mathbf{v} , which is usually obtained from a solution of Maxwell's equations with a spatially local dielectric function $\varepsilon(\omega) := \varepsilon(\mathbf{q} = 0, \omega)$ in the long wave length limit and appropriate boundary conditions. This approach works well for small angle dipolar scattering processes, especially in aloof geometries, and allows to interpret dipolar scattering experiments with great success [55, 57, 87–90]. However when the beam gets close to atomic columns in intersecting geometries and electrons are scattered towards large angles, i.e., in the impact scattering regime, the description of the sample in terms of the local dielectric function in the long wavelength limit is not satisfactory [91]. Therefore we need to employ other theories for transmission geometries and impact scattering. In Refs. [78, 91] a step towards this goal is achieved within the semi-classical picture conveyed by eq. (2.1) by essentially improving the description of the induced fields to include short wavelength modes by means of lattice dynamics and molecular dynamics calculations. The resulting spectra include then losses to phonon modes, which are absent if one considers only the local dielectric function $\varepsilon(\omega)$ in the long wave length limit [91].

2.2 The first-order Born approximation

In order to describe impact scattering, we need to consider atomic-level details of the variation of the beam-sample interaction and we enter thus the domain of quantum mechanics. We consider some central results of time-independent scattering theory in appendix A. The main result is that the Double Differential Scattering Cross Section (DDSCS) for the transition $|i\rangle \rightarrow |f\rangle$ is written as (c.f. eqs. (A.5)) and C.2

$$\frac{d^2\sigma_{i \rightarrow f}}{d\Omega_{\mathbf{k}'} d\Delta E} = \frac{(2\pi)^4 m_e^2}{\hbar^4} \frac{k'}{k} |\langle \mathbf{k}', \Phi_f | \hat{T} | \mathbf{k}, \Phi_i \rangle|^2 \delta(E_{\Phi_f} - E_{\Phi_i} - \Delta E), \quad (2.1)$$

where \mathbf{k} and \mathbf{k}' are the initial and final wave vector of the scattering particle, $|\Phi_i\rangle$ and $|\Phi_f\rangle$ are the initial and final states of the sample, and the Dirac- δ signifies overall energy conservation between beam and sample. In the first-order Born approximation, we replace the operator transition operator \hat{T} by the interaction operator \hat{H}_{inter} , i.e., we consider that electrons are scattered only once by the potential. The derivation of the first-order Born approximation for phonon scattering of electrons [92] is very analogous to the derivation for the scattering of neutrons and X-rays on phonons [93–98]. We present in this thesis a lengthy, yet mostly complete, derivation of the DDSCS for electrons.

We start with the interaction of an electron with the full many-body system of the sample and split the sample in an electronic and a nuclear

subsystem by virtue of the Born-Oppenheimer (BO) approximation in appendix B. In this appendix, we limit ourselves to the first-order Born approximation, i.e., we replace \hat{T} by \hat{H}_{inter} , and arrive at an expression for the DDSCS associated with the transition $|i\rangle \rightarrow |f\rangle$, which depends on the Fourier transform of the electronic and nuclear charge densities. We then average the DDSCS in eq. (2.1) over initial states and sum over final states in appendix D, since the sample will generally be in thermal equilibrium and we have no control over the final state of the sample. Following van Hove [99], these considerations lead to the definition of the Dynamic Form Factor (DFF)

$$S(\mathbf{q}, \Delta E) := \int_{-\infty}^{\infty} \frac{dt}{2\pi\hbar} e^{-i\Delta E t/\hbar} \langle \rho_{\text{tot}}^{\dagger}(\mathbf{q}, \{\hat{\mathbf{R}}_{\kappa}\}) \rho_{\text{tot}}(\mathbf{q}, \{\hat{\mathbf{R}}_{\kappa}(t)\}) \rangle_T, \quad (2.2)$$

where $\langle \rho_{\text{tot}}(\mathbf{q}, \{\hat{\mathbf{R}}_{\kappa}\}) \rho_{\text{tot}}(\mathbf{q}, \{\hat{\mathbf{R}}_{\kappa}(t)\}) \rangle_T$ is the density-density correlation function. Using eq. (2.2) the DDSCS can be written as [92, 99]

$$\frac{d^2\sigma}{d\Omega_{\mathbf{k}'} d\Delta E} = \frac{m_e^2 e^4}{(2\pi)^2 \hbar^4 \epsilon_0^2} \frac{k'}{k} \frac{1}{q^4} S(\mathbf{q}, \Delta E). \quad (2.3)$$

We consider then a crystal in the *harmonic approximation*¹ as the target in appendix E and proceed further by describing the total charge density within the Independent Atom Model (IAM) in appendix F. The correlation function of the charge density appearing in eq.(2.2) reduces to thermal averages of exponentials of displacement operators in the IAM and we show in appendix G how these averages are computed.

We find that the DDSCS in first-order Born approximation and using the IAM can be written as a series

$$\frac{d^2\sigma}{d\Omega_{\mathbf{q}} d\Delta E} = \sum_{\eta=0}^{\infty} \frac{d^2\sigma^{(\eta)}}{d\Omega_{\mathbf{q}} d\Delta E}, \quad (2.4)$$

where the leading two terms $\eta = 0$,

$$\frac{d^2\sigma^{(0)}}{d\Omega_{\mathbf{q}} d\Delta E} = N_{\text{uc}}^2 \sum_{\mathbf{G}} \delta_{\mathbf{q},\mathbf{G}} \left| \sum_{j=1}^{N_{\text{ba}}} e^{-i\mathbf{G}\cdot\mathbf{R}_j^0} f_{ej}(G) e^{-W_j(\mathbf{G},T)} \right|^2 \delta(\Delta E), \quad (2.5)$$

and $\eta = 1$,

$$\begin{aligned} \frac{d^2\sigma^{(1)}}{d\Omega_{\mathbf{q}} d\Delta E} &= \frac{\hbar N_{\text{uc}}}{2} \frac{k'}{k} \sum_{\mathbf{G},\nu} \delta_{\mathbf{q}-\mathbf{q}_0,\mathbf{G}} \left| \sum_{j=1}^{N_{\text{ba}}} e^{-i\mathbf{G}\cdot\mathbf{R}_j^0} f_{ej}(q) e^{-W_j(\mathbf{q},T)} \frac{(\mathbf{q}\cdot\boldsymbol{\epsilon}_{j\mathbf{q}_0\nu})}{\sqrt{m_j}} \right|^2 \times \\ &\times \left[\frac{\langle n_{\mathbf{q}_0\nu} \rangle_T + 1}{\omega_{\mathbf{q}_0\nu}} \delta(\hbar\omega_{\mathbf{q}_0\nu} - \Delta E) + \frac{\langle n_{\mathbf{q}_0\nu} \rangle_T}{\omega_{\mathbf{q}_0\nu}} \delta(\hbar\omega_{\mathbf{q}_0\nu} + \Delta E) \right]. \end{aligned} \quad (2.6)$$

¹The harmonic approximation and phonon calculations are also the topic of sec. 3.3.

correspond to the DDSCS associated with elastic (0-phonon) and single inelastic (1-phonon) scattering, respectively. The energy-gain term is proportional to $\delta(\hbar\omega_{\mathbf{q}_0\nu} + \Delta E)$, while $\delta(\hbar\omega_{\mathbf{q}_0\nu} - \Delta E)$ corresponds to the energy-loss part of the DDSCS. We refer the interested reader to the derivations in the relevant appendices for a definition of all quantities in these expressions and also to sec. 3.3 for more details on phonon properties and calculations.

Equations (2.5) and (2.6) present a more suitable approach for intersecting beam geometries as they explicitly include interactions with all phonon modes up to large momentum transfers \mathbf{q} . We can understand a few important properties from these expressions. For example the dot product $\mathbf{q} \cdot \boldsymbol{\epsilon}_{j\mathbf{q}_0\nu}$ leads to a selective enhancement of modes, whose phonon polarization has a component along \mathbf{q} . It is therefore argued in the supplementary material of Ref. [64] that the main features of impact scattering vibrational EELS measured with a large off-axis detector can be understood in terms of the Phonon Density of States (PDOS) projected along the direction of the considered momentum-transfer \mathbf{q} (c.f. sec. 3.3). We will return to this point in the discussion of paper II and continue here by briefly considering the geometry of the momentum transfer at different scattering angles θ and energy losses ΔE .

We show in Fig. 2.1 how the ratio of the absolute value of the components of momentum transfer $\mathbf{q} = (\mathbf{q}_\perp, q_z)$ perpendicular and parallel to the initial wave vector \mathbf{k} varies over a wide range of the scattering angles and energy losses (c.f. appendix H, especially eq. (H.6)). The inset depicts the range of these quantities, which are commonly studied in vibrational EELS. We note that in this range, $|\mathbf{q}_\perp| > q_z$ and, together with the momentum transfer selectivity described above, the vibrational EELS is therefore mainly sensitive to modes, whose polarization has components perpendicular to the incident wave vector and parallel to the momentum transfer \mathbf{q} .

The first-order Born approximation has seen wide adoption in calculations of momentum-resolved scattering cross sections of thin materials consisting of light atom species [73, 74, 92] and it has been used as a theoretical tool to understand some properties of the inelastic impact scattering cross section [64, 77, 100]. It should also be noted that the first-order Born approximation includes in principle dipolar scattering on optical phonons at small \mathbf{q} as long as the charge transfer in polar materials is included in the modeled charge density. This can be achieved by considering perturbations to the electron density due to atomic displacements within Density Functional Perturbation Theory (DFPT) [74] or appropriately scaled (ionic) scattering factors [63, 92].

We note that the first-order Born approximation as we have laid it out here considers only a single plane wave component $|\mathbf{k}\rangle$ of the incident beam. For a convergent beam in e.g. STEM, we would need to take the initial state to be a sum over the incident momentum transfers compatible

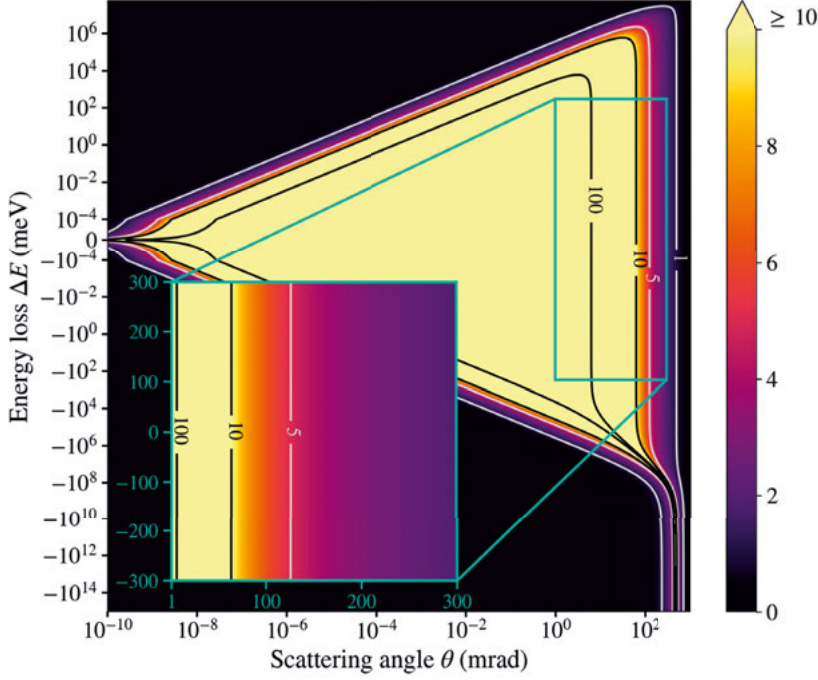


Figure 2.1. Color map plot of the ratio of $|\mathbf{q}_\perp|/|q_z|$ computed using eq. (H.6) as a function of scattering angle θ and energy loss ΔE . We consider thereby an initial kinetic energy $E_k = 60$ keV. Note the logarithmic axes in the main plot and the linear axes scale in the inset, which shows the typical regime of vibrational EELS.

with the probe-forming aperture $A(\alpha)$, i.e.,

$$|i\rangle \propto \sum_{\mathbf{k}_\perp \in A(\alpha)} |\mathbf{k}, \Phi_i\rangle \quad (2.7)$$

in eq. (A.3a). This leads effectively to an integration of the scattering amplitude $f_{i \rightarrow f}(\mathbf{k}, \mathbf{k}')$ over a range of values of \mathbf{k} . For a large enough convergence angle α , it would give rise to the appearance of the Mixed Dynamic Formfactor (MDFF) $S(\mathbf{q}, \mathbf{q}', \omega)$ instead of the DFF in the expression of the DDSCS [101]. A similar effect would be observed for the case of a finite detector entrance aperture, which would require to sum over the accepted range of final momenta \mathbf{k}' . No systematic studies on the impact of the convergence and collection semi-angles on calculated vibrational EELS have been reported yet to the best of our knowledge, but it is a commonly accepted view in the literature, that for large enough convergence and/or collection angles, the EELS is comparable with the projected PDOS along \mathbf{q}_\perp as we have described above. It should be mentioned here that Konečná *et al.* have developed a single inelastic scattering theory for atomic-scale

mapping, which takes the incident beam shape explicitly into account and which was applied to isotope mapping in a h-BN type molecule [102].

Opening the convergence angle has another implication in the treatment of scattering theory as we have laid it out here, which is worth mentioning: we note in appendix A that the conventional definition of the DDSCS according to eq. (2.1) does not predict the correct number of counts in the forward direction at zero energy loss. In the Bright Field (BF) in STEM, this issue gets aggravated, since Bragg spots broaden into Bragg disks for finite convergence angles. Consequently the observed intensities on the detector deviate for larger convergence angle over a larger range of momentum transfers from the DDSCS of eq. (2.1). Thus for the correct description of the elastic cross section, we cannot apply the DDSCS as derived here alone, but we need to consider also the initial wave. We will see below that for this reason, we work usually with scattered wave function for the purpose of TEM and STEM.

Despite all these successes in describing momentum resolved experiments and in allowing to understand some of the functional dependencies of vibrational EELS, the first-order Born approximation has some major shortcomings [103]. First of all the criterion for its range of validity is commonly stated as [104, 105]

$$\frac{\Delta z H_{\text{inter}}}{h\nu} \ll 1, \quad (2.8)$$

where Δz is a characteristic *range* of the potential. Even for high-energy electrons this criterion can not be fulfilled for thick specimen, especially not for infinite crystals as in our derivation. The reason for this is, that for thick specimen $\Delta z \gg 0$, a “characteristic” value of the interaction potential H_{inter} can approach very large values for the Coulomb potential near the nucleus. Furthermore the electron speed v is limited by the speed of light c , so even electrons with very high energy will not be able to satisfy equation (2.8) [104–106]. Furthermore, for scattering on a single atom, the first-order Born approximation leads to a purely real scattering amplitude for elastic scattering, which is incompatible with the conservation of probability [106, 107], an issue, which adds to the forward scattering issue of the elastic cross section discussed above. In order to obtain more physical scattering amplitudes for electrons, higher-order terms need to be taken into account in the Born series [104, 106, 108], i.e., multiple elastic scattering needs to be included even for scattering on single atoms.

2.3 Elastic scattering of high-energy electrons

We have argued in the previous section, that the Born approximation is not sufficient for treating elastic scattering in the context of TEM and STEM.

If we return then to appendix A and limit ourselves to elastic interactions with a potential

$$\hat{H}_{\text{inter}} = \frac{2\pi\hbar^2}{m_e} \int_{-\infty}^{\infty} \frac{d\mathbf{q}}{(2\pi)^3} e^{i\mathbf{q}\cdot\hat{\mathbf{r}}} \sum_{\kappa} e^{-i\mathbf{q}\cdot\mathbf{R}_{\kappa}^{(0)}} f_{e,\kappa}(q), \quad (2.9)$$

where $\mathbf{R}_{\kappa}^{(0)}$ are the equilibrium positions of nuclei and we have assumed the IAM of appendix F. We take the initial and final states to be just plane wave states, i.e.,

$$|i\rangle = |\mathbf{k}\rangle, \quad \langle f| = \langle \mathbf{k}'|. \quad (2.10)$$

Time-independent scattering theory allows then only elastic scattering for this problem, since the DDSCS reduces to

$$\frac{d^2\sigma_{i\rightarrow f}}{d\Omega_{\mathbf{q}} d\Delta E} = \frac{(2\pi)^4 m_e^2}{\hbar^4} |\langle \mathbf{k}' | \hat{T} | \mathbf{k} \rangle|^2 \delta(\Delta E) = |f(\mathbf{k}, \mathbf{k}')|^2 \delta(\Delta E), \quad (2.11)$$

where $k = k'$ and $\mathbf{k} \perp \hat{\mathbf{z}}$. For high-energy electrons and small angle scattering, the scattering amplitude $f(\mathbf{k}, \mathbf{k}') = \langle \mathbf{k}' | \hat{T} | \mathbf{k} \rangle$ can be approximated as [104]

$$f(\mathbf{k}, \mathbf{k}') = -\frac{ik}{2\pi} \int_{-\infty}^{\infty} d\mathbf{r}_{\perp} e^{i\mathbf{q}_{\perp}\cdot\mathbf{r}_{\perp}} [1 - \phi(\mathbf{r}_{\perp})], \quad (2.12)$$

where $\mathbf{r} = (\mathbf{r}_{\perp}, z)$ and $\mathbf{q} = \mathbf{k}' - \mathbf{k} = (\mathbf{q}_{\perp}, q_z)$ and we have introduced the Phase Object Approximation (POA) wave $\phi(\mathbf{r}_{\perp})$, an interaction parameter σ and the projected potential $V_{\text{proj}}(\mathbf{r}_{\perp})$

$$\phi(\mathbf{r}_{\perp}) = e^{i\sigma V_{\text{proj}}(\mathbf{r}_{\perp})} \quad (2.13a)$$

$$\sigma = \frac{m_e}{\hbar^2 k} \quad (2.13b)$$

$$V_{\text{proj}}(\mathbf{r}_{\perp}) = - \int_{-\infty}^{\infty} dz H_{\text{inter}}(\mathbf{r}). \quad (2.13c)$$

The projected potential reads

$$V_{\text{proj}}(\mathbf{r}_{\perp}) = -\frac{(2\pi)\hbar^2}{m_e} \int_{-\infty}^{\infty} \frac{d\mathbf{q}_{\perp}}{(2\pi)^2} e^{i\mathbf{q}_{\perp}\cdot\mathbf{r}_{\perp}} \sum_{\kappa} e^{-i\mathbf{q}_{\perp}\cdot\mathbf{R}_{\perp\kappa}^{(0)}} f_{e,\kappa}(q_{\perp}), \quad (2.14)$$

where we have carried out the integration over z , which yields $2\pi\delta(q_z)$.

Eq. 2.12 is a more appropriate approximation to the scattering amplitude of a thin sample than the first-order Born approximation for electrons. However, this scattering amplitude still suffers from the neglect of the contributions of the *unscattered* wave, while the POA wave function $\phi(\mathbf{r})$ and its intensity explicitly include the unscattered wave as it can be seen from

eq. (2.12): the difference between one and the POA wave effectively removes the initial plane wave

$$\phi_0(\mathbf{r}_\perp) = 1 \quad (2.15)$$

from the equation for the scattering amplitude. Thus, if we carry out the spatial Fourier Transform (FT) in eq. (2.12), we see that the DDSCS becomes

$$\frac{d^2\sigma_{i \rightarrow f}}{d\Omega_{\mathbf{q}_\perp} d\Delta E} = \frac{k^2}{(2\pi)^2} |\delta(\mathbf{q}_\perp) - \phi(\mathbf{q}_\perp)|^2, \quad (2.16)$$

so we can define a quantity

$$\frac{d^2\tilde{\sigma}_{i \rightarrow f}}{d\Omega_{\mathbf{q}_\perp} d\Delta E} = \frac{k^2}{(2\pi)^2} |\phi(\mathbf{q}_\perp)|^2, \quad (2.17)$$

which is proportional to the measured counts also for $\mathbf{q}_\perp = 0$, contrary to the DDSCS. Since k is just a scaling constant in elastic scattering under small angles, independent of \mathbf{q}_\perp , we can use the intensity $|\phi(\mathbf{q}_\perp)|^2$ of the POA for most purposes, such as estimates of the relative scattering probability. The POA wave is often used in the context of TEM and STEM if a simple model of elastic scattering is required for thin enough specimen.

If the initial wave function $\phi_0(\mathbf{r}_\perp)$ is different from a plane wave, the POA becomes simply

$$\phi(\mathbf{r}_\perp) = e^{i\sigma V_{\text{proj}}(\mathbf{r}_\perp)} \phi_0(\mathbf{r}_\perp) \quad (2.18)$$

and $|\phi(\mathbf{q}_\perp)|^2$ can still be used to quantify the scattering probability at momentum transfer \mathbf{q}_\perp . Furthermore the Weak Phase Object Approximation (WPOA)

$$\phi(\mathbf{r}_\perp) \approx [1 + i\sigma V_{\text{proj}}(\mathbf{r}_\perp)] \phi_0(\mathbf{r}_\perp) \quad (2.19)$$

is also a widely used further approximation for weak projected potentials. The DDSCS becomes for a plane initial wave in WPOA

$$\begin{aligned} \frac{d^2\sigma_{i \rightarrow f}}{d\Omega_{\mathbf{q}_\perp} d\Delta E} &= \frac{k^2}{(2\pi)^2} |\sigma^2 V_{\text{proj}}^2(\mathbf{q}_\perp)|^2 \\ &= \left| \sum_{\kappa} e^{-i\mathbf{q}_\perp \cdot \mathbf{R}_{\perp\kappa}^{(0)}} f_{e,\kappa}(q_\perp) \right|^2, \end{aligned} \quad (2.20)$$

which has the same functional dependence as eq. (2.5), except that we have not assumed a periodic arrangement of atoms here and the Debye Waller Factor (DWF) is missing due to neglecting thermal vibrations here.

The POA as we have developed it here is a better approximation for scattering on not too thick samples and motivates why we are usually concerned with the scattered waves rather than the DDSCS in the context of

TEM and STEM. However, the POA is still incapable of describing multiple elastic interactions at different thicknesses in the sample. In the usual language of electron microscopy, this multiple elastic scattering leads to so-called *dynamical diffraction* and *channeling*. The former is the dynamic, thickness-dependent reshuffling of elastic intensity between waves of different final wave vector \mathbf{k}' . Channeling on the other hand describes the tendency of electrons to stay close to an atomic column in STEM.

These effects are usually accounted for in quantitative simulations by the so-called *Bloch wave* method or the *multislice* method. Both approaches allow to calculate the scattered wave $\phi(\mathbf{q}_\perp, z)$ at some thickness z in the sample. In the former approach, the wave function of the beam electrons is expanded in terms of Bloch waves and the thickness-dependent interference of these Bloch waves shifts intensity back and forth between different plane wave states, which manifests itself as dynamical diffraction as the electron beam passes the specimen [109]. For perfect crystals, a small number of Bloch waves is typically sufficient for converged results, but defects with large unit cells or large super cells, become prohibitively expensive to simulate: the Bloch coefficients, which describe the partial intensity of specific Bloch waves, are solutions to an eigenvalue problem, whose computational complexity scales with the third power of the considered number of Bloch waves.

In multislice simulations on the other hand, the high energy beam electron wave function is numerically propagated through a super cell of the studied structure. The scattering potential is thereby divided into thin slices and the computational scheme consists of a series of transmission and propagation steps [110]. The scattering potential acts thereby as a *phase grating* in exactly the same way as it does in the POA in eq. (2.13a), effectively creating diffraction of the wave function, and the propagation step evolves the wave function through free space over the slice thickness. Compared to Bloch waves, the simulation time scales only with the total size of the system, but is not strongly affected by compositional details of the structure, which makes it ideal for studies of disordered systems, defects, nanoparticles, interfaces etc. We will explain the multislice method in detail in sec. 3.1 in connection with the description of computational methods in chapter 3.

2.4 The Frozen Phonon Multislice Method

The effect of atomic vibrations on the angular distribution of scattered electrons, i.e., the diffraction pattern $|\phi(\mathbf{q}_\perp, z)|^2$, is two-fold: the elastic scattering potential becomes thermally smeared and inelastic scattering occurs. The former leads to an exponential dampening of high-angle elastic scattering, the so-called DWF, while the latter leads to an absorption of elastic

intensity into inelastic channels. This manifests itself in a reduction of total (elastic) intensity at energy loss $\Delta E = 0$ and the missing intensity is simultaneously scattered towards angles, which do not necessarily need to coincide with Bragg angles. The inelastically scattered electrons form then a diffuse background to the elastic Bragg spots, the so-called *Thermal Diffuse Scattering* (TDS). Within the first-order Born approximation, the effects of thermal smearing and TDS are encapsulated in the 0-phonon and 1-phonon DDSCS of eq. (2.5) and (2.6), respectively².

In purely elastic imaging and diffraction calculations, the thermal smearing and absorption effects on the elastic wave can be included by applying the DWF to atomic scattering factors and considering absorptive scattering potentials [82, 83, 109]. If also the inelastic intensity, i.e., TDS, is of interest, more elaborate simulations need to be carried out. For example TDS can in principle be modeled for thick samples via the single inelastic theories outlined in sec. 2.6 below and integrating over energy loss, but the resulting calculations would require large amount of computational resources. Here we will focus on the so-called Frozen Phonon Multislice (FPMS) method [84].

The FPMS method is motivated in a semi-classical picture³ by the large difference in time scales at which the thermally averaged diffraction pattern or image is formed [109]: on one hand the time it takes a high-energy electron of 60 keV to pass a specimen of thickness 20 nm is of the order 10^{-16} s, while the typical time scale of atomic motion in the specimen due to thermal vibrations is on the order of about 10^{-12} to 10^{-13} s. Therefore the electron “sees” only one static configuration of the atomic displacements in the specimen. On the other hand, the time between two consecutive beam electrons pass the specimen is around 10^{-9} s for a beam current of 100 pA and thus much longer than the characteristic time of atomic oscillations. Each electron “sees” therefore a different, uncorrelated configuration of atomic positions of the vibrating structure, a so-called *snapshot*.

In this picture, the diffraction pattern $I_{\text{FPMS}}(\mathbf{q}_\perp, z, \mathbf{r}_p)$ is expressed as the incoherent average over N_c (independent) snapshots $\{\mathbf{R}_n\}_{n=1}^{N_c}$, i.e.,

$$I_{\text{FPMS}}(\mathbf{q}_\perp, z, \mathbf{r}_p) = \frac{1}{N_c} \sum_{n=1}^{N_c} |\phi(\mathbf{q}_\perp, z, \mathbf{r}_p, \mathbf{R}_n)|^2, \quad (2.21)$$

where $\phi(\mathbf{q}_\perp, z, \mathbf{r}_p, \mathbf{R}_n)$ is the beam exit wave function calculated using the multislice method at thickness z , with the probe centered at position \mathbf{r}_p , and atoms located at positions \mathbf{R}_n . Thus the FPMS method reduces the

²Higher-order terms with $\eta > 1$ also contribute to the TDS at any momentum transfer throughout the diffraction plane.

³Spectral modifications in Energy-Loss Near Edge Structure (ELNES) were simulated using arguments similar to the ones presented here by averaging over snapshots of molecular vibrations [111].

complexities associated with phonon scattering to a Monte-Carlo sampling of the thermally averaged intensity of elastic waves over different distorted lattice configurations. It is important to note that the frozen phonon picture has been justified on quantum mechanical grounds [109, 112–114].

Different approaches can be used to generate the snapshots $\{\mathbf{R}_n\}_{n=1}^N$, the most widely used of which is a model of uncorrelated atomic motion, also called an *Einstein model* [84]. Correlated motion, i.e., the notion of lattice modes or *phonons*, can be included either by considering a detailed phonon dispersion in the Monte-Carlo sampling [115, 116], or via Molecular Dynamics (MD) simulations [117–124]. It was shown that the total single inelastically scattered intensity is the same for the Einstein model and a more sophisticated correlated model [125]. However, diffraction patterns simulated with the FPMS method considering structure snapshots sampled from MD simulations exhibit subtle intensity variations, which are attributable to correlated atomic motion [116, 118].

The FPMS allows therefore for a great freedom in modeling atomic vibrations and the computational effort to include the effect of phonon scattering is given by the number of configurations necessary to reach convergence of the intensity $I_{\text{FPMS}}(\mathbf{q}_\perp, z, \mathbf{r}_p)$. We have observed that typically about 100-200 independent snapshots of atomic configurations give well converged averages. For the purpose of vibrational EELS, however, the FPMS method can only give estimates of the total inelastic intensity and it is not applicable to spectroscopy, since it does not provide energy resolution.

2.5 The QEP model

The Quantum Excitations of Phonons (QEP) model is derived from the many-body Schrödinger equation of the beam-sample system using an approximation akin to the BO approximation for the beam electron. The total intensity in the diffraction plane is expressed as a (incoherent) configurational average of multislice wave functions $\phi(\mathbf{q}_\perp, z, \mathbf{r}_p, \mathbf{R})$ over atomic displacements \mathbf{R} ,

$$I_{\text{incoh}}(\mathbf{q}_\perp, z, \mathbf{r}_p) = \int d\mathbf{R} |\phi(\mathbf{q}_\perp, z, \mathbf{r}_p, \mathbf{R})|^2 P(\mathbf{R}). \quad (2.22)$$

This integral is evaluated by the Monte-Carlo average in eq. (2.21) if \mathbf{R} is drawn from the probability distribution $P(\mathbf{R})$. Thus the QEP model is mathematically equivalent to the FPMS method. $P(\mathbf{R})$ is within the QEP model given in terms of the crystal states $|\mathbf{n}\rangle$, which could be simple harmonic oscillator states (Einstein model) or the phonon number states in

the harmonic approximation (c.f. appendix E), as

$$P(\mathbf{R}) = \sum_{\mathbf{n}} \frac{e^{-\beta E_{\mathbf{n}}}}{Z} |\langle \mathbf{R} | \mathbf{n} \rangle|^2. \quad (2.23)$$

Within the QEP model it is possible to define a *coherently* averaged wave

$$\bar{\psi}_{\text{coh}}(\mathbf{q}_{\perp}, z, \mathbf{r}_p) = \int d\mathbf{R} \phi(\mathbf{q}_{\perp}, z, \mathbf{r}_p, \mathbf{R}) P(\mathbf{R}), \quad (2.24)$$

which carries the notion of the elastically scattered wave [126]. Using this definition, we can extract the inelastic intensity

$$I_{\text{inel}}(\mathbf{q}_{\perp}, z, \mathbf{r}_p) = I_{\text{incoh}}(\mathbf{q}_{\perp}, z, \mathbf{r}_p) - |\bar{\psi}_{\text{coh}}(\mathbf{q}_{\perp}, z, \mathbf{r}_p)|^2, \quad (2.25)$$

which is the variance of multislice exit wave functions $\phi(\mathbf{q}_{\perp}, z, \mathbf{r}_p, \mathbf{R})$. The inelastic intensity gives the distribution of TDS in the diffraction plane. Furthermore an “inelastic wave” associated with a transition $|\mathbf{m}\rangle \rightarrow |\mathbf{n}\rangle$ can be defined as

$$\psi_{\mathbf{mn}}(\mathbf{q}_{\perp}, z, \mathbf{r}_p) = \int d\mathbf{R} \langle \mathbf{n} | \mathbf{R} \rangle \langle \mathbf{R} | \mathbf{m} \rangle \phi(\mathbf{q}, \mathbf{R}, z, \mathbf{r}_p). \quad (2.26)$$

The QEP model has been used to support interpretation of experiments showing atomic-scale contrast in vibrational EELS and to explain contrast reversal in on-axis vibrational EELS [60, 63]. Dipolar scattering was included in Ref. [63] in an approximate way by modifying the atomic scattering factor. However, in all of these calculations only a simple Einstein model of atomic displacements was considered. Furthermore, the inelastic wave in eq. (2.26) has not been considered in literature, except analytically in our paper IV, which we discuss in sec. 4.4.

Similar to the FPMS method, the QEP model offers a tractable way to obtain the *total* inelastic intensity, but spectroscopic calculations via eq. (2.26) requires explicit knowledge of phonon modes and is computationally expensive to evaluate due to the large number of states $|\mathbf{m}\rangle$ and $|\mathbf{n}\rangle$.

2.6 Single inelastic scattering theories including multiple elastic scattering

After considering how vibrational scattering can be treated in a statistical sense, we turn our attention here towards explicit spectroscopic calculations in a single inelastic scattering approximation. In order to include the multiple elastic interactions mentioned in sec. 2.3 in such simulation, one needs to compute how elastic scattering changes the wave function of the beam electrons from the initial wave function to the wave function at the

position of the inelastic interaction, and subsequently how the inelastically scattered electron wave function changes until it reaches the detector.

Such simulations have been used to study the origin of lattice resolution in on-axis vibrational EELS [127]. Bloch waves were thereby used to describe the elastic propagation and a transition potential accounts for single inelastic scattering [128], which has a similar functional dependence as the single phonon first-order Born approximation. Furthermore Dwyer has used an inelastic multislice theory including dipolar scattering to consider the prospects of spatial resolution in vibrational EELS in several works [39, 62, 129].

Both methods, inelastic Bloch wave and inelastic multislice simulations, include the effect of dynamical diffraction, are conceptually transparent, yet both require the explicit knowledge of the phonon modes of the system under study. Similar to the Bloch coefficients, the phonon modes are the solutions of an eigenvalue problem, whose numerical complexity scales as the third power of the system size, here the number of atoms. This unfavorable scaling becomes problematic for defects or other systems requiring large super cells, especially if a thermal average over the initial states of the target is to be carried out.

2.7 Towards a new method for vibrational EELS

We have reviewed in this chapter the main approaches to phonon scattering in the context of TEM and STEM, which are presently available for interpreting vibrational EELS experiments. We have considered their realm of feasible applicability and recognize, that there is an opportunity for a new approach, which combines the computational advantages of the FPMS method with frequency resolution (an energy dimension). The idea is to develop such an extension of the FPMS method, which can deal efficiently with large structures, such as defect systems, is versatile in the scattering geometries it can describe, and includes multiple elastic interaction, such that the thickness dependence of vibrational EELS can be modeled. We call this method the *Frequency Resolved Frozen Phonon Multislice* (FRFPMS) method and this dissertation is its story. In chapter 3, we will explain more of the methods on which the FRFPMS method is built and which we have used in papers I-VI. A summary and discussion of these papers is the topic of chapter 4, which includes also a detailed description of the FRFPMS method itself.

3. Simulation Methods

Consistent with the core-idea of this dissertation to develop a Frequency-Resolved Frozen Phonon Multislice (FRFPMS) method, which we have formulated at the end of chapter 2, we present in this section the computational details necessary to compute and understand the results presented in chapter 4. Starting with the multislice method we first describe in section 3.1 how the electron beam exit wave function is computed from a structure model of the specimen and an initial wave function. We proceed then with a consideration of MD simulations, specifically MD simulations based on the Generalized Langevin Equation (GLE), which allows to construct thermostats providing frequency-dependent heating of modes. In the last section, section 3.3, we describe some of the theory of phonons in the harmonic approximation and how to calculate phonon properties from first-principles.

3.1 The Multislice Method

The multislice method allows to compute the elastic scattering of a high energy electron on an assembly of atoms characterized by their scattering potential $V(\mathbf{r})$. Quantum mechanically this is commensurate to solving the Schrödinger equation

$$-\frac{\hbar^2}{2m}\nabla_{\mathbf{r}}^2\Psi(\mathbf{r}) + V(\mathbf{r})\Psi(\mathbf{r}) = E\Psi(\mathbf{r}), \quad (3.1)$$

where $\mathbf{r} = (x, y, z)$ is the position, $\Psi(\mathbf{r})$ is the wave function, and E the energy of the beam electrons. The multislice solution is based on the paraxial approximation to eq. (3.1) for high energy electrons [130], which reads

$$\frac{\partial\phi(\mathbf{r})}{\partial z} = \left[\frac{i\lambda}{4\pi} (\nabla_{xy}^2 + \tilde{\sigma}V(\mathbf{r})) \right] \phi(\mathbf{r}), \quad \tilde{\sigma} = \frac{2m_e}{\hbar^2} \quad (3.2)$$

with the initial wave vector \mathbf{k} of the wave function assumed to be parallel to the z axis and the wave function factorized as

$$\Psi(\mathbf{r}) = \phi(\mathbf{r}) \exp(2\pi iz/\lambda). \quad (3.3)$$

Here $\nabla_{xy}^2 = \frac{\partial^2}{\partial x^2} + \frac{\partial^2}{\partial y^2}$ is the Laplacian in xy directions and λ the electron wave length. In this way, the quick oscillation in z -direction is split off and

the object of principal concern is the wave function $\phi(\mathbf{r})$, which is modified by the interaction with the potential. It is worth pointing out, that in the derivation of the paraxial approximation, eq. (3.2), all backscattered electrons are neglected. Since the electron speed is a significant fraction of the speed of light at acceleration voltages of 60 to 300 keV¹, relativistic effects need to be taken into account in eq. (3.1). This can be achieved to a satisfactory degree by correcting the mass and electron wave length [130, 131] according to

$$\lambda = \frac{hc}{\sqrt{(m_0c^2 + E)^2 - m_0^2c^4}} \quad (3.4a)$$

$$m = \gamma m_0 = \frac{m_0}{\sqrt{1 - \frac{v^2}{c^2}}} = m_0 \left(1 + \frac{E}{m_0c^2}\right) \quad (3.4b)$$

where m_0 and m are the electron rest and relativistic electron mass, respectively. Furthermore λ and v are the relativistic electron wave length and velocity, respectively, and γ is the relativistic factor, and c the speed of light in vacuum.

We can find a solution to the paraxial Schrödinger equation, eq. (3.2), by considering the formal operator solution [130]

$$\phi(\mathbf{r}_\perp, z + \Delta z) = \exp \left[\int_z^{z+\Delta z} (A + B) dz' \right] \phi(\mathbf{r}_\perp, z) \quad (3.5a)$$

$$A = \frac{i\lambda}{4\pi} \nabla_{xy}^2 \quad (3.5b)$$

$$B = \frac{i\lambda}{4\pi} \tilde{\sigma} V(\mathbf{r}) \quad (3.5c)$$

where $\mathbf{r} = (\mathbf{r}_\perp, z)$ and $\mathbf{r}_\perp = (x, y)$. Equation (3.5) describes that the wave function $\phi(\mathbf{r}_\perp, z + \Delta z)$ at a certain depth $z + \Delta z$ can be computed by acting with the exponential operator of A and B on the (known) wave function $\phi(\mathbf{r}_\perp, z)$ at depth z . For small enough Δz one may factorize the exponential of the operators according to

$$\exp(A\Delta z + B\Delta z) = \exp(A\Delta z) \exp(B\Delta z) + \frac{1}{2} [B, A] (\Delta z)^2, \quad (3.6)$$

where $[B, A] = BA - AB$ is the commutator. Then eq. (3.5) can be rewritten as

$$\begin{aligned} \phi(\mathbf{r}_\perp, z + \Delta z) = & \exp \left(\frac{i\lambda}{4\pi} \Delta z \nabla_{xy}^2 \right) \times \\ & \times \exp \left(\frac{i\lambda}{4\pi} \tilde{\sigma} V_{\text{proj}}(\mathbf{r}_\perp, z, \Delta z) \right) \phi(\mathbf{r}_\perp, z) \end{aligned} \quad (3.7)$$

¹The relativistic speed of 60 keV electrons is about 0.45c, while 300 keV electrons travel at a speed of about 0.78c.

up to an error of order $(\Delta z)^2$ for a sufficiently small value of the projected potential

$$V_{\text{proj}}(\mathbf{r}_\perp, z, \Delta z) = \int_z^{z+\Delta z} V(\mathbf{r}_\perp, z') dz'. \quad (3.8)$$

Note that the product of the exponential of the projected potential and the wave after the previous slice in the second row of eq. (3.7) is equivalent to the POA, c.f. eq. (2.13a), albeit with the projected slice potential instead of the projected potential of the entire crystal. Equation (3.7) is the solution to the scattering problem and exposes the core of the method: the scattering potential of the specimen is divided into N_s thin slices of thicknesses $\Delta z_n, n = 1, \dots, N_s^2$. Within these slices, it is assumed, that the projected potential is sufficiently small and the wave function is then propagated in an iterative process from the crystal entrance surface at $z = 0$ to the crystal exit surface at $z = \sum_{n=1}^{N_s} \Delta z_n$ by repeated application of eq. (3.7). The propagation itself is thereby represented as an alternating sequence of scattering at the interface of the slices and free-space propagation between slices.

We will now see how the multislice method is implemented in practice and discuss thereby two different evaluation algorithms. The first one is the so-called Conventional Multislice (CMS) method [110] and its solution reads

$$\phi_{n+1}(\mathbf{r}_\perp) = p(\mathbf{r}_\perp, \Delta z_{n+1}) \otimes [t_{n+1}(\mathbf{r}_\perp) \phi_n(\mathbf{r}_\perp)], \quad (3.9)$$

where \otimes denotes the convolution operation. It follows from considering the Fourier transform of eq. (3.7) and realizing via application of the convolution theorem, that it describes a convolution of the real space propagator function [130]

$$p(\mathbf{r}_\perp, \Delta z_n) = \frac{1}{i\lambda\Delta z_n} \exp\left(\frac{i\pi}{\lambda\Delta z_n} \mathbf{r}_\perp^2\right) \quad (3.10)$$

with the product of the transmission function

$$t_{n+1}(\mathbf{r}_\perp) = \exp\left[\frac{i\lambda}{4\pi} \tilde{\sigma} V_{n+1}(\mathbf{r}_\perp)\right] \quad (3.11)$$

with the wave function $\phi_n(\mathbf{r}_\perp)$ of the previous slice. We have used the notation

$$\begin{aligned} \phi_n(\mathbf{r}_\perp) &= \phi(\mathbf{r}_\perp, z_n) \\ V_{n+1}(\mathbf{r}_\perp) &= V_{\text{proj}}(\mathbf{r}_\perp, z_n, \Delta z_n) \\ z_n &= \sum_{m=1}^n \Delta z_m \\ z_0 &= 0 \end{aligned}$$

and $\phi_0(\mathbf{r}_\perp)$ is taken to be the initial wave function. Equation (3.10) expresses, that the CMS solution is obtained by repeatedly multiplying the

²The slices do not necessarily need to have the same thickness.

wave function by the transmission function and convolving the result with the propagator function. The convolution is conventionally implemented by Fourier transforming the term, multiplying by the Fourier transform of the propagator function

$$\text{FT}[p(\mathbf{r}_\perp, \Delta z_n)] = \exp(-i\pi\lambda\mathbf{k}_\perp^2\Delta z_n) \quad (3.12)$$

and applying the inverse FT. The Fast Fourier Transform (FFT) makes this procedure an efficient algorithm [105, 132]. Furthermore it should be noted, that the factorization in eq. (3.6) is only one of many possible. There exists in fact a whole hierarchy of multislice methods derived from expansions of the operator exponential in orders of λ , which differ in computational complexity as well as accuracy [133, 134].

Such expansion of the exponential in eq. (3.2) in powers of λ together with an exclusive evaluation of all expressions in real space is the defining feature of the Real Space Multislice (RSMS) method [134–137]. We follow the derivation in Cai *et al.* [138] and start with the iterative form of eq. (3.2), i.e.,

$$\phi_{n+1}(\mathbf{r}_\perp) = \exp\left[\frac{i\lambda}{4\pi}\{\Delta z_{n+1}\nabla_{xy}^2 + \tilde{\sigma}\Delta V_{n+1}(\mathbf{r}_\perp)\}\right]\phi_n(\mathbf{r}_\perp). \quad (3.13)$$

The RSMS solution is obtained by computing

$$\phi_{n+1}(\mathbf{r}_\perp) = \sum_{m=0}^{\infty} \frac{1}{m!} \left[\frac{i\lambda}{4\pi}\{\nabla_{xy}^2 + \tilde{\sigma}V_{n+1}(\mathbf{r}_j)\}\right]^m \phi_n(\mathbf{r}_\perp). \quad (3.14)$$

The derivatives in eq. (3.14) can be evaluated by finite difference methods and within one slice the following iteration is carried out

$$\phi_{n+1}^{m+1}(\mathbf{r}_\perp) = \frac{1}{m} \left[\frac{i\lambda}{4\pi}\right] \{\nabla_{xy}^2 + \tilde{\sigma}V_{n+1}(\mathbf{r}_j)\} \phi_{n+1}^m(\mathbf{r}_\perp), \quad (3.15)$$

where $\phi_{n+1}^0(\mathbf{r}_\perp) = \phi_n(\mathbf{r}_\perp)$ and $\phi_{n+1}(\mathbf{r}_\perp) = \sum_{m=0}^{\infty} \phi_{n+1}^m(\mathbf{r}_\perp)$. Note, that in order for this expansion to converge for finite m , the potential still needs to be divided into slices Δz_i in the RSMS method, since the size of the product $\lambda V_{n+1}(\mathbf{r}_j)$ depends on the slice thickness, especially near nuclei, and the series may not converge for too thick slices.

From a practical point of view the wave functions are represented on a two dimensional numerical grid of size $N_x \times N_y$ in multislice methods. An initial wave function $\phi_0(\mathbf{r}_\perp)$ determined by the details of the experiment and instrument is required in both methods, CMS and RSMS. In this thesis we consider two choices for $\phi_0(\mathbf{r}_\perp)$ (excluding aberrations):

$$\begin{aligned} \text{parallel illumination: } \phi_0(\mathbf{r}_\perp) &= \frac{1}{\sqrt{N_x N_y}} \\ \text{convergent beam: } \phi_0(\mathbf{r}_\perp) &\propto \text{FT}^{-1}[\exp(i\mathbf{k} \cdot \mathbf{r}_p)A(\mathbf{k})] \end{aligned} \quad (3.16)$$

where vector quantities in bold face are defined in the xy plane, i.e., the wave vector $\mathbf{k} = (k_x, k_y)$ and the probe position $\mathbf{r}_p = (r_{px}, r_{py})$. $A(\mathbf{k})$ is the aperture function determined by the convergence angle α , i.e.,

$$A(\mathbf{k}) = \begin{cases} 1 & \text{if } \lambda|\mathbf{k}| \leq 2\pi\alpha \\ 0 & \text{else} \end{cases}. \quad (3.17)$$

We see that the RSMS method requires a double iteration, one over slices similar to the CMS method and one within each slice, unlike the CMS method. The RSMS is more accurate than the CMS method for the same slice thickness and may be faster than the CMS method if slice thickness is reduced [138]. The RSMS method offers an additional advantage for large, disordered structures, as its computational complexity scales with the number of pixels $N = N_x \times N_y$ instead of the $N \log_2 N$ scaling of the CMS method [139].

The last topic to be considered in this section is the scattering potential $V(\mathbf{r})$ or rather its projection according to eq. (3.8). Usually the Independent Atom Model (IAM) is assumed (c.f. appendix F), with which the projected potential reads

$$V_{\text{proj}}(\mathbf{r}_\perp, z, \Delta z) = -\frac{2\pi\hbar^2}{m_e} \int_z^{z+\Delta z} dz \int_{-\infty}^{\infty} \frac{d\mathbf{q}}{(2\pi)^3} e^{i\mathbf{q}\cdot\mathbf{r}} \times \sum_{\kappa} e^{-i\mathbf{q}\cdot\mathbf{R}_\kappa} f_{e,\kappa}(q). \quad (3.18)$$

If the projected potential is calculated from the contributions of all atoms within z and $z + \Delta z$, it is often called a *3D-potential* approach in the context of multislice calculations. However more often the so-called *projection approximation* is assumed and the entire potential of a single atom is projected into its associated slice at thickness z . The projected scattering potential reads then

$$V_{\text{proj}}(\mathbf{r}_\perp, z, \Delta z) = -\frac{2\pi\hbar^2}{m_e} \int_{-\infty}^{\infty} \frac{d\mathbf{q}_\perp}{(2\pi)^2} \times \sum_{\substack{\kappa \\ z_\kappa \in [z, z+\Delta z]}} e^{i\mathbf{q}_\perp \cdot (\mathbf{r}_\perp - \mathbf{R}_{\perp\kappa})} f_{e,\kappa}(q_\perp), \quad (3.19)$$

where the sum goes only over those atoms, that are part of the slice (c.f. eq. (2.14)). We explain in appendix F, that the IAM assumes, that the charge density associated with atom κ , is the charge density of the corresponding *free* atom and bonding effects are therefore neglected.

The electron atomic scattering factors $f_{e,\kappa}(q_\perp)$ can be obtained from X-ray scattering factors via the Mott-Bethe formula in eq. (F.10) or interpolated from first principles relativistic electronic structure calculations [130,

140–142]. For ionic materials, in which charge transfer between atoms is significant, ionic scattering potentials should be used [143–145]. More generally, all bonding effects can be included in the scattering potential $V(\mathbf{r})$ by abandoning the IAM and using DFT calculations to compute $V(\mathbf{r})$ directly [146–154].

In this section we have considered how to compute the electron beam exit wave function for a static specimen. In reality atoms oscillate around their equilibrium positions and we have described in sec. 2.4 and 2.5 that the FPMS and QEP methods can be used to include the effects of thermal motion using multislice wave functions computed for distorted atomic structure “snapshots”. In the following section, we will consider MD simulations, which can be used to model correlated atomic motion and generate snapshots for FPMS/QEP simulations.

3.2 Molecular Dynamics Simulations

In classical MD simulations the classical equations of motion³

$$\dot{r} = \frac{p}{m}, \quad (3.20a)$$

$$\dot{p} = -V'(r), \quad (3.20b)$$

are integrated in time for atoms inside a virtual so-called simulation box. r is thereby the position, p is the momentum and $V'(r)$ the gradient of the Interatomic Potential (IAP). The potential $V(r)$ is the BO surface (c.f. appendix E), which can be approximated to varying degree. In so-called *ab-initio* MD simulations, $V(r)$ is directly obtained from first-principles calculations of the electronic structure such as Density Functional Theory (DFT). *Ab-initio* MD requires a large amount of computational resources and for large-scale simulations one usually defers to an empirical form of the IAP, which has been fit to material properties. Examples of such potentials for hBN are the Tersoff, extended Tersoff, and diverse interlayer potentials [156–160]. Advances in machine learning have also swept into the field of IAP development and there is an ever growing number of so-called Machine Learned Interatomic Potentials (MLIPs) available today, which are designed to faithfully reproduce the BO surface calculated by DFT or other electronic structure methods [161]. One of the main problems in applying MD simulations to solids is, that one conventionally requires a potential, which is specifically trained for the material under study. To address this issue so-called *universal* MLIPs are being developed, which are trained on large amounts of electronic structure calculations of

³In this chapter, we will change the style of notation in accordance with the notation in Ref. [155]. In particular, we will write the equations of motion in a 1D form for one atom, but the generalization to 3D and N atoms is straightforward.

many different materials and promise to be applicable to any combination of a range of elements with good accuracy [162–164].

The result of MD simulations are trajectories $(r(t), p(t))$, which represent the time evolution of the system and which can be viewed as sequences of samples of phase space (r, p) via the ergodic hypothesis [165]. The simulation box satisfies certain boundary conditions, usually periodic boundary conditions, and is required in order to ascribe a volume and pressure to the system. By default, equations (3.20) produce dynamics consistent with a so-called *micro-canonical* or *NVE* ensemble⁴, since the total energy E is conserved in the system for a conservative potential $V(r)$. In order to simulate thermodynamical ensembles involving a constant temperature T , so-called *thermostats* need to be used, which are effectively modifications of the equations of motion in eq. (3.20).

Dynamics producing a canonical (*NVT*) ensemble⁵, can be achieved, for example, by introducing additional artificial degrees of freedom in eq. (3.20), an approach developed by Nosé and Hoover [166, 167]. Temperature regulation can, however, also be achieved by introducing friction and stochastic noise forces acting on the atoms in the simulation. A popular thermostat of this kind is the so-called *Langevin* thermostat based on the Langevin equation [168]

$$\begin{aligned}\dot{r} &= p/m \\ \dot{p} &= -V'(r) - a_{pp} p + b_{pp} \xi(t),\end{aligned}\tag{3.21}$$

where ξ is a time-dependent, Gaussian-distributed random noise, a_{pp} is the friction coefficient, and b_{pp} is the strength of the random force term. The random noise is delta-correlated $\langle \xi(t)\xi(0) \rangle = \delta(t)$, has mean value $\langle \xi \rangle = 0$ and the system is Markovian, thus fully determined by the state $(r(t), p(t))$ at time t . Setting

$$b_{pp}^2 = 2 a_{pp} k_B T,\tag{3.22}$$

where k_B is the Boltzmann constant, the Langevin equation fulfills the classical Fluctuation Dissipation Theorem (FDT) and samples the *NVT* ensemble of classical statistical mechanics [169, 170]. In the calculations for the papers included in this thesis, a Langevin thermostat as implemented in LAMMPS is used for all *NVT* simulations [171, 172].

But one can take a step further and use the non-Markovian GLE [155]

$$\begin{aligned}\dot{r} &= \frac{p}{m} \\ \dot{p} &= -V'(r) - \int_{-\infty}^t K(t-s)p(s) ds + \zeta(t)\end{aligned}\tag{3.23}$$

⁴*NVE*: constant number of particles N , constant volume V , and constant total energy E

⁵*NVT*: constant number of particles N , constant volume V , and constant temperature T

where $K(t-s)$ is a memory kernel, which governs the history dependence of the friction force and $\zeta(t)$ is a colored-noise force. Non-Markovian systems are not easily implemented in simulations, since their state depends on the *history* of the system and is not uniquely determined by the current values of $(r(t), p(t))$. It can, however, be shown that the non-Markovian system described by equation (3.23) is equivalent to the Markovian system [155]

$$\dot{r} = \frac{p}{m}$$

$$\begin{pmatrix} \dot{p} \\ \dot{\mathbf{s}} \end{pmatrix} = \begin{pmatrix} -V'(r) \\ \mathbf{0} \end{pmatrix} - \begin{pmatrix} a_{pp} & \mathbf{a}_p^T \\ \bar{\mathbf{a}}_p & \mathbf{A} \end{pmatrix} \begin{pmatrix} p \\ \mathbf{s} \end{pmatrix} + \begin{pmatrix} b_{pp} & \mathbf{b}_p^T \\ \bar{\mathbf{b}}_p & \mathbf{B} \end{pmatrix} \begin{pmatrix} \xi \end{pmatrix}, \quad (3.24)$$

where $\mathbf{s} = \{s_i\}$ are n auxiliary momenta and ξ is a vector of $n + 1$ uncorrelated Gaussian random numbers. The parameters a_{pp} , \mathbf{a}_p^T , $\bar{\mathbf{a}}_p$, \mathbf{A} , b_{pp} , \mathbf{b}_p^T , $\bar{\mathbf{b}}_p$, and \mathbf{B} are related to the memory kernel $K(t-s)$ of the non-Markovian system and provide the flexibility to adapt the GLE for a wide array of thermostating applications [168]. Not all applications require the same number of auxiliary variables n , as different memory kernels are only well approximated for an appropriate choice of n . We define the following matrices in order to simplify the notation in the remainder of this section

$$\mathbf{A}_p = \begin{pmatrix} a_{pp} & \mathbf{a}_p^T \\ \bar{\mathbf{a}}_p & \mathbf{A} \end{pmatrix}$$

$$\mathbf{B}_p = \begin{pmatrix} b_{pp} & \mathbf{b}_p^T \\ \bar{\mathbf{b}}_p & \mathbf{B} \end{pmatrix}. \quad (3.25)$$

Furthermore \mathbf{A}_p and \mathbf{B}_p are related via the static covariance matrix \mathbf{C}_p

$$\mathbf{A}_p \mathbf{C}_p + \mathbf{C}_p \mathbf{A}_p^T = \mathbf{B}_p \mathbf{B}_p^T \quad (3.26)$$

and it can be shown that the GLE satisfies the classical FDT for $\mathbf{C}_p = k_B T \mathbf{1}$, where $\mathbf{1}$ is the identity matrix [168].

We have described that the idea of the FRFPMS method is to develop a *frequency-resolved* FPMS method. We will see in chapter 4, that one way to implement the frequency-resolution requires the ability to obtain snapshots of the vibrating structure at different frequencies. This idea of using snapshots of the vibrating structure at different frequencies to model vibrational EELS was actually the starting point for the work presented in this dissertation. It originally stems from the coincidental finding of the so-called δ -thermostat in the literature [173] while researching a so-called *quantum thermostat* for a different work [121, 174]. The idea of the δ -thermostat can be motivated as follows: consider the following choice of

matrices

$$\mathbf{A}_p = \begin{pmatrix} 0 & \sqrt{\frac{\gamma}{2\pi}} & \sqrt{\frac{\gamma}{2\pi}} \\ -\sqrt{\frac{\gamma}{2\pi}} & \Delta\omega & \omega_0 \\ -\sqrt{\frac{\gamma}{2\pi}} & -\omega_0 & \Delta\omega \end{pmatrix} \quad (3.27)$$

$$\mathbf{B}_p \mathbf{B}_p^T = k_B T (\mathbf{A}_p + \mathbf{A}_p^T),$$

which produces a δ -like memory kernel but still samples the canonical ensemble due to it fulfilling the classical FDT [175]. If the a_{pp} element in the leftmost column of the top row of matrix \mathbf{A}_p is replaced by a finite friction parameter γ' , without applying the change to the matrix $\mathbf{B}_p \mathbf{B}_p^T$, however, the FDT is broken. Therefore the resulting thermostat does not sample an equilibrium ensemble, but the thermostat will affect mostly vibrational modes with frequencies close to ω_0 . The finite friction γ' will on the other hand dissipate energy from all modes equally, effectively freezing those modes, whose frequencies are not close to ω_0 . This is the idea of the δ -thermostat. It should be noted, that the final matrices \mathbf{A}_p and \mathbf{B}_p of the δ -thermostat cannot be written in the form of eq. (3.27) [175]. Rather they are obtained by a fitting procedure and can be downloaded from an online repository ⁶. We have used the δ -thermostat in paper I and discussed its advantages and disadvantages for our purposes in paper II.

Another frequency-dependent thermostat, the so-called *hotspot* thermostat, is provided by the choice

$$\mathbf{A}_p = \begin{pmatrix} \gamma_{\text{base}} & \sqrt{\frac{\gamma_{\text{peak}} \omega_{\text{peak}}}{2\pi}} & 0 \\ -\sqrt{\frac{\gamma_{\text{peak}} \omega_{\text{peak}}}{2\pi}} & \Delta\omega & \omega_{\text{peak}} \\ 0 & -\omega_{\text{peak}} & 0 \end{pmatrix}, \quad (3.28)$$

$$\mathbf{B}_p \mathbf{B}_p^T = \begin{pmatrix} 2T_{\text{base}} \gamma_{\text{base}} & 0 & 0 \\ 0 & 2T_{\text{peak}} \Delta\omega & 0 \\ 0 & 0 & 0 \end{pmatrix}.$$

This thermostat equilibrates effectively all modes at a temperature T_{base} and injects also kinetic energy corresponding to a temperature T_{peak} into modes, whose frequency lies (at least approximately) within an interval of $\Delta\omega$ around ω_{peak} . The selectable frequency-width $\Delta\omega$ provides advantages for our purposes as detailed in paper II.

In order to judge the frequency profile of thermostats and in order to calculate the PDOS from MD simulations, we need to extract the relative contribution of different frequencies to the motion encoded in a MD trajectory. In the methods section of paper II, we consider the topic of determining the vibrational spectrum from MD simulations in detail. The basic

⁶<http://gle4md.org/index.html?page=matrix>, accessed: 2023-12-06

equation reads

$$g(\omega) = \int_{-\infty}^{\infty} dt \frac{\sum_{n=1}^{N_{\text{at}}} m_n \langle \mathbf{v}_n(t) \mathbf{v}_n(0) \rangle_T}{\sum_{n=1}^{N_{\text{at}}} m_n \langle \mathbf{v}_n(0) \mathbf{v}_n(0) \rangle_T} \exp(i\omega t), \quad (3.29)$$

which is the normalized FT of the velocity-velocity autocorrelation function $\langle \mathbf{v}_n(t) \mathbf{v}_n(0) \rangle_T$, and m_n is the mass of the n -th atom. It can be shown that the procedure described by eq. (3.29) yields the PDOS for NVE dynamics [176, 177]. We call eq. (3.29) without normalization the Vibrational Power Spectrum (VPS)

$$\text{VPS}(\omega) = \int_{-\infty}^{\infty} dt \sum_{n=1}^{N_{\text{at}}} m_n \langle \mathbf{v}_n(t) \mathbf{v}_n(0) \rangle \exp(i\omega t) \quad (3.30)$$

and if the sum in eq. (3.29) is only extended over a certain subset of the atoms, we speak of the Local Phonon Density of States (LPDOS) at those atoms. In practice eq. (3.30) and for that matter also eq. (3.29) is most easily evaluated using the FT $\mathbf{v}_n(\omega)$ of the velocity trajectory $\mathbf{v}_n(t)$

$$\text{VPS}(\omega) = \sum_{n=1}^{N_{\text{at}}} m_n |\mathbf{v}_n(\omega)|^2. \quad (3.31)$$

In the following section, we will see how we can obtain phonon dispersions and the PDOS from the MD force field or any other model of the BO surface.

3.3 Phonon theory and calculations

Phonons are the quasi-particles of vibrational excitations in solids. They are characterized by the phonon branch ν and the wave vector in the first Brillouin zone \mathbf{k}_0 . Generally, the Hamiltonian of the nuclei in a crystal can be written as (c.f. appendix B and E)

$$\begin{aligned} \hat{H}_{\text{nuc}} &= \sum_{j,l=1}^{N_{\text{ba}}, N_{\text{uc}}} \frac{\hat{\mathbf{p}}_{jl}^2}{2m_j} + E_{\text{BO}}(\{\mathbf{R}_{jl}\}) \\ &\approx \sum_{j,l=1}^{N_{\text{ba}}, N_{\text{uc}}} \frac{\hat{\mathbf{p}}_{jl}^2}{2m_j} + E_{\text{BO}}(\{\mathbf{R}_{jl}^0\}) + \frac{1}{2} \sum_{l,l'=1}^{N_{\text{uc}}} \sum_{j,j'=1}^{N_{\text{ba}}} \hat{\mathbf{U}}_{jl}^T \Phi_{jj'}^{ll'} \hat{\mathbf{U}}_{j'l'}, \end{aligned} \quad (3.32)$$

where we assume the *harmonic approximation* [93], i.e., we expand the BO surface $E_{\text{BO}}(\{\hat{\mathbf{R}}_{jl}\})$ in powers of the displacements $\hat{\mathbf{U}}_{jl}$ of the j -th basis

atoms in the l -th unit cells around their equilibrium positions $\hat{\mathbf{R}}_{jl}^0$ and terminate after the harmonic term. The constant term $E_{\text{BO}}(\{\mathbf{R}_{jl}^0\})$ is an additive constant, which can be safely set to zero in the following⁷ and the term linear in the displacements vanishes due to vanishing forces on atoms at their equilibrium positions. We have assumed here a crystal of N_{uc} unit cells with N_{ba} atoms in the basis. Furthermore the Hessian of the BO surface evaluated with all atoms in their equilibrium positions, i.e.,

$$\Phi_{jj'}^{ll'} = \left. \frac{\partial^2 E_{\text{BO}}(\{\mathbf{R}_{jl}\})}{\partial \mathbf{R}_{jl} \partial \mathbf{R}_{j'l'}} \right|_{\{\mathbf{R}_{jl}^0\}} \quad (3.33)$$

is a 3×3 matrix for each combination (j, j', l, l') , which is usually called the *force constant matrix*. It describes essentially the direction and magnitude of the change in force felt by an atom jl due to a displacement of atom $j'l'$.

The equation of motion for the atoms in one unit cell $l = 1$ becomes via Newton's second law

$$m_j \omega_{\mathbf{k}_0\nu}^2 \epsilon_{\mathbf{k}_0\nu}^j = \sum_{j'=1}^{N_{\text{basis}}} \mathcal{D}_{jj'}(\mathbf{k}_0) \epsilon_{\mathbf{k}_0\nu}^{j'} \quad (3.34)$$

where the $\mathcal{D}_{jj'}(\mathbf{k}_0)$ is a 3×3 matrix, the so-called *dynamical matrix*, which reads

$$\mathcal{D}_{jj'}(\mathbf{k}_0) = \frac{1}{\sqrt{m_j m_{j'}}} \sum_{l'} \Phi_{jj'}^{ll'} \exp(i\mathbf{k}_0 \cdot (\mathbf{R}_{jl'}^0 - \mathbf{R}_{j1}^0)). \quad (3.35)$$

Equation (3.34) defines an eigenvalue problem, which can be solved by diagonalization. Therefore the phonon polarization vectors $\epsilon_{j\mathbf{k}_0\nu}$ are the eigenvectors and the phonon frequencies $\omega_{\mathbf{k}_0\nu}$ are the eigenvalues of the dynamical matrix. The phonon polarization vector is chosen to satisfy the orthonormalization conditions

$$\sum_{j=1}^{N_{\text{ba}}} \epsilon_{j\mathbf{k}_0\nu} \epsilon_{j\mathbf{k}_0\nu'}^* = \delta_{\nu\nu'} \quad (3.36a)$$

$$\sum_{\nu=1}^{3N_{\text{ba}}} \epsilon_{\alpha j\mathbf{k}_0\nu} \epsilon_{\beta j'\mathbf{k}_0\nu}^* = \delta_{\alpha\beta} \delta_{jj'}, \quad (3.36b)$$

where $\epsilon_{\alpha j\mathbf{k}_0\nu}$ denotes the α -th cartesian component of the phonon polarization vector.

⁷Note: as a constant energy shift, $E_{\text{BO}}(\{\mathbf{R}_{jl}^0\})$ does not influence the calculation of thermodynamic averages of the form $\frac{1}{Z} \sum e^{-\beta(E_{\text{n}} + E_{\text{BO}}(\{\mathbf{R}_{jl}^0\}))}$, due to cancellation with part of the partition function Z .

The displacements are expanded in normal modes ($\mathbf{k}_0\nu$) [178, 179]

$$\hat{\mathbf{U}}_{jl}(t) = \sqrt{\frac{\hbar}{2N_{\text{uc}}m_j}} \sum_{\mathbf{k}_0,\nu} e^{i\mathbf{k}_0 \cdot \mathbf{R}_{jl}^0} \boldsymbol{\epsilon}_{j\mathbf{k}_0\nu} \hat{u}_{\mathbf{k}_0\nu}(t), \quad (3.37)$$

where the phonon wave vectors \mathbf{k}_0 are defined in the first Brillouin zone, ν is the band index, and m_j is the mass and $\boldsymbol{\epsilon}_{j\mathbf{k}_0\nu}$ the phonon polarization vector of the j -th basis atom. Furthermore $\hat{u}_{\mathbf{k}_0\nu}(t)$ is a time dependent “displacement” operator of the normal mode ($\mathbf{k}_0\nu$)⁸, which reads in the language of second quantisation

$$\hat{u}_{\mathbf{k}_0\nu}(t) = \frac{1}{\sqrt{\omega_{\mathbf{k}_0\nu}}} \left[\hat{a}_{\mathbf{k}_0\nu} e^{-i\omega_{\mathbf{k}_0\nu}t} + \hat{a}_{-\mathbf{k}_0\nu}^\dagger e^{i\omega_{\mathbf{k}_0\nu}t} \right]. \quad (3.38)$$

The phonon creation and annihilation operators $\hat{a}_{\mathbf{k}_0\nu}$ and $\hat{a}_{\mathbf{k}_0\nu}^\dagger$, respectively, satisfy

$$\hat{a}_{\mathbf{k}_0\nu} |n_{\mathbf{k}_0\nu}\rangle = \sqrt{n_{\mathbf{k}_0\nu}} |n_{\mathbf{k}_0\nu} - 1\rangle \quad (3.39a)$$

$$\hat{a}_{\mathbf{k}_0\nu}^\dagger |n_{\mathbf{k}_0\nu}\rangle = \sqrt{n_{\mathbf{k}_0\nu} + 1} |n_{\mathbf{k}_0\nu} + 1\rangle \quad (3.39b)$$

$$[\hat{a}_{\mathbf{k}_0\nu}, \hat{a}_{\mathbf{k}'_0\nu'}^\dagger] = \delta_{\mathbf{k}_0\mathbf{k}'_0} \delta_{\nu\nu'} \quad (3.39c)$$

$$\hat{a}_{\mathbf{k}_0\nu}^\dagger \hat{a}_{\mathbf{k}_0\nu} |n_{\mathbf{k}_0\nu}\rangle = n_{\mathbf{k}_0\nu} |n_{\mathbf{k}_0\nu}\rangle \quad (3.39d)$$

$$\hat{a}_{\mathbf{k}_0\nu} \hat{a}_{\mathbf{k}_0\nu}^\dagger |n_{\mathbf{k}_0\nu}\rangle = (n_{\mathbf{k}_0\nu} + 1) |n_{\mathbf{k}_0\nu}\rangle, \quad (3.39e)$$

where $|n_{\mathbf{k}_0\nu}\rangle$ is a Fock-state, which is occupied by $n_{\mathbf{k}_0\nu}$ phonons. We can express the total eigenstate of the system in harmonic approximation as

$$|\mathbf{n}\rangle := \prod_{\mathbf{k}_0\nu} \frac{1}{\sqrt{n_{\mathbf{k}_0\nu}!}} (\hat{a}_{\mathbf{k}_0\nu}^\dagger)^{n_{\mathbf{k}_0\nu}} |\mathbf{0}\rangle \quad (3.40)$$

where $|\mathbf{0}\rangle$ is the *vacuum* state and $\mathbf{n} = (n_{\mathbf{k}_{01}1}, n_{\mathbf{k}_{01}2}, \dots)$ is a vector of the $3N_{\text{uc}}N_{\text{ba}}$ phonon occupation numbers $n_{\mathbf{k}_0\nu}$. The Hamiltonian can then be rewritten in terms of the phonon creation and annihilation operators as

$$\hat{H}_{\text{nuc}} = \sum_{\mathbf{k}_0\nu} \hbar\omega_{\mathbf{k}_0\nu} \left(\hat{a}_{\mathbf{k}_0\nu}^\dagger \hat{a}_{\mathbf{k}_0\nu} + \frac{1}{2} \right), \quad (3.41)$$

and the state $|\mathbf{n}\rangle$ is an energy eigenstate of the Hamiltonian, which satisfies

$$\hat{H}_{\text{nuc}} |\mathbf{n}\rangle = E_{\mathbf{n}} |\mathbf{n}\rangle, \quad (3.42a)$$

$$E_{\mathbf{n}} = \sum_{\mathbf{k}_0\nu} \hbar\omega_{\mathbf{k}_0\nu} \left(n_{\mathbf{k}_0\nu} + \frac{1}{2} \right). \quad (3.42b)$$

⁸ $\hat{u}_{\mathbf{k}_0\nu}(t)$ does not have the unit of length, so it is not a measure of a physical displacement of an atom, but rather how much the oscillator of mode ($\mathbf{k}_0\nu$) is displaced.

We note some further properties of the quantities we have introduced here. The displacement operator needs to be hermitian, since it is an observable of the system. This condition

$$\hat{\mathbf{U}}_{jl}(t) = \hat{\mathbf{U}}_{jl}^\dagger(t) \quad (3.43)$$

implies that the phonon polarization vectors need to satisfy

$$\boldsymbol{\epsilon}_{j\mathbf{k}_0\nu} = \boldsymbol{\epsilon}_{j-\mathbf{k}_0\nu}^*, \quad (3.44)$$

i.e., the phonon polarization vector at reciprocal lattice point \mathbf{k}_0 is the complex conjugate of the polarization vector at $-\mathbf{k}_0$. The phonon frequencies satisfy furthermore

$$\omega_{\mathbf{k}_0\nu} = \omega_{-\mathbf{k}_0\nu}. \quad (3.45)$$

Other important quantities for our purposes are thermal averages $\langle \dots \rangle_T$, which become

$$\langle \dots \rangle_T = \frac{1}{Z} \sum_{\mathbf{n}} e^{-\beta E_{\mathbf{n}}} \langle \mathbf{n} | \dots | \mathbf{n} \rangle, \quad (3.46)$$

where the partition function reads

$$Z = \sum_{\mathbf{n}} e^{-\beta E_{\mathbf{n}}}. \quad (3.47)$$

Examples of these are the phonon occupation number

$$\langle n_{\mathbf{k}_0\nu} \rangle_T = \frac{1}{e^{\beta \hbar \omega(\mathbf{k}_0\nu)} - 1}, \quad (3.48)$$

the Mean-Square Displacement (MSD)

$$\langle \hat{\mathbf{U}}_{jl}^\dagger(t) \hat{\mathbf{U}}_{jl}(t) \rangle_T = \frac{\hbar}{2N_{\text{uc}} m_j} \sum_{\mathbf{k}_0, \nu} \frac{1 + 2\langle n_{\mathbf{k}_0\nu} \rangle_T}{\omega_{\mathbf{k}_0\nu}} |\boldsymbol{\epsilon}_{j\mathbf{k}_0\nu}|^2, \quad (3.49)$$

and the *projected* MSD

$$\langle (\mathbf{e} \cdot \hat{\mathbf{U}}_{jl}^\dagger(t)) (\mathbf{e} \cdot \hat{\mathbf{U}}_{jl}(t)) \rangle_T = \frac{\hbar}{2N_{\text{uc}} m_j} \sum_{\mathbf{k}_0, \nu} \frac{1 + 2\langle n_{\mathbf{k}_0\nu} \rangle_T}{\omega_{\mathbf{k}_0\nu}} |\mathbf{e} \cdot \boldsymbol{\epsilon}_{j\mathbf{k}_0\nu}|^2, \quad (3.50)$$

where \mathbf{e} is a unit vector denoting the projection direction.

We have seen in the introduction, that vibrational EELS provides access to a variety of phonon properties, among others, the (projected) PDOS and the phonon dispersion. We consider briefly how these quantities are defined. The atom-projected PDOS reads

$$g_j(\omega, \mathbf{e}) = \frac{1}{N_{\text{uc}}} \sum_{\mathbf{k}_0\nu} \delta(\omega - \omega_{\mathbf{k}_0\nu}) |\mathbf{e} \cdot \boldsymbol{\epsilon}_{j\mathbf{k}_0\nu}|^2. \quad (3.51)$$

The local projected PDOS is a measure of how much the j -th basis atom partakes in vibrational modes along the direction of unit vector \mathbf{e} as a function of frequency. The sum of the local projected PDOS along the three spatial dimensions and over all basis atoms is the total PDOS

$$g(\omega) = \sum_{\mathbf{e}=\hat{x},\hat{y},\hat{z}} \sum_j g_j(\omega, \mathbf{e}) = \frac{1}{N_{\text{uc}}} \sum_{\mathbf{k}_0\nu} \delta(\omega - \omega_{\mathbf{k}_0\nu}). \quad (3.52)$$

After briefly considering the theory surrounding phonons, we see, that the phonon frequencies and polarizations are the only quantities, which we will need to determine for a material in order to evaluate any of the expressions in this section. Therefore the main job in a phonon calculation is to diagonalize the dynamical matrix. In turn this requires to calculate the force constant matrix. One of two approaches is commonly employed in the literature: either the dynamical matrix is obtained using DFPT, where one perturbatively considers the effect displacements on the electronic structure, or one can use a *finite* displacement method, which works with any calculation method able to provide a model of the BO surface. We will focus here on the finite displacement method as it is this method we use in connection with MD IAPs.

The basic idea of the finite displacement method is to assemble the force constant matrix $\Phi_{jj'}^{ll'}$ atom pair by atom pair. The j -th atom in the basis is thereby displaced by a small distance $\Delta\mathbf{R}_{jl}$ and the change in the force $\Delta\mathbf{F}_{j'l'}$ on all other atoms $j'l'$ caused by the displacement is calculated. For a small enough displacement the force constants can then be obtained by the finite difference⁹

$$\Phi_{jj'}^{ll'} \simeq \frac{\Delta\mathbf{F}_{j'l'}}{\Delta\mathbf{R}_{jl}}. \quad (3.53)$$

This procedure requires generally a sufficiently large super cell for converged results, since several orders of nearest-neighbor interactions need to be included. Once all force constants are known, the dynamical matrix can be assembled and diagonalized, which yields the phonon frequencies and polarizations. This approach is used by the `phonopy` software [180], which we use together with the `phonolammps`¹⁰ package.

⁹The division of vector quantities is here to be understood as $\Phi_{\alpha\beta} = \frac{\Delta F_\beta}{\Delta r_\alpha}$, where α and β denote the spatial coordinates.

¹⁰<https://github.com/abelcarreras/phonolammps>, accessed 2023-12-04.

4. Summary of Papers

We are going to summarize and discuss the FRFPMS method in this chapter. The overarching story line of the papers included in this thesis is as follows: in paper I we introduce the FRFPMS method and report our first atomic-scale vibrational EELS simulations. Paper II deals with simulations of momentum-resolved vibrational EELS, and some technical details and aspects to consider regarding the practical implementation of the method. Furthermore we motivate reasons for choosing the *hotspot* over the δ -thermostat. In paper III, we report angle- and spatially-resolved FRFPMS simulations for a model system containing a planar defect. After these three papers focused more on computational aspects, we change our angle of investigation in paper IV and compare the elastic and inelastic signals in the FRFPMS method analytically with the QEP model and the first-order Born approximation for a target modeled as a simple harmonic oscillator. This comparison enables us to *revise* the FRFPMS method. We then apply such *revised* FRFPMS method in papers V and VI in calculations of two systems, which we compare directly to experiments performed by collaborators. We observe excellent agreement with experimental results and our simulations enable insights, which would not have been possible from experiment alone. The following sections are dedicated to a more in-depth summary and reflection of each paper.

4.1 Paper I: Proposal of the FRFPMS Method

In our first paper we outline the idea of the FRFPMS method, without yet naming it the FRFPMS method. As mentioned at in the summary of chapter 2 in sec. 2.7, the FPMS method does not allow for spectroscopy, but considers only the effect of *all* atomic vibrations on the diffraction pattern or image. In paper I we extend the FPMS method and add energy resolution to the method by choosing an equidistant grid of N_{bin} frequencies ω_i , $i = 1, \dots, N_{\text{bin}}$, in the range of frequencies for which the PDOS of the specimen is appreciable. For each bin, we perform essentially one full FPMS simulation using snapshots $\{\mathbf{R}_n(\omega_i)\}_{n=1}^{N_c}$, which were sampled from a MD simulation, in which a δ -thermostat, c.f. sec. 3.2, was used to predominantly excite vibrational modes in a narrow interval around the bin fre-

quency ω_i . Equation (2.21) is then replaced by

$$\begin{aligned} I_{\text{incoh}}(\mathbf{q}_{\perp}, z, \mathbf{r}_p, \omega_i) &= \frac{1}{N_c} \sum_{n=1}^{N_c} |\phi(\mathbf{q}_{\perp}, z, \mathbf{r}_p, \mathbf{R}_n(\omega_i))|^2 \\ &= \left\langle |\phi(\mathbf{q}_{\perp}, z, \mathbf{r}_p, \mathbf{R}(\omega_i))|^2 \right\rangle_{N_c} \end{aligned} \quad (4.1)$$

and we also compute the average

$$\begin{aligned} I_{\text{coh}}(\mathbf{q}_{\perp}, z, \mathbf{r}_p, \omega_i) &= \left| \frac{1}{N_c} \sum_{n=1}^{N_c} \phi(\mathbf{q}_{\perp}, z, \mathbf{r}_p, \mathbf{R}_n(\omega_i)) \right|^2 \\ &= \left| \langle \phi(\mathbf{q}_{\perp}, z, \mathbf{r}_p, \mathbf{R}(\omega_i)) \rangle_{N_c} \right|^2. \end{aligned} \quad (4.2)$$

Equation (4.1) is the *incoherently* and equation (4.2) the *coherently* averaged intensity. These expressions were inspired by the QEP model, which we have introduced in sec. 2.5, but similar averages were already used by Hall and Hirsch for the estimation of mean-free paths of TDS [83]. It is worth reiterating, that the coherent average is the elastic intensity corresponding to the ZLP within the QEP models [63], but its meaning was less obvious in the context of the FRFPMS method, since every energy bin gives rise to one coherent average.

The vibrational EELS associated with frequency ω_i is then the difference

$$\begin{aligned} I_{\text{vib}}(\mathbf{q}_{\perp}, z, \mathbf{r}_p, \omega_i) &= I_{\text{incoh}}(\mathbf{q}_{\perp}, z, \mathbf{r}_p, \omega_i) - I_{\text{coh}}(\mathbf{q}_{\perp}, z, \mathbf{r}_p, \omega_i) \\ &= \left\langle |\Psi(\mathbf{q}_{\perp}, z, \mathbf{r}_p, \mathbf{R}(\omega_i))|^2 \right\rangle_{N_c} - \left| \langle \Psi(\mathbf{q}_{\perp}, z, \mathbf{r}_p, \mathbf{R}(\omega_i)) \rangle_{N_c} \right|^2. \end{aligned} \quad (4.3)$$

Thus the inelastic vibrational scattering at energy loss ΔE is within the FRFPMS method assumed to be equivalent to the TDS generated by scattering of an elastic wave on the specimen, which vibrates predominantly with frequency $\omega = \Delta E/\hbar$. The energy loss ΔE is not explicitly considered, but it is in some sense encoded in the (frequency-resolved) displacements of the structure snapshots. We will return to this point in the summary of paper IV in sec. 4.4 and visualize in Fig. 4.1, how these displacements translate into an inelastic signal in the diffraction plane. We also compare the inelastic signal in the diffraction plane with the z-projection of the phonon dispersion and all non-trivial intensity features can be correlated to the phonon dispersion. This demonstrates, that the FRFPMS method is capable of simulating features of vibrational EELS.

We consider hBN as a model material in paper I due to its popularity in vibrational EELS measurements and also because we wanted to compare our results to the results of Ref. [60]. As mentioned above, we used initially a δ -thermostat for frequency-dependent structure snapshot generation. The beam exit wave functions were simulated using an in-house

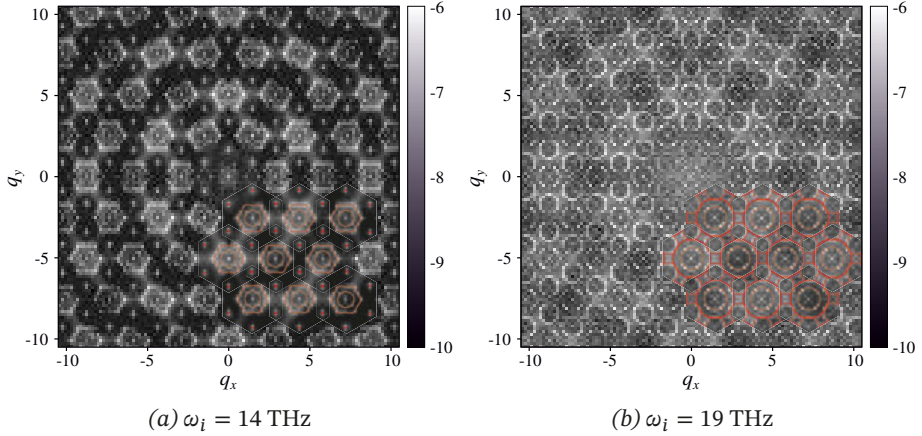


Figure 4.1. Comparison of the z-projection of the phonon dispersion of hBN (thin orange to red lines) with the inelastic signal calculated with the FRFPMS method for two different frequencies ω_i of the δ -thermostat.

implementation of the RSMS method. We consider pure impact scattering in a large detector on-axis and off-axis geometry, which are called Bright Field (BF) and dark field Dark Field (DF) in the paper, respectively. For both geometries, we show spectra and spectrum images.

We observe good agreement of the predicted contrast in both on-axis and off-axis spectrum images with atomic scale maps of phonon losses published in Ref. [60]. Also, off-axis spectrum imaging using only lower energy losses or higher energy losses exhibits atomic scale contrast, in agreement with results in the supplementary material to Ref. [60]. We observe contrast at the positions of atomic columns in on-axis images in good agreement with Ref. [63], where the contrast reversal is explained in terms of the channeling of the electron probe. Furthermore the on-axis spectra and spectrum images turn out to be difficult to converge, since the coherent intensity in the diffraction plane is a considerable fraction of the incoherent intensity for larger convergence angles, and the brightness streaks, which are visible in our on-axis spectrum images serve as a reminder of this circumstance.

Based on these results, we conclude, that the FRFPMS method leads to spectrum images, which are in good agreement with experimental results and simulations of atomic resolution impact scattering phonon EELS. We note, however, that our method calls for deeper theoretical investigations regarding the approximations, which are necessary to derive the FRFPMS method from first principles or from other established theories. Furthermore we note that the FRFPMS method can only be correct for single inelastic scattering, since we would associate an incorrect energy-loss to multiple inelastic processes. We know, however, that some multiple inelastic processes must inherently be captured by our model, since the FPMS

method includes such processes and we are still doing FPMS, just on a subset of all possible modes.

Paper I is overall rather short due to the page limit imposed by the journal, which calls for a follow-up work, in which more details of the method are explored and explained. This is the main purpose of paper II, which is summarized in the following section.

4.2 Paper II: Details about the FRFPMS Method and Momentum-Resolved Simulations

In paper II we give a detailed account of the FRFPMS method, explore the influence of the thermostat on the VPS of the MD simulation, and consider results for momentum-resolved vibrational EELS. Additionally, we compare a high-angle off-axis spectrum for a large collection angle with the total VPS and the in-plane VPS.

The material of choice is thereby again hBN, but the shape of the simulation box is different than in paper I, since we could make use of the same MD trajectories as for the defect-free system calculated for paper III in an effort to save computational resources. We furthermore continue to neglect dipolar scattering and we use the CMS method with the projection approximation according to eq. (3.19) as implemented in `DrProbe` [181]. In this way, we reduce the much fewer computational resources than our in-house implementation based on the RSMS method (c.f. sec. 3.1 for more details on these methods and why the CMS method is faster).

We show in paper II, that the δ -thermostat can lead to difficult to interpret spectra due to finite size effects, if only a sparse grid of such thermostats is used. The reason for this circumstance is the smoothing effect, which thermostats have on the VPS of a MD simulation, and the δ thermostat provides very little of such smoothing of the VPS. There are three thinkable solutions to this problem: we could use a much denser grid of δ -thermostats, a much larger simulation box or a different thermostat, which has a larger frequency-width and provides thus larger smoothing. The first solution is computationally expensive, since the total computational effort increases linearly with the number of thermostats. The same holds even more so for the second solution, since computational effort scales with the volume of the simulation box. This leaves the third solution, which has the potential to not increase computational costs compared with a δ -thermostat simulation, if the same number of trajectories is required. Therefore we adopt the third strategy and use a hotspot thermostat in the MD simulations for paper II. This thermostat has a much wider frequency profile and smooths the VPS sufficiently. All further results in this paper are calculated with the hotspot thermostat.

Layered van der Waals materials, such as hBN, exhibit a strong anisotropy of the PDOS between in-plane and out-of-plane directions, which can be discerned in Fig. 1 of paper II. Furthermore one can consider $\omega_{\mathbf{k}_0\nu}$ as a function of \mathbf{k}_0 along different paths in the Brillouin zone, which leads to characteristic plots of the phonon dispersion. One such plot is depicted in above-mentioned Fig. 1 of paper II for a selection of high symmetry directions.

We proceed by exploring the vibrational EELS predicted by the FRFPMS method. In Figure 4 of paper II we consider the EEL spectrum for a large off-axis detector. We have mentioned in sec. 2.2, that it is expected, that such spectra mimic the projected PDOS, here the in-plane PDOS or VPS. The FRFPMS EEL spectrum decreases rapidly as a function of energy, so we multiply the spectrum by energy in order to reveal more of the spectral features and compare it to the total VPS as well as the in-plane projected VPS. The energy multiplied FRFPMS spectrum exhibits all features observed in the in-plane VPS and incidentally, multiplying the raw spectrum by the square of the energy results in a shape very close to the in-plane VPS. At the time of writing of paper II, this observation confused us a little, since the DDSCS in first-order Born approximation in eq. 2.6 does not have the same energy-scaling at first sight, but we will see in the summary of paper IV, that one can find a simple explanation for the observed scaling.

Furthermore, we considered momentum-resolved vibrational EELS in Figs. 5-7 of paper II. All spectra exhibit a dependence on the momentum transfer \mathbf{q} and phonon polarization ϵ , which is consistent with a dependence of the spectra on the scalar product $\mathbf{q} \cdot \epsilon$. Our results are in this point consistent with single inelastic scattering theory in the first Born approximation (c.f. eq. (2.6)). A careful comparison of the spectra in Figs. 5 and 6 reveals, however, thickness variations in the relative weighing of modes, which cannot be explained within the first Born approximation, but could be caused by dynamical diffraction effects.

In Fig. 7 of paper II we compare the FRFPMS vibrational EELS along two symmetrically distinct paths in the diffraction plane with the phonon dispersion along the corresponding paths in reciprocal space. The agreement between the dispersion and the inelastic intensity of the FRFPMS calculation is very good and the visibility of modes agrees for the most part with the results of Refs. [74, 92]. There are some subtle details, however, in which the simulations differ: hBN is a polar material and the optical modes can cause strong dipolar scattering as $q \rightarrow 0$. In Fig. 7 the vibrational EELS vanishes for optical modes as $q \rightarrow 0$, which is a consequence of our neglect of dipolar scattering and it is not observed when dipolar scattering is included as in Refs. [74, 92]. This interpretation is further supported by the comparison with the results for graphene in Ref. [74]. Graphene is not polarizable and does not give rise to dipolar scattering from optical modes as $q \rightarrow 0$. Dipolar scattering could be included in our FRFPMS calcula-

tions via ionic electron scattering factors as in Refs. [63, 92] and in paper V discussed below.

The longitudinal modes deserve some extra attention at small scattering angles. The DFPT treatment in Ref. [74] predicts for hBN a vanishing cross section for longitudinal modes as $q \rightarrow 0$ for both directions in reciprocal space, i.e., Γ -K as well as Γ -M, which is neither observed in the results for graphene of the same reference, nor in Fig. 7 of paper II, nor in Ref. [92]. It remains to be seen how these predictions can be harmonized.

We additionally observe strong intensity at all Γ -points in Fig. 7 of paper II, which is not observed in Refs. [74, 92]. The spectra exhibit a strong inverse energy-scaling and complicating matters further, statistical effects in our simulation could play a large role at Γ points, since convergence of the vibrational signal is difficult to achieve due to the vibrational intensity being the difference of two almost equally large numbers. Additionally the frequency profile of the hotspot thermostat exhibits non-zero tails at very low frequencies, which could cause motion in small or zero wave vector acoustic modes, which is enhanced by the strong $1/\omega^2$ -scaling of spectra. We will see in the discussion of paper VI, that this issue is indeed connected to our use of frequency-resolved thermostats, since a different snapshot sampling strategy removes this artefact at Γ -points.

These results demonstrate the capabilities of the FRFPMS method to capture details of the phonon scattering process in vibrational EELS as a function of momentum-transfer and energy-loss. In the following section, we consider momentum- and spatially-resolved FRFPMS simulations for a defect system.

4.3 Paper III: Defect Calculation with Nano- and Atomic-Size Beams

In paper III, we consider a system with a planar defect and model spatially-resolved vibrational spectroscopy using either a nanobeam or an atomic-sized beam of convergence semiangles 3 mrad and 25 mrad, respectively. The structure we consider for these simulations is hBN and contains two so-called Anti-Phase Boundaries (APBs). Fig. 1 of the paper displays the structure. In order to conserve computational resources, we use here a hotspot thermostat of width 2.5 THz.

We consider first the changes in the LPDOS induced by the defect in Figs. 2 and 3. The defect is found to induce significant changes in the LPDOS at different frequencies, which are localized to a varying degree near the APB. These changes can be detected in the simulated vibrational EELS for a nanobeam, depicted in Figs. 5-8. The localization of the spectral modifications is thereby probed at nanometer resolution by scanning the nanobeam along a line over the structure and plotting the signal integrated

over a small energy range as a function of beam position. It is interesting to note that spectral modifications are enhanced, if a small detector is placed at specific high-symmetry points, here the K- or M-point, corroborating similar findings in Ref. [66].

Using an atomic-sized beam, the FRFPMS simulations predict that the location of the APB can be pinpointed with atomic-column precision in an off-axis geometry for an appropriate normalization of the spectra, depicted in Figs. 11 and 12. These findings agree with experimental evidence of spatial modifications of vibrational EELS near defects [64, 66]. Furthermore it is worth pointing out, that the APB should be invisible to HAADF imaging, since it is generally thought, that the HAADF intensity is purely a function of atomic column composition. As displayed in Fig. 1 of paper III the atomic columns involved in the APB have all the same composition. We have explained above that the APB is not invisible to vibrational EELS, but we also observe small intensity variations in the HAADF signal as the beam is scanned over the APB, suggesting that some of the modifications of the phonon scattering impact also the HAADF signal. This observation could have implications for atomic counting techniques, which rely on the HAADF image being purely determined by the atomic composition [182].

Overall paper III highlights the capabilities of the FRFPMS method to simulate spatially resolved vibrational EELS for an extended structure containing a defect. Paper III marks also the end of our preliminary computational investigations with the FRFPMS method as we will turn towards more theoretical considerations in the summary of paper IV.

4.4 Paper IV: Lessons from the harmonic oscillator

The idea of paper IV is to consider a simple situation and compare the vibrational EELS predicted by the first-order Born approximation and by the QEP model to the FRFPMS method. We radically simplify our considerations by assuming that the target is a single atom, which is modeled as a 2 dimensional Anisotropic Quantum Harmonic Oscillator (AQHO) with Hamiltonian

$$\hat{H}|\mathbf{n}\rangle = \underbrace{\left[\hbar\omega_x \left(\frac{1}{2} + n_x \right) + \hbar\omega_y \left(\frac{1}{2} + n_y \right) \right]}_{=E_{\mathbf{n}}} |\mathbf{n}\rangle, \quad (4.4)$$

where $|\mathbf{n}\rangle = |n_x, n_y\rangle$ and $\omega_x \neq \omega_y$. We have chosen to work in the language of the DDSCS in order to compare with the formulation of scattering in the first-order Born approximation.

We are then interested in the inelastic DDSCS associated with a transition $n_x \rightarrow n_x + 1$, i.e., single inelastic scattering on the x-mode of the AQHO. We show that the inelastic DDSCS reads in first-order Born ap-

proximation

$$\frac{d^2\sigma}{d\Omega_{\mathbf{q}_\perp} d\omega} = \frac{2\pi^2\hbar}{M} \frac{1 + \langle n_x \rangle_T}{\omega_x} \times \quad (4.5)$$

$$\times q_x^2 f_e^2(q_\perp) e^{-2W_x(q_x)} e^{-2W_y(q_y)} \delta(\omega - \omega_x),$$

where $\langle n_x \rangle_T$ is the phonon occupation number in thermal equilibrium and M is the mass of the target atom. The exponential terms $e^{-2W_x(q_x)}$ and $e^{-2W_y(q_y)}$ are DWFs associated with the x - and y -motion, respectively.

The QEP model and FRFPMS method work with scattered wave functions instead of the DDSCS. In order to be comparable with the Born approximation, we used the WPOA for the scattered wave functions, which is described in sec. 2.3. Using eq. (2.20), we can formulate the DDSCS using the WPOA scattered wave. The QEP model leads to the same inelastic DDSCS as the first-order Born approximation under relevant conditions (small \mathbf{q}_\perp , low temperature T , high frequency ω_x).

The DDSCS predicted by the FRFPMS method and the scattered waves in WPOA reads¹

$$\frac{d^2\sigma}{d\Omega_{\mathbf{q}_\perp} d\omega} = \frac{2\pi^2\hbar}{M} \frac{2\langle n_x \rangle_T + 1}{\omega_x} q_x^2 f_e^2(q_\perp) \delta(\omega - \omega_x) \quad (4.6)$$

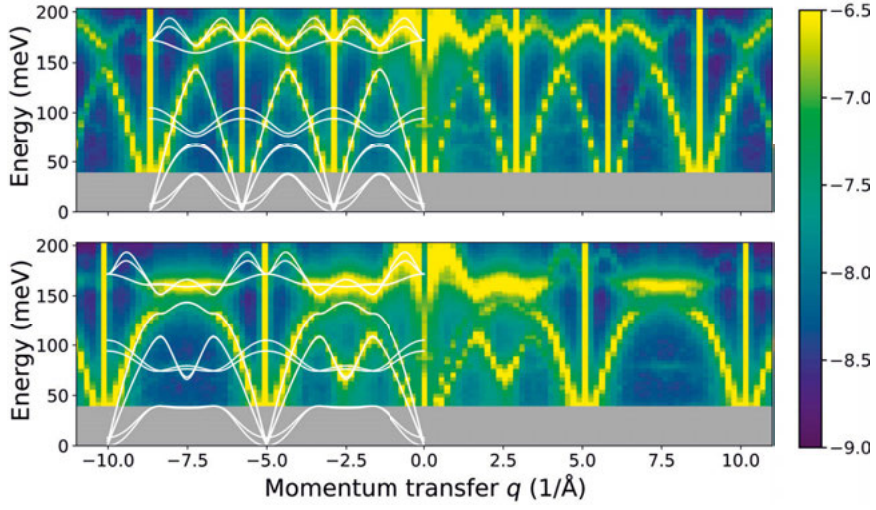
$$= 4\pi^2 q_x^2 \langle u_x^2 \rangle_T f_e^2(q_\perp) \delta(\omega - \omega_x),$$

where $\langle u_x^2 \rangle_T = (2\langle n_x \rangle_T + 1) \hbar / (2M\omega_x)$ is the so-called MSD of the x -mode of the AQHO (c.f. eq. (3.49)).

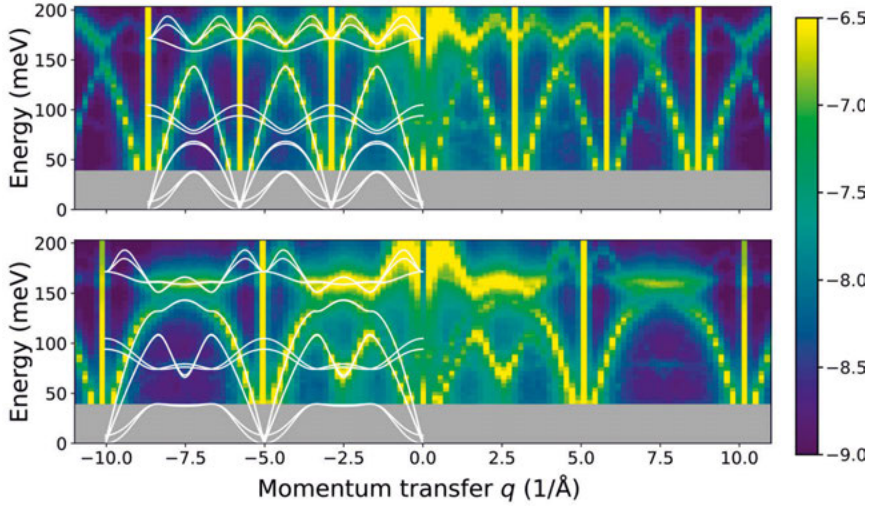
Comparing eqs. (4.5) and (4.6), we recognize that both expressions have a similar dependence on $q_x^2 f_e^2(q)$, but differ in two aspects: their frequency- and temperature-dependent scaling and the appearance of DWF factors. In first-order Born approximation, the single-phonon DDSCS scales with $\langle n_x \rangle_T + 1$, while the FRFPMS expression scales with the MSD, i.e., $2\langle n_x \rangle_T + 1$. We explain this difference as an inherent addition of energy-loss and -gain in the FRFPMS method (c.f. eq. (2.6)). We propose that these differences can be remedied by a straight-forward energy- and temperature-dependent rescaling of the vibrational EELS as computed by the FRFPMS method. Furthermore the momentum-transfer dependence can be corrected for large angles by including an explicit DWF factor in the calculation.

We proceed in the simulations part of paper IV to show that the FRFPMS method *revised* in such way matches the elastic and inelastic DDSCS in first-order Born approximation for a *small enough* mode MSD $\langle u_x^2 \rangle_T$. The requirement of a *reduced* MSD is actually fulfilled in real-world FRFPMS simulations by virtue of the frequency-selectivity, since only a subset of all possible modes contribute in any given bin. The AQHO is in comparison

¹We neglect here the relativistic factor γ appearing in the paper.



(a) No DWF included



(b) DWF included

Figure 4.2. Comparison of the inelastic signal along Γ -M- Γ (top panels) and Γ -K-M-K- Γ directions in hBN for (a) the *original* FRFPMS and (b) the *revised* FRFPMS method. The color scale corresponds to the decadic logarithm of the inelastic intensity.

a rather artificial model system, since all motion along x would contribute to the same frequency-bin in the FRFPMS method.

Another interesting outcome of this paper is, that we can actually explain the frequency-scaling of large detector off-axis spectra, which we have observed in connection with paper II. Contrary to what we have written in eq. (4.6), our MD simulations do not generate quantum dynamics, but atoms follow classical equations of motion. Thus thermodynamic averages sampled by MD simulations satisfy by default classical statistical mechanics. We show in appendix I, that the classical MSD of a 2D harmonic oscillators reads

$$\langle u_x^2 \rangle_T = \frac{k_B T}{M \omega_x^2}, \quad (4.7)$$

i.e., the classical MSD of a harmonic oscillator scales as $1/\omega^2$. Together with the last line of eq. (4.6), we can explain the $1/\omega^2$ -scaling observed in paper II with the classical statistics of displacements in our simulations.

The calculations in paper II show that by selecting only certain modes to contribute to displacements of atoms, one can indeed account for the inelastic scattering generated by those modes in a single inelastic scattering picture. Certain corrections regarding the scaling with frequency, temperature as well as large momentum-transfer should be applied, but these are expected to predominantly affect the “quantitativeness” of the inelastic scattering. Qualitatively the *original* FRFPMS method gives similar result as we showcase in Fig. 4.2. The main difference in terms of momentum-transfer dependence between the calculations is found at large momentum transfers, where the *revised* FRFPMS method shows less intensity compared with the *original* FRFPMS method. Overall we have made an important step forward in understanding the FRFPMS method and its inherent approximations in paper IV.

4.5 Paper V: Isotope Effects in Momentum-Resolved Vibrational EELS

Paper V focuses on the isotopic shift of optical phonon frequencies in hBN as the isotopic mass of boron is changed from ^{10}B to ^{11}B . We compare the simulated vibrational EELS to experiments performed by Jordan Hachtel from Oak Ridge National Laboratory (TN, USA). Apart from the scaling corrections outlined in sec. 4.4, we have made a number of additional improvements to our calculations in order to account better for momentum-resolved vibrational EELS on hBN.

The most notable improvement is showcased in Fig. 4.2, where we obtain an inelastic signal for optical modes near $\mathbf{q}_\perp = 0$, which was not observed in the calculations for paper II. Here we use *ionic* electron scattering

factors, which account better for dipolar scattering near $\mathbf{q}_\perp = 0$. We also note that all three optical modes have the same frequency at Γ -points, even though LO- and TO-modes should be split in a polar material such as hBN. This is a consequence of periodic boundary conditions and a finite supercell, which is used in the MD simulations. Actually also DFT and DFPT phonon calculations do not include this splitting by default either, but it is added “by hand” using a so-called *non-analytic term correction* to the dynamical matrix [183]. Since we use the trajectories generated by MD simulations directly in the FRFPMS method, such correction cannot be applied and the FRFPMS does not include LO/TO splitting.

Another improvement regards the IAP in the MD simulations. We use a machine-learned so-called GAP potential [184]. This potential is trained on DFT calculations and allows therefore for near-DFT accuracy of interatomic forces at much lower computational cost. The improved accuracy is visible in the vibrational frequencies of optical modes, which are about 4 THz lower than in our simulations for paper II as a comparison of relevant Figs. 1 and 2 of paper V with Figs. 1 and 7 of paper II reveals. The GAP potential is, however, still much more computationally demanding than the empirical force fields used in papers II and III, and the computations for paper V have been among the most demanding of the whole dissertation.

We show in Figs. 2 and 3 of paper V, how the computed and experimentally measured momentum-resolved vibrational EELS changes as a function of the ratio of ^{10}B to ^{11}B . The main change is thereby a softening of the optical modes by about 7 meV when going from hBN with ^{10}B to ^{11}B as depicted in Fig. 1 of paper V. This is in qualitative agreement with expectations based on the dispersion of a linear chain of masses m_1 and m_2 connected by harmonic springs [93]

$$\omega_{\pm}^2(k) = K \left(\frac{1}{m_1} + \frac{1}{m_2} \right) \pm K \sqrt{\left(\frac{1}{m_1} + \frac{1}{m_2} \right)^2 - \frac{4 \sin^2 \frac{ka}{2}}{m_1 m_2}}, \quad (4.8)$$

where K is the spring constant, k the wave vector, and a the lattice parameter. At the Brillouin zone boundary $k = \pi/a$ and if we assume without loss of generality $m_1 > m_2$, we find

$$\Delta\omega = \omega_+(k = \pi/a) - \omega_-(k = \pi/a) = \sqrt{\frac{2K}{m_1 m_2}} (\sqrt{m_1} - \sqrt{m_2}). \quad (4.9)$$

In this simple model, the “gap” $\Delta\omega$ between the acoustic and the optical branch is a function of the difference of the square roots of masses between the two basis atoms. Since Nitrogen has atomic mass of 14, the difference in mass to ^{11}B is smaller than to ^{10}B and a smaller “gap” is thus expected. In summary, we have demonstrated that momentum-resolved vibrational

EELS can be used to detect the small isotopic shift in phonon frequencies in a momentum-resolved way.

4.6 Paper VI: Imaging Vibrational Anisotropy

The last paper included in this dissertation is another collaboration with experimental colleagues, predominantly Xingxu Yan from University of California in Irvine (CA, USA). Xingxu approached us with the question to simulate atomic-resolution vibrational STEM-EELS for Strontium Titanate (STO). He had done some measurements, which showed that it is possible to do elemental mapping using vibrational EELS in a large detector off-axis geometry. Initially we resorted to simulations using an empirical IAP [185], which we had used in an old project published in Ref. [122], but changed quickly to a machine-learned, so-called DeePMD IAP [186, 187]. This IAP provided a much better description of the phonon dispersion, which was deemed crucial for this project.

The DeePMD IAP is able to describe the structural phase transition from the low temperature tetragonal to the high temperature cubic phase in STO. At room temperature, STO is in the cubic phase. This advanced potential brought some issues for the FRFPMS method as we have applied it thus far. We have used frequency-dependent thermostats thus far and these thermostats do not work well for phase transitions driven by temperature, since they enforce a non-equilibrium situation, in which not all modes are thermalized, but only a subset of modes is maintained at a kinetic energy corresponding to the desired temperature. Therefore the structural phase transition would not happen in these non-equilibrium simulations, which would consequently lead to inaccurate vibrational EELS within the FRFPMS method.

In order to circumvent this issue and to improve the FRFPMS method further, we have implemented a new snapshot sampling strategy for paper VI. The starting point for the idea was learning about the relation between the VPS and the PDOS introduced in secs. 3.2 and 3.3. Inspired by the procedure of the FT of the velocity trajectory, we came up with the idea that one could obtain trajectories, in which arbitrary ranges of frequencies contribute, by band-pass filtering the position trajectory. We can then sample snapshots for FRFPMS calculations from these band-pass filtered trajectories. We compare this method compares to simulations with a hotspot thermostat in Fig. 4.3. The band-pass method faithfully reproduces features of the phonon dispersion, similar to the hotspot thermostat. However, we observe much lower background between the bands in comparison with the hotspot thermostat, suggesting that band-pass filtering leads to a cleaner frequency-selectivity. Furthermore the strong artefacts at Γ -points are removed by the band-pass filtering method. We attribute the

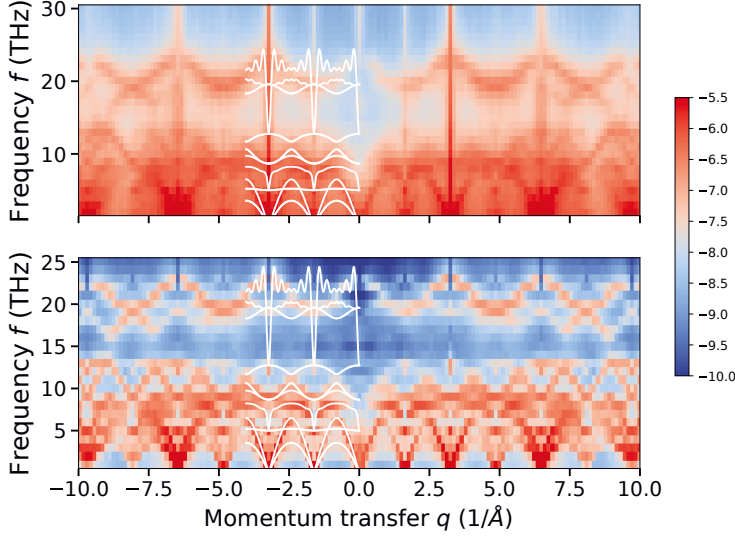


Figure 4.3. Comparison of simulated vibrational EELS along the Γ -X- Γ direction in STO for snapshots sampled with a hotspot thermostat (top panel) and using the band-pass filtering method developed in connection with paper VI (bottom panel). These results were obtained using the IAP of Ref. [185]. We have overlaid the phonon dispersion calculated without applying the non-analytic term correction. The decadic logarithm of the inelastic intensity is represented by the color map.

removal of these artefacts to the better frequency-selectivity, which does not lead to low-frequency tails, which might be the cause of the artefacts in the case of the hotspot thermostat simulations.

After these preliminary considerations of computational advances in the calculations of vibrational EELS with the FRFPMS method, we turn our attention now to a brief discussion of the main results of paper VI. Our collaborators have measured vibrational EELS in a large detector off-axis geometry with careful consideration of the displacement direction of the detector with respect to the sample. We show in Fig. 2 of paper VI that it is possible to map the location of Strontium (Sr), Titanium (Ti), and Oxygen (O) atoms in STO at the atomic scale via spectrum imaging using appropriate energy-loss windows. Our simulated maps are in excellent agreement with the experimental maps of the vibrational EELS. Furthermore and even more interestingly, the visibility of O columns depends on the displacement direction of the detector with respect to the sample. Maps of the vibrational energies ≤ 60 meV, predominantly associated with O vibrations, show a signal at only one of the two O columns for a detector aligned with the $[100]$ direction in STO. Shifting the detector, such that it is displaced by the same angle with respect to the direct beam along the $[010]$ direction, the other O column of STO is visible, while we observe less intensity at the previous O column.

Analyzing this directional selectivity in more detail in Fig. 3, we find that the reason for it is the anisotropic motion of O atoms in STO, which is characterized by a so-called *thermal ellipsoids*. This anisotropy is long known and has recently also been studied using core-loss EELS [188]. However, we are able to image the evolution of the thermal ellipsoids as a function of vibrational frequency for the first time. At low frequencies, the thermal ellipsoids of O atoms are extended along the plane with Sr atoms, while they are extended along the direction of bonds with the closest Ti atoms at high frequencies. We find then that the vibrational EELS is enhanced, if the detector is displaced parallel to the direction of one of the major axes of the frequency-dependent thermal ellipsoid. In Fig. 2 this dependence is mainly visible in the directionality of the “haze” around the intense Ti columns at low energy-loss, but at high energies it leads to the visibility of only one of the two pure O columns. Overall our simulations are in excellent agreement with experimentally obtained data, demonstrating the predictive and interpretative power of the FRFPMS method.

Within the DDSCS in first-order Born approximation, we can rationalize the origin of the observed directional selectivity. According to Eq. 2.6, the inelastic DDSCS depends on the square of the scalar product $\mathbf{q}_\perp \cdot \boldsymbol{\epsilon}_{\perp \mathbf{q}_0 \nu}$ and we have seen that the momentum transfer \mathbf{q}_\perp in the diffraction plane can be uniquely decomposed into a lattice vector \mathbf{G}_\perp and a vector $\mathbf{q}_{0\perp}$ in the first Brillouin zone, i.e.,

$$\mathbf{q}_\perp = \mathbf{G}_\perp + \mathbf{q}_{0\perp}. \quad (4.10)$$

In our geometry, the momentum transfer in the diffraction plane \mathbf{q}_\perp is relatively large, since we have displaced the center of the EEL spectrometer entrance aperture by about five primitive reciprocal lattice vectors \mathbf{b}_1 or \mathbf{b}_2 along the [100] or [010] directions, respectively. Neglecting that the detector covers more than one Brillouin-zone and aligning \mathbf{b}_1 with the x - and \mathbf{b}_2 with the y -axis, we can write the scalar product as

$$\mathbf{q}_\perp \cdot \boldsymbol{\epsilon}_{\perp \mathbf{q}_0 \nu} = \begin{cases} 5 b_1 \epsilon_{x \mathbf{q}_0 \nu} + \mathbf{q}_{0\perp} \cdot \boldsymbol{\epsilon}_{\perp \mathbf{q}_0 \nu} & \text{along [100]} \\ 5 b_2 \epsilon_{y \mathbf{q}_0 \nu} + \mathbf{q}_{0\perp} \cdot \boldsymbol{\epsilon}_{\perp \mathbf{q}_0 \nu} & \text{along [010]}. \end{cases} \quad (4.11)$$

Thus we see, that the scalar product leads to a directional dependence due to the detector displacement, which is given by the larger first term in eq. (4.11). This selectivity is further enhanced by the circumstance, that it is the square of the absolute value of this scalar product, which enters the actual expression of the DDSCS. Thus our results here show, that the large-angle off-axis spectrum is not simply proportional to the in-plane PDOS, but rather to the PDOS projected along the reciprocal lattice vector component \mathbf{G}_\perp of momentum transfer \mathbf{q}_\perp , which is also formulated in the supplementary material of Ref. [64].

This project really showcases the importance of modeling and computation for the interpretation of vibrational EELS measurements. Initially,

the goal of this project was “just” to demonstrate atomic resolution spectrum imaging using vibrational EELS, but thanks to our simulations, we could show that it is possible to extract a lot more information in the form of imaging vibrational anisotropies from large detector off-axis vibrational EELS spectra.

5. Conclusions and Outlook

We have introduced the FRFPMS method in this dissertation and applied it to momentum- and spatially-resolved simulations of vibrational spectroscopy in the STEM. We have shown that simulation results are in good agreement with other published results, both experimental and theoretical. We have demonstrated in paper I, that the FRFPMS approach can be used to simulate spectra as well as spectrum images in vibrational EELS. In paper II, we have applied the method to simulations of momentum-resolved EELS, for which our method correctly predicts the visibility of phonon modes along high-symmetry directions in the diffraction plane. We have also considered simulations of momentum- and spatially-resolved vibrational EELS for an extended planar defect in paper III, for which our method corroborates experimental observation of other studies.

Furthermore our method enabled the interpretation of state-of-the-art experiments in papers V and VI, in which we observe excellent agreement of our simulations with measurements. Specifically in paper VI, our simulations guided the refinement of the experimental conditions until we could confidently demonstrate the ability to image the frequency-dependent vibrational anisotropy of O atoms in STO. We have thereby added in principle the direction and magnitude of the phonon polarization vector to the growing list of properties, which can be investigated using vibrational EELS.

Parallel to these simulation studies, we have also continued to develop the calculation techniques of the FRFPMS method. We switched from the δ -thermostat to the hotspot thermostat and, more recently, to band-pass filtered MD trajectories. With this evolution our understanding of what the essence of the FRFPMS method is has also changed: we assumed initially that frequency-resolved MD simulations were strictly necessary and really at the core of our method. But gradually this view developed further and we have now that the core or essence of the FRFPMS method is to approximate the *single* inelastic scattering of high-energy electrons on a range of vibrational modes by averaging *elastic* multislice calculations over snapshots of the atomic structure, in which only the selected range of vibrational modes contributes to the displacements of atoms. The way these snapshots are generated does not matter in principle¹. We have also

¹Every snapshot generation strategy will, of course, have its benefits and drawbacks as we have shown in this thesis. The point we are trying to make is rather, that the FRFPMS idea works with any snapshot generation technique able to provide frequency resolution.

introduced a *revision* of our original method in paper IV by including the DWF and an energy- and temperature-dependent rescaling of spectra in our procedure. With these modifications dynamical diffraction effects and the quantitateness of single inelastic phonon scattering should be modeled much more accurately as a function of momentum transfer and calculated spectra should match experimentally measured spectra better as a function of energy-loss.

Considering these results, we have demonstrated that our method satisfies the need for a method to simulate vibrational EELS including dynamical diffraction effects and capable of dealing with large structures at reasonable computational cost, which we have identified in section 2.

But this dissertation is in the end not the end of the story of the FRFPMS method, but rather a preliminary status report on its state at the end of 2023. There are some areas, where further research and development is necessary. The most obvious one, and one that we are still investigating, is, that we have yet to demonstrate proper inclusion of dynamical diffraction effects. This is a difficult topic, since we do not have many results to compare with. That dynamical diffraction happens in our simulations in some form is clear, since we use multislice calculations and we have observed in paper II variations in the spectral shape as a function of thickness. We believe at the time of writing, that with proper inclusion of the DWF and of an absorptive potential, the *revised* FRFPMS method approximates the effect of dynamical diffraction very well. Once the question of correct dynamical diffraction has been settled, careful investigations of the thickness-dependence of vibrational EELS spectra can be made, which are of great interest for the design and interpretation of experiments and quantitative measurements of vibrational properties.

Another avenue of future research, which is already under way, is to understand the FRFPMS method within a *correlated* model of atomic motion beyond the AQHO. Furthermore, it will also be instructive to consider the FRFPMS method beyond the single slice and weak projected potential limit investigated in paper IV. Here the formalism and observations of Ref. [114] might provide a suitable starting point. There it was shown that the FPMS method and QEP model are approximating the full Green's function of the beam-sample system by the “static” Green's function of the beam electron for a “snapshot” of the sample. Within the FRFPMS method, we are very likely doing the same approximation, but the exact details remain to be seen.

6. Popular Science Summary

The topic of this dissertation is the development of a computational method for the simulation of vibrational Electron Energy Loss Spectroscopy (EELS) in the Scanning Transmission Electron Microscope (STEM). The purpose of this chapter is to enable an understanding of the context and main results of this work for a general audience.

Scientific progress often relies on the development of new imaging techniques, which allow us to *see the previously unseen*: the history of electron microscopy is deeply intertwined with scientists *seeing* more and more of the microscopic world. Today we are able to routinely see atoms in the STEM. The image is thereby assembled in a pixel-by-pixel fashion by *scanning* an electron beam over the sample. At each beam position, the number of electrons which have reached a detector is recorded and the final image is a map of these numbers.

The origin of these images are interactions of the beam electrons with the sample. Interactions can either change the direction of travel, or the speed (energy) of the beam electrons. Those interactions that change the direction of travel are called *elastic*, while those that instead change the speed are called *inelastic*. Conventional STEM images look at the more likely elastic interactions and are captured by placing an electron detector behind the sample. The detector captures all electrons, which move in a certain direction after interaction with the sample.

One can, however, extract more information about the sample by combining the STEM with a so-called Electron Energy Loss (EEL) spectrometer. The EEL spectrometer is essentially a “speed-cam” for electrons, which is placed behind the sample in the direction of the beam. The combination of the STEM technique with EELS, enables us to study variations in the speed of electrons after interaction with the sample as the beam is scanned over the sample. We can extract very useful information with this technique such as the elemental composition of the sample and information about atomic bonding.

In materials, vibrations are intimately connected with thermal properties and temperature. Almost ten years ago the EELS technique received a major upgrade. Using an improved so-called *monochromator* the energy resolution was massively improved, meaning that it is now possible to measure smaller differences in the speed of electrons. Similar to how the electron microscope opened the door to the nano-world, the monochromator opened the gate to the world of nano-scale measurements of vibrational

properties in the STEM. Vibrational EELS has therefore great potential for advancing our understanding of the flow of heat at the nano- and atomic-scale, which could help to better manage heat in microchips, to invent new heating or refrigeration techniques, and design materials for energy applications.

The interaction of the beam electrons with the sample is rather complicated in a STEM. The electrons interact often not only once, but several times with the sample, especially for thicker samples. This possibility of multiple interaction makes experiments difficult to interpret and often validation of the results with a computational model of the beam-sample interaction is required. This dissertation presents a new way of modeling that complicated interaction between the sample and the beam electrons.

In a series of papers, we have introduced a new model of vibrational EELS called FRFPMS. Apart from modeling the inelastic interaction, our model allows to take multiple elastic interactions with the sample into account. It is also computationally tractable and works for systems, which require large computations such as samples containing defects and interfaces.

The name of our model, the *Frequency-Resolved Frozen Phonon Multislice* (FRFPMS) method, is a rather unforgiving name to the uninitiated, so we will briefly unravel it here. A so-called *multislice* calculation is, simply said, a calculation of the probability of the beam electron to move in a certain direction after elastic interaction with a sample. The outcome of the calculation depends predominantly on the position of the atoms. The *Frozen Phonon Multislice* (FPMS) method, which is a standard method for calculating the effect of thermal vibrations on STEM images, uses many multislice calculations for different thermal displacements of atomic positions. The average over such calculations allows to extract the probability of inelastic interaction of the beam electrons with vibrational excitations of the sample in the *whole* range of vibrational energies. Our model extends the FPMS with *frequency-resolution*.

We take a moment to unravel this concept: the conventional models of atomic motion used in connection with the FPMS method take the whole range of possible vibrations into account. However, for the purpose of vibrational EELS, we want to know how many electrons have interacted within a certain range of energies. This is where the aforementioned frequency-resolution added with the FRFPMS method comes.

The core idea of the FRFPMS method is then straightforward: in order to model the probability of exchanging a certain amount of energy, we just need to reduce the range of vibrations in the model for the atomic motion. We can then apply the same machinery of multislice calculations and averaging as one does within the FPMS method. By repeating this procedure for every range of frequencies we are interested in, we can assemble the full picture of the probability of exchanging a certain amount of energy with vi-

brations in the sample, thus contributing to an increased understanding of atomic motion and the flow of heat at these small scales.

Paper I introduces this idea. We apply the idea and compare its predictions to other experimental and theoretical results in papers II and III. The main message of these papers is that our model agrees with other research whenever comparable conditions are found, but it offers something extra compared to other models of vibrational EELS in the form of being able to account for multiple elastic scattering and being able to treat systems requiring large models of the atomic positions.

However, despite the success in modeling, we asked ourselves questions about what kind of simplifications the FRFPMS method makes. So we compare the FRFPMS method in paper IV to other established theoretical approaches for a very simple situation. We assume that the beam electrons interact only with a single carbon atom, which is modelled as a so-called Quantum Harmonic Oscillator (QHO), the simplest possible model of how an atom is bound in a crystal. We show that the procedure of the FRFPMS method gives identical results to other theories, provided we apply two small modifications. These modifications regard changes to the scaling of the computed probabilities with exchanged energy and temperature as well as a reduction of the probability of electrons to be deflected under a large angle from their initial direction of travel. We refer to this modified FRFPMS method as the *revised* FRFPMS method.

The last two papers are the result of collaborations with experimental colleagues and we model explicit experiments. In paper V we consider the effect of different isotopic compositions in hBN. Isotopes are atoms of the same element with different mass. As such they share much of the same chemical properties, but the atomic mass influences the vibrational frequencies. In agreement with expectation, experiment and other works on this topic, we find that the highest vibrational energies in hBN are affected by the isotopic composition and shift to lower values for larger isotope mass. We show that it is possible to detect this shift using vibrational EELS depending on the direction of travel of electrons after interaction. In the last paper, paper VI, our calculations enabled us to interpret an interesting effect, which was not anticipated at the start of our collaboration. We observe in both experiment and theory, that maps of the inelastic interaction probability near Oxygen atoms in a material called Strontium Titanate (STO) are sensitive to the direction in which the inelastic electrons travel after the interaction. We explain this sensitivity with the anisotropy of the motion of oxygen atoms in STO, which means simply said, that Oxygen atoms move more along one axis than along another. This anisotropy is long known, but we could image it here for the first time as a function of vibrational frequency and show that the direction of atomic motion of Oxygen changes from low to high vibrational frequencies.

In summary, we contribute with this thesis an efficient and versatile computational model for the simulation and interpretation of vibrational EELS, which is an important tool for the study of heat at the nano- and atomic-scale with many potential applications in areas of materials science and nano-engineering.

7. Populärvetenskaplig Sammanfattning

Ämnet för denna avhandling är utvecklingen av en beräkningsmetod för simulering av vibrationell Elektronenergiförlustspektroskopi (EELS) i Rasteröverföringselektronmikroskopet (STEM). Syftet med detta kapitel är att ge en förståelse för sammanhanget och de huvudsakliga resultaten av detta arbete för en bredare publik.

Vetenskapens framsteg förlitar sig ofta på utvecklingen av nya avbildningstekniker, vilka möjliggör att vi kan *se det tidigare osedda*. Historien om elektronmikroskopi är djupt förknippad med forskare som *ser* allt mer av den mikroskopiska världen. Idag kan vi rutinemässigt se atomer i STEM. Bilden sätts samman pixel för pixel genom att *skanna* en elektronstråle över provet. Vid varje strållägesposition registreras antalet elektroner som har nått en detektor, och den slutliga bilden är en karta över dessa nummer.

Ursprunget till dessa bilder är interaktioner mellan strålelektronerna och provet. Interaktioner kan antingen ändra riktningen eller hastigheten (energin) hos strålelektronerna. De interaktioner som ändrar riktningen kallas *elastiska*, medan de som istället ändrar hastigheten kallas *inelastiska*. Konventionella STEM-bilder fokuserar på de mer sannolika elastiska interaktionerna och tas genom att placera en elektrondetektor bakom provet. Detektorn fångar alla elektroner som rör sig i en viss riktning efter att ha interagerat med provet.

Man kan dock extrahera mer information om provet genom att kombinera STEM med en så kallad Electron Energy Loss (EEL)-spektrometer. EEL-spektrometern är i huvudsak en "fartkamera" för elektroner, som placeras bakom provet i riktning mot strålen. Kombinationen av STEM-tekniken med EELS möjliggör studier av variationer i elektronernas hastighet efter interaktion med provet, där strålen skannar över det. Vi kan extrahera mycket användbar information med denna teknik, så som provets grundläggande sammansättning och information om atomära bindningar.

I material är vibrationer intimt kopplade till termiska egenskaper och temperatur. För nästan tio år sedan fick EELS-tekniken en betydande uppgradering. Genom en förbättrad s.k. *monokromator* förbättrades energiuoplösningen kraftigt, vilket innebär att det nu är möjligt att mäta mindre skillnader i elektronernas hastighet. Liknande till hur elektronmikroskopet öppnade dörren till nanovärlden, öppnade monokromatoren porten till mätningar av vibrerande egenskaper på nanoskala i STEM. Vibratorisk EELS har därför stor potential att främja vår förståelse för värmeöverföring

på nano- och atomskala, vilket kan hjälpa till med att bättre hantera värme i mikrochip, uppfinna nya uppvärmnings- eller kylningstekniker och designa material för energiapplikationer.

Interaktionen mellan strålelektronerna och provet är ganska komplicerad i STEM. Elektronerna interagerar ofta inte bara en gång, utan flera gånger med provet, särskilt för tjockare prover. Denna möjlighet till flera interaktioner gör experiment svåra att tolka och ofta krävs validering av resultaten med en beräkningsmodell av stråle-prov-interaktionen. Denna avhandling presenterar ett nytt sätt att modellera denna komplicerade interaktion mellan provet och strålelektronerna.

I en serie av artiklar har vi introducerat en ny modell för vibrationell EELS kallad FRFPMS. Förutom att modellera den inelastiska interaktionen gör vår modell det möjligt att ta hänsyn till flera elastiska interaktioner med provet. Den är också beräkningsmässigt hanterbar och fungerar för system som kräver stora beräkningar, så som prover innehållande defekter och gränsskikt.

Vi kallar vår modell för *Frequency-Resolved Frozen Phonon Multislice* (FRFPMS), ett namn som kan upplevas främmande för oinvidga, så vi kommer kort att förklara det här. En så kallad *multislice*-beräkning är helt enkelt en beräkning av sannolikheten för att strålelektronen rör sig i en viss riktning efter en elastisk interaktion med ett prov. Resultatet av beräkningen beror huvudsakligen på positionen hos atomerna. *Frozen Phonon Multislice* (FPMS)-metoden, som är en standardmetod för att beräkna effekterna av termiska vibrationer på STEM-bilder, använder många multislice-beräkningar för olika termiska förflyttningar av atompositioner. Medelvärdet över dessa beräkningar gör det möjligt att extrahera sannolikheten för inelastiska interaktioner mellan strålelektroner och vibrationella excitationer i hela spektrat av vibrationsenergier. Vår modell utvidgar FPMS med *frekvensupplösning*.

Vi tar en stund för att förklara detta begrepp: de konventionella modellerna för atomrörelse som används i samband med FPMS-metoden tar hänsyn till hela spektrat av möjliga vibrationer. Men för vibrationell EELS vill vi veta hur många elektroner som har interagerat inom ett visst energiområde. Detta är där den tidigare nämnda frekvensupplösningen tillsammans med FRFPMS-metoden kommer in.

Kärnidéen med FRFPMS-metoden är då rättfram: för att modellera sannolikheten att utbyta en viss mängd energi behöver vi bara minska vibrationsområdet i modellen för atomrörelsen. Sedan kan vi tillämpa samma metod med multislice-beräkningar och medelvärdesberäkning som inom FPMS-metoden. Genom att upprepa detta förfarande för varje frekvensområde som vi är intresserade av kan vi sammanställa den fullständiga bilden av sannolikheten att utbyta en viss mängd energi med vibrationer i provet, vilket bidrar till en ökad förståelse för atomrörelse och värmetransport på dessa små skala.

Artikel I introducerar denna idé. Vi tillämpar idén och jämför dess förutsägelser med andra experimentella och teoretiska resultat i artikel II och III. Det huvudsakliga budskapet i dessa artiklar är att vår modell överensstämmer med annan forskning när jämförbara förhållanden finns, men den erbjuder något extra jämfört med andra modeller för vibrationell EELS genom att den kan ta hänsyn till flera elastiska spridningar och behandla system som kräver stora modeller för atompositionerna.

Trots framgången i modellering ställde vi oss frågor om vilka förenklingar FRFPMS-metoden gör. Vi jämför FRFPMS-metoden i artikel IV med andra etablerade teoretiska metoder för en mycket avskalad situation. Vi antar att strålelektronerna bara interagerar med en enda kolatom, som modelleras som en s.k. Quantum Harmonic Oscillator (QHO), den enklast möjliga modellen för hur en atom är bunden i en kristall. Vi visar att vår metod ger identiska resultat som andra teorier, förutsatt att vi applicerar två små modifieringar. Dessa gäller förändringar av skalningen hos beräknade sannolikheter med utbytt energi och temperatur, samt en minskning av sannolikheten att elektroner avviker i en stor vinkel från deras ursprungliga färdriktning. Vi hänvisar till denna modifierade FRFPMS-metod som *reviderad* FRFPMS-metod.

De två sista artiklarna är resultatet av samarbeten med kollegor inom det experimentella fältet och vi modellerar väldefinierade experiment. I artikel V överväger vi effekten av olika isotopsammansättningar i hBN. Isotoper är atomer av samma element men med olika massa. Även om de delar många kemiska egenskaper så påverkar den atomära massan de vibrationella frekvenserna. I överensstämmelse med förväntningar, experiment och andra arbeten inom detta ämne finner vi att de högsta vibrationsenergierna i hBN påverkas av isotopsammansättningen och förskjuts till lägre värden för större isotopmassa. Vi visar att det är möjligt att detektera denna förskjutning med hjälp av vibrationell EELS beroende på elektronernas färdriktning efter interaktion. I den sista artikeln, artikel VI, möjliggjorde våra beräkningar tolkningen av en intressant effekt som inte hade förväntat oss i början av vårt samarbete. Vi observerar både i experiment och teori att kartor över sannolikheten för inelastisk interaktion nära syreatomer i ett material kallat Strontium Titanate (STO) är känsliga för riktningen i vilken de inelastiska elektronerna färdas efter interaktionen. Vi förklarar denna känslighet med anisotropin i rörelsen hos syreatomer i STO, vilket helt enkelt betyder att syreatomer rör sig mer längs en specifik axel än längs en annan. Denna anisotropi har länge varit känd, men här kunde vi för första gången avbilda den som en funktion av vibrationsfrekvensen och visa att riktningen för atomrörelsen hos syreatomer ändras från låga till höga vibrationsfrekvenser.

Sammanfattningsvis bidrar vi i och med denna avhandling till en effektiv och mångsidig beräkningsmodell för simulering och tolkning av vibrationell EELS, vilket är ett viktigt verktyg för studier av värme på nano- och

atomskala med många potentiella tillämpningar inom materialvetenskap och nanoingenjörsvetenskap.

8. Populärwissenschaftliche Zusammenfassung

Das Thema dieser Dissertation ist die Entwicklung eines Berechnungsverfahrens zur Simulation von Elektronenenergieverlustspektroskopie (EELS) von Atomschwingungen und Gitterschwingungen im Rastertransmissionselektronenmikroskop (STEM). Das Ziel dieses Kapitels ist es, der Allgemeinheit ein Verständnis für den Kontext und die Hauptergebnisse dieser Arbeit zu ermöglichen.

Wissenschaftlicher Fortschritt baut oft auf der Entwicklung neuer bildgebender Verfahren auf, die es uns ermöglichen, das *zuvor Unsichtbare sichtbar zu machen*: Die Geschichte der Elektronenmikroskopie ist tief damit verbunden, dass wir immer mehr von der mikroskopischen Welt *sehen* können. Heutzutage können wir routinemäßig Atome im STEM sehen. Ein Elektronenstrahl wird dabei über die Probe *gescannt* (gerastert) und das Bild Pixel für Pixel aufgebaut. An jeder Position des Strahls wird die Anzahl der Elektronen, die einen Detektor erreicht haben, aufgezeichnet, und das endgültige Bild ist eine Art "Karte" dieser Zahlen.

Der Ursprung dieser Bilder liegt in den Wechselwirkungen der Strahlelektronen mit der Probe. Wechselwirkungen können entweder die Richtung der Bewegung oder die Energie der Strahlelektronen ändern, was sich in einer Veränderung ihrer Geschwindigkeit äußert. Wechselwirkungen, die die Richtung der Bewegung ändern, werden als *elastisch* bezeichnet, während solche, die stattdessen die Geschwindigkeit ändern, als *inelastisch* bezeichnet werden. Konventionelle STEM-Bilder werden mittels der wahrscheinlicheren elastischen Wechselwirkungen und mit Hilfe eines Elektronendetektors erstellt, der in Strahlrichtung hinter der Probe platziert wird. Der Detektor erfasst dabei alle Elektronen, die sich nach der Wechselwirkung mit der Probe in eine bestimmte Richtung bewegen.

Es ist jedoch möglich, mehr Informationen über die Probe zu gewinnen, indem man das STEM mit einem sogenannten Elektronenenergieverlustspektrometer (EEL-Spektrometer) kombiniert. Das EEL-Spektrometer ist im Wesentlichen ein "Blitzer" für Elektronen, der in Richtung des Elektronenstrahls hinter der Probe platziert ist. Die Kombination der STEM-Technik mit EELS ermöglicht es uns, Unterschiede in der Geschwindigkeit der Elektronen nach der Wechselwirkung mit der Probe zu untersuchen, während der Strahl über die Probe gescannt wird. Wir können mit dieser Technik sehr nützliche Informationen extrahieren, wie etwa die elementare Zusammensetzung der Probe und Informationen über die atomare Bindung.

In atomare Schwingungen sind eng mit den thermischen Eigenschaften und der Temperatur eines Materials verbunden. Vor fast zehn Jahren machte die EELS-Technik einen großen Fortschritt. Durch einen verbesserten, sogenannten *Monochromator* wurde die Energieauflösung der Methode erheblich verbessert. Dies bedeutet, dass es jetzt möglich ist, kleinere Unterschiede in der Geschwindigkeit der Elektronen nach der Wechselwirkung mit der Probe zu messen. Ähnlich wie das Elektronenmikroskop die Tür zur Nanowelt öffnete, öffnete der Monochromator das Tor zur Welt der Messung von atomschwingungsbezogenen Eigenschaften im STEM auf der Nano- und Atomebene. EELS von atomaren Schwingungen hat daher großes Potenzial, unser Verständnis des Wärmefflusses auf Nano- und Atomskala voranzutreiben, was dazu beitragen könnte, Wärme in Mikrochips besser zu steuern, neue Heiz- oder Kühltechniken zu erfinden und Materialien für Energieanwendungen zu entwickeln.

Allerdings ist die Wechselwirkung der Strahlelektronen mit der Probe recht kompliziert. Elektronen interagieren oftmals nicht nur einmal, sondern mehrmals mit der Probe, insbesondere bei dickeren Proben. Diese Möglichkeit mehrfacher Interaktionen erschwert die Interpretation von Experimenten und daher ist es oft erforderlich, die experimentellen Ergebnisse mit einem Modell der Wechselwirkung zwischen Strahl und Probe zu verifizieren. Diese Dissertation präsentiert eine Übersicht über eine neue Methode zur Modellierung dieser komplizierten Wechselwirkung zwischen Probe und Strahlelektronen für EELS von Atomschwingungen.

Wir haben dieses Modell namens FRFPMS-Methode in einer Reihe von Artikeln vorgestellt. Unser Modell ermöglicht neben der Modellierung der inelastischen Wechselwirkung auch die Berücksichtigung mehrfacher elastischer Wechselwirkungen mit der Probe. Außerdem ist es auch für Systeme, die große Berechnungen erfordern, wie etwa Proben mit Defekten und Grenzflächen, mit endlichem Zeitaufwand berechenbar.

Der Name unseres Modells, die *Frequency-Resolved Frozen Phonon Multislice* (FRFPMS) Methode, erscheint Nichteingeweihten eher ungnädig. Daher werden wir ihn hier kurz erläutern. Eine sogenannte *Multislice*-Berechnung ist, einfach gesagt, eine Berechnung der Wahrscheinlichkeit, dass sich ein Strahlelektron nach der (mehrfachen) elastischen Wechselwirkung mit der Probe in eine bestimmte Richtung bewegt. Das Ergebnis der Berechnung hängt hauptsächlich von der Position der Atome in der Probe ab. Die *Frozen Phonon Multislice* (FPMS) Methode ist eine Standardmethode zur Berechnung des Effekts thermischer Vibrationen auf STEM-Bilder. Dabei werden viele *Multislice*-Berechnungen für verschiedene thermische Verschiebungen der Atompositionen durchgeführt. Die Mittelung dieser Berechnungen ermöglicht es uns, die Wahrscheinlichkeit der inelastischen Wechselwirkung der Strahlelektronen mit den Schwingungsanregungen der Atome in der Probe über alle Schwingungsenergien hinweg zu extra-

hieren. Unser Modell erweitert die FPMS Methode um eine *Frequenzauflösung*.

Wir erläutern dieses Konzept kurz: Herkömmlichen Modelle der Atom-Bewegung, die in Verbindung mit der FPMS-Methode verwendet werden, berücksichtigen die gesamte Bandbreite möglicher Vibrationen. Mit Hinblick auf EELS von Atomschwingungen möchten wir jedoch wissen, wie viele Elektronen innerhalb eines bestimmten Energiebereichs interagiert haben. Hier kommt die zuvor erwähnte *Frequenzauflösung* der FRFPMS-Methode ins Spiel.

Die Kernidee der FRFPMS-Methode ist dann einfach: Um die Wahrscheinlichkeit des Austauschs einer bestimmten Energiemenge zu modellieren, müssen wir einfach die Bandbreite der möglichen Atomschwingungen reduzieren. Wir können dann die gleiche Mittelung wie innerhalb der FPMS-Methode anwenden, um die Wahrscheinlichkeit der inelastischen Wechselwirkung zu berechnen. Indem wir dieses Verfahren für jeden Frequenzbereich wiederholen, an dem wir interessiert sind, können wir das vollständige Bild der Wahrscheinlichkeit des Energieaustauschs mit Vibrationen in der Probe aufbauen und so helfen, das Verständnis der Atombewegung und des Wärmeflusses auf kleinster Ebene zu erweitern.

Artikel I stellt diese Idee der FRFPMS Methode vor. In den Artikeln II und III setzen wir die Idee weiter in die Praxis um und vergleichen ihre Vorhersagen mit anderen experimentellen und theoretischen Ergebnissen. Die Hauptbotschaft dieser Artikel ist, dass unser Modell mit anderen Forschungsergebnissen übereinstimmt, wenn vergleichbare Bedingungen vorliegen, aber dass unser Modell auch ein gewisses Extra im Vergleich zu anderen Modellen bietet. Es ist beispielsweise in der Lage, mehrfache elastische Streuung zu berücksichtigen und ist außerdem für Systeme berechenbar, die große Modelle der Atompositionen benötigen.

Trotz dieser Erfolge in der praktischen Modellierung haben wir uns Fragen darüber gestellt, welche Art von Vereinfachungen die FRFPMS-Methode macht. Daher vergleichen wir die FRFPMS-Methode in Artikel IV mit anderen etablierten theoretischen Ansätzen für eine stark vereinfachte Situation. Wir nehmen an, dass die Strahlelektronen nur mit einem einzigen Kohlenstoffatom wechselwirken, das als sogenannter quantenmechanischer harmonischer Oszillator (QHO) modelliert wird, dem einfachsten Modell für ein gebundenes Atom. Wir zeigen, dass das Verfahren der FRFPMS-Methode identische Ergebnisse zu anderen Theorien liefert, vorausgesetzt, wir modifizieren unsere Methode in zwei Punkten. Die Modifikationen betreffen eine Änderung der Skalierung der berechneten Wahrscheinlichkeiten mit der Temperatur und der ausgetauschten Energie sowie eine Reduzierung der Wahrscheinlichkeit, dass Elektronen unter einem großen Winkel von ihrer ursprünglichen Bewegungsrichtung abgelenkt werden. Wir bezeichnen diese modifizierte FRFPMS-Methode als die *überarbeitete* FRFPMS-Methode.

Die letzten beiden Artikel sind das Ergebnis von Zusammenarbeit mit experimentellen Kollegen, und wir modellieren explizite Experimente mit der modifizierten FRFPMS-Methode. In Artikel V betrachten wir den Effekt unterschiedlicher Isotopenzusammensetzungen in hBN. Isotope sind Atome des gleichen Elements mit unterschiedlicher Masse. Sie teilen daher viele chemische Eigenschaften, aber die atomare Masse beeinflusst die atomaren Schwingungsfrequenzen. Im Einklang mit Erwartungen, Experimenten und anderen Arbeiten zu diesem Thema stellen wir fest, dass die höchsten Schwingungsenergien in hBN von der Isotopenzusammensetzung beeinflusst werden und für größere Isotopenmasse zu niedrigeren Werten verschoben werden. Wir zeigen, dass es möglich ist, diese Verschiebung mittels EELS in Abhängigkeit von der Richtung zu messen, in der sich die Elektronen nach der Wechselwirkung bewegen. Im letzten Artikel, Artikel VI, ermöglichten uns unsere Berechnungen es, einen interessanten Effekt zu interpretieren, der zu Beginn unserer Zusammenarbeit nicht erwartet wurde. Wir beobachten sowohl im Experiment als auch in der Theorie anhand eines Materials namens Strontiumtitanat (STO), dass Bilder der Wahrscheinlichkeit der inelastischen Wechselwirkung in der Nähe von Sauerstoffatomen empfindlich auf die Richtung reagieren, in der sich die inelastischen Elektronen nach ihrer Wechselwirkung mit der Probe bewegen. Wir erklären dieses Phänomen mit der Anisotropie der Bewegung von Sauerstoffatomen in STO, was einfach gesagt bedeutet, dass sich Sauerstoffatome entlang einer Achse mehr bewegen als entlang einer anderen. Diese Anisotropie ist seit langem bekannt, aber wir konnten sie hier zum ersten Mal als Funktion der Schwingungsfrequenz abbilden und zeigen, dass sich die Richtung der atomaren Bewegung der Sauerstoffatome in STO von niedrigen hin zu hohen Schwingungsfrequenzen ändert.

Zusammenfassend tragen wir mit dieser Arbeit ein effizientes und vielseitiges rechnerisches Modell zur Simulation und Interpretation von EELS für Atomschwingungen bei. EELS ist heutzutage ein wichtiges Werkzeug für die Untersuchung von Wärme auf kleinsten Längenskalen im Nano- und Atombereich, mit vielen potenziellen Anwendungen in der Materialwissenschaft und dem Nanoingenieurwesen.

9. Acknowledgements

I would like to express my deep gratitude to my “academic father” Ján for his guidance during the last 9 years, his trust in me and my abilities, and his immense patience with me. I am also really thankful for the many opportunities to visit conferences and work on interesting side-projects Ján offered me. I will really miss working with you here in Uppsala, but I am sure that we will continue to collaborate on many future projects. After all, the story of the FRFPMS is not finished yet! I would also like to thank my co-supervisors Hermann, Olle, and especially Peter for taking on this role. We have not worked much together, but I enjoyed the discussions with you and the life advice from you.

Vanda, you are truly my “partner in crime”, La Peligrosa, queen of the dangerous and love of my life. Thank you for sharing this life with me! I am so lucky to have you and I am deeply grateful for your unwavering support and love, even when I am writing a thesis. I am looking forward to a future full of new adventures and experiences with you.

I am truly indebted for life to my family, especially my parents Kerstin and Robert. You have always supported my decisions and choice of path in life and provided me with with ample of opportunities to grow and learn. Without you, I would not be where I am and I would not have written this dissertation. Also my sister Caren is always there for me with an open ear, a place to sleep after weeks of biking or skiing, and a wet suit to go freediving and spearfishing. Thank you, mum and dad and Caren!

El Cartel, you have been a fun and creative bunch of colleagues and I will always remember our meetings and common lunch breaks! Thank you El Diablo, El Carnisero, Keenan, Los Ossitos, Justyn and El Jefe de Jefes. Also the cartel overseas is recognized for discussions, collaborations and future plans. Thank you, El Presidente and La Estrella! Another big thanks to my co-authors Ján, Xingxu, Juri, Les, Jordan, Demie, Quentin, Xiaoqing, Yifeng, Chait, and Hongbin, who have all contributed in their own way to the papers in this dissertation and my future.

An important part of a PhD is the time not spent on progressing the thesis work. I am very thankful to all my friends, who helped me take time off from all the thinking about electrons and phonons. Specifically I would like to honor the “rats”, Emma, Josh, Reinier and Vanda, for many fun hours cooking, eating, playing, watching movies, and talking life in Uppsala. And also for a multitude of fun trips around Sweden and proof reading the popular summary of this dissertation! Angel, Brenda, Leandro,

Rafael, Vanda and Wuyihan, you guys have made many evenings a blast with dinners, playing analog and digital games, and discussions about life and the world. I am also really grateful to have climbed a lot with the legends Tor, James, and Vanda all around Scandinavia. You guys rock and I hope that we will find time for more trips in the mountains in the future. More recently, I met Lennart through the PhD mentoring program and we have shared some fun boulder sessions, evenings and a rock concert, which I will always remember. I am also grateful for my friend Kai from kindergarten days, who is always there for an adventure and enjoying life, and Max from high school days, with whom I can always have an insightful discussion on the state of politics and play any multi-hour board game. Furthermore Rafael in particular has been a pillar of support and commiseration during the last weeks of finishing this dissertation. We have had many meals, and tea and coffee breaks together, which really helped me keep my sanity.

I would also like to thank my office mates over time, Leandro, Jérôme, Francesco C., Francesco F., and Sanaz, for a great atmosphere, and many scientific and non-scientific discussions in the office, which anyone has access to. I am also thankful for the entire division of Materials Theory, which has accommodated me for all these years and which I had the honor to serve as a PhD representative for. Thank you for the common lunches, fikas, discussions, board games, ping pong and activities, Alena, Andreas, Ángel, Duo, Francesco C., Francesco F., Felix, Heike, Ivan, Jérôme, Leandro, Lucas, Madhura, Markus, Mohamed, Mrudul, Nabil, Nastaran, Pablo, Patric, Quentin, Rafael, Raquel, Renan, Rohit, Rodrigo, Sebastian K., Sanaz, Soheil, Vladislav, and anyone else I might have forgotten in the stress of finishing. I have also received valuable guidance from Ralph, Peter, and Susanne on plans for my future.

I spent a considerable amount of time on teaching during my PhD studies. I would like to express my gratitude to Andreas, Christina, Ibrahim, Julia, Lucile, Michael, Nanny, Sebastian C., and Simon, for the enjoyable time of teaching labs together. Susanne, Anders, Ján, and Nic, have also guided and entrusted me with teaching responsibilities, which helped me grow personally and as an academic.

Last but not least, I am grateful to have served as a representative to the department board, the work environment board, and the PhD council at the Department of Physics and Astronomy. I have learned a lot about the university environment and the common issues faced by many in academia during this time and I will remember these lessons for the future. This dissertation would also not be possible without funding by the Swedish Research Council. Simulations were enabled by resources provided by the Swedish National Infrastructure for Computing (SNIC) at NSC Centre partially funded by the Swedish Research Council through Grant Agreement No. 2018-05973. Another special thanks goes out to Staffan, whose Injera

has been a staple for many years now, and also to ChatGPT for help with translating the popular science summary of this dissertation.

Bibliography

- [1] E. Ruska, The development of the electron microscope and of electron microscopy, *Bioscience Reports* **7**, 607–629 (1987).
- [2] C. Davisson and L. H. Germer, Diffraction of Electrons by a Crystal of Nickel, *Physical Review* **30**, 705–740 (1927).
- [3] C. Davisson and L. H. Germer, The Scattering of Electrons by a Single Crystal of Nickel, *Nature* **119**, 558–560 (1927).
- [4] G. P. Thomson and A. Reid, Diffraction of Cathode Rays by a Thin Film, *Nature* **119**, 890–890 (1927).
- [5] C. J. Davisson and L. H. Germer, Reflection of Electrons by a Crystal of Nickel, *Proceedings of the National Academy of Sciences of the United States of America* **14**, 317–322 (1928).
- [6] Wikipedia TEM schematic, <https://w.wiki/8VGC> (2009-03-22).
- [7] M. Knoll, Aufladepotential und Sekundäremission elektronenbestrahlter Körper, *Zeitschrift für Technische Physik* **16**, 467 (1935).
- [8] M. von Ardenne, Das Elektronen-Rastermikroskop, *Zeitschrift für Physik* **109**, 553–572 (1938).
- [9] C. W. Oatley, W. C. Nixon, and R. F. W. Pease, Scanning electron microscopy, in *Advances in Electronics and Electron Physics*, Vol. 21, edited by L. Marton (Academic Press, 1966) pp. 181–247.
- [10] A. V. Crewe, Scanning electron microscopes: Is high resolution possible?, *Science* **154**, 729–738 (1966).
- [11] A. V. Crewe, J. Wall, and L. M. Welter, A High-Resolution Scanning Transmission Electron Microscope, *Journal of Applied Physics* **39**, 5861–5868 (1968).
- [12] A. V. Crewe, J. Wall, and J. Langmore, Visibility of Single Atoms, *Science* **168**, 1338–1340 (1970).
- [13] D. B. Williams and C. B. Carter, *Transmission Electron Microscopy* (Springer US, Boston, MA, 2009).
- [14] Wikipedia schematic of EELS features, <https://w.wiki/8VGA> (2017-06-17).
- [15] P. Schattschneider, S. Rubino, C. Hébert, J. Rusz, J. Kuneš, P. Novák, E. Carlino, M. Fabrizioli, G. Panaccione, and G. Rossi, Detection of magnetic circular dichroism using a transmission electron microscope, *Nature* **441**, 486–488 (2006).
- [16] S. J. Pennycook, Fulfilling Feynman’s dream: “Make the electron microscope 100 times better”—Are we there yet?, *MRS Bulletin* **40**, 71–78 (2015).
- [17] Z. Chen, Y. Jiang, Y.-T. Shao, M. E. Holtz, M. Odstrčil, M. Guizar-Sicairos, I. Hanke, S. Ganschow, D. G. Schlom, and D. A. Muller, Electron ptychography achieves atomic-resolution limits set by lattice vibrations, *Science* **372**, 826–831 (2021).

- [18] M. Haider, S. Uhlemann, E. Schwan, H. Rose, B. Kabius, and K. Urban, Electron microscopy image enhanced, *Nature* **392**, 768–769 (1998).
- [19] P. E. Batson, N. Dellby, and O. L. Krivanek, Sub-ångstrom resolution using aberration corrected electron optics, *Nature* **418**, 617–620 (2002).
- [20] T. Akashi, Y. Takahashi, T. Tanigaki, T. Shimakura, T. Kawasaki, T. Furutsu, H. Shinada, H. Müller, M. Haider, N. Osakabe, and A. Tonomura, Aberration corrected 1.2-MV cold field-emission transmission electron microscope with a sub-50-pm resolution, *Applied Physics Letters* **106**, 074101 (2015).
- [21] H. Sawada, N. Shimura, F. Hosokawa, N. Shibata, and Y. Ikuhara, Resolving 45-pm-separated Si–Si atomic columns with an aberration-corrected STEM, *Microscopy* **64**, 213–217 (2015).
- [22] S. Morishita, M. Mukai, K. Suenaga, and H. Sawada, Resolution enhancement in transmission electron microscopy with 60-kV monochromated electron source, *Applied Physics Letters* **108**, 013107 (2016).
- [23] S. Morishita, R. Ishikawa, Y. Kohno, H. Sawada, N. Shibata, and Y. Ikuhara, Resolution Achievement of 40.5 pm in Scanning Transmission Electron Microscopy using 300 kV Microscope with Delta Corrector, *Microscopy and Microanalysis* **24**, 120–121 (2018).
- [24] M. P. Oxley, A. R. Lupini, and S. J. Pennycook, Ultra-high resolution electron microscopy, *Reports on Progress in Physics* **80**, 026101 (2016).
- [25] O. L. Krivanek, T. C. Lovejoy, N. Dellby, T. Aoki, R. W. Carpenter, P. Rez, E. Soignard, J. Zhu, P. E. Batson, M. J. Lagos, R. F. Egerton, and P. A. Crozier, Vibrational spectroscopy in the electron microscope, *Nature* **514**, 209 (2014).
- [26] O. L. Krivanek, N. Dellby, J. A. Hachtel, J.-C. Idrobo, M. T. Hotz, B. Plotkin-Swing, N. J. Bacon, A. L. Bleloch, G. J. Corbin, M. V. Hoffman, C. E. Meyer, and T. C. Lovejoy, Progress in ultrahigh energy resolution EELS, *Ultramicroscopy* **203**, 60 – 67 (2019).
- [27] N. Dellby, T. Lovejoy, G. Corbin, N. Johnson, R. Hayner, M. Hoffman, P. Hrncrik, B. Plotkin-Swing, D. Taylor, and O. Krivanek, Ultra-high Energy Resolution EELS, *Microscopy and Microanalysis* **26**, 1804–1805 (2020).
- [28] K. Lyon, A. Bergman, P. Zeiger, D. Kepaptsoglou, Q. M. Ramasse, J. C. Idrobo, and J. Rusz, Theory of magnon diffuse scattering in scanning transmission electron microscopy, *Physical Review B* **104**, 214418 (2021).
- [29] B. G. Mendis, A semi-classical theory of magnetic inelastic scattering in transmission electron energy loss spectroscopy, *Ultramicroscopy* **230**, 113390 (2021).
- [30] B. G. Mendis, Quantum theory of magnon excitation by high energy electron beams, *Ultramicroscopy* **239**, 113548 (2022).
- [31] J. Á. Castellanos-Reyes, P. Zeiger, A. Bergman, D. Kepaptsoglou, Q. M. Ramasse, J. C. Idrobo, and J. Rusz, Unveiling the impact of temperature on magnon diffuse scattering detection in the transmission electron microscope, *Physical Review B* **108**, 134435 (2023).
- [32] H. Boersch, J. Geiger, and H. Hellwig, Steigerung der Auflösung bei der elektronen-energieanalyse, *Physics Letters* **3**, 64–66 (1962).

- [33] H. Boersch, J. Geiger, and W. Stickel, Anregung von molekülschwingungen durch schnelle elektronen, *Physics Letters* **10**, 285–286 (1964).
- [34] H. Boersch, J. Geiger, and W. Stickel, Interaction of 25-keV Electrons with Lattice Vibrations in LiF. Experimental Evidence for Surface Modes of Lattice Vibration, *Physical Review Letters* **17**, 379–381 (1966).
- [35] B. Schröder and J. Geiger, Electron-Spectrometric Study of Amorphous Germanium and Silicon in the Two-Phonon Region, *Physical Review Letters* **28**, 301–303 (1972).
- [36] J. Geiger and H. Katterwe, Differences in the interaction of fast electrons with crystalline and amorphous titanium oxide films, *Thin Solid Films* **32**, 359–361 (1976).
- [37] J. A. Hachtel, A. R. Lupini, and J. C. Idrobo, Exploring the capabilities of monochromated electron energy loss spectroscopy in the infrared regime, *Scientific Reports* **8**, 1–10 (2018).
- [38] B. Plotkin-Swing, G. J. Corbin, S. De Carlo, N. Dellby, C. Hoermann, M. V. Hoffman, T. C. Lovejoy, C. E. Meyer, A. Mittelberger, R. Pantelic, L. Piazza, and O. L. Krivanek, Hybrid pixel direct detector for electron energy loss spectroscopy, *Ultramicroscopy* **217**, 113067 (2020).
- [39] C. Dwyer, Localization of high-energy electron scattering from atomic vibrations, *Phys. Rev. B* **89**, 054103 (2014).
- [40] K. Venkatraman and P. A. Crozier, Role of Convergence and Collection Angles in the Excitation of Long- and Short-Wavelength Phonons with Vibrational Electron Energy-Loss Spectroscopy, *Microscopy and Microanalysis*, 1–9 (2021).
- [41] S. J. Pennycook and L. A. Boatner, Chemically sensitive structure-imaging with a scanning transmission electron microscope, *Nature* **336**, 565–567 (1988).
- [42] S. J. Pennycook and D. E. Jesson, High-resolution incoherent imaging of crystals, *Physical Review Letters* **64**, 938–941 (1990).
- [43] R. F. Egerton, Vibrational-loss EELS and the avoidance of radiation damage, *Ultramicroscopy* **159**, 95–100 (2015).
- [44] P. Rez, T. Aoki, K. March, D. Gur, O. L. Krivanek, N. Dellby, T. C. Lovejoy, S. G. Wolf, and H. Cohen, Damage-free vibrational spectroscopy of biological materials in the electron microscope, *Nature Communications* **7**, 10945 (2016).
- [45] P. A. Crozier, Vibrational and valence aloof beam EELS: A potential tool for nondestructive characterization of nanoparticle surfaces, *Ultramicroscopy* **180**, 104–114 (2017).
- [46] P. A. Crozier, T. Aoki, and Q. Liu, Detection of water and its derivatives on individual nanoparticles using vibrational electron energy-loss spectroscopy, *Ultramicroscopy* **169**, 30–36 (2016).
- [47] J. C. Idrobo, A. R. Lupini, T. Feng, R. R. Unocic, F. S. Walden, D. S. Gardiner, T. C. Lovejoy, N. Dellby, S. T. Pantelides, and O. L. Krivanek, Temperature Measurement by a Nanoscale Electron Probe Using Energy Gain and Loss Spectroscopy, *Physical Review Letters* **120**, 095901 (2018).
- [48] M. J. Lagos and P. E. Batson, Thermometry with Subnanometer Resolution in the Electron Microscope Using the Principle of Detailed Balancing,

- Nano Letters **18**, 4556–4563 (2018).
- [49] J. R. Jokisaari, J. A. Hachtel, X. Hu, A. Mukherjee, C. Wang, A. Konecna, T. C. Lovejoy, N. Dellby, J. Aizpurua, O. L. Krivanek, J.-C. Idrobo, and R. F. Klie, Vibrational Spectroscopy of Water with High Spatial Resolution, *Advanced Materials* **30**, 1802702 (2018).
 - [50] J. A. Hachtel, J. Huang, I. Popovs, S. Jansone-Popova, J. K. Keum, J. Jakowski, T. C. Lovejoy, N. Dellby, O. L. Krivanek, and J. C. Idrobo, Identification of site-specific isotopic labels by vibrational spectroscopy in the electron microscope, *Science* **363**, 525–528 (2019).
 - [51] D. L. Mills and E. Burstein, Polaritons: the electromagnetic modes of media, *Reports on Progress in Physics* **37**, 817 (1974).
 - [52] C. H. Henry and J. J. Hopfield, Raman Scattering by Polaritons, *Physical Review Letters* **15**, 964–966 (1965).
 - [53] D. N. Basov, M. M. Fogler, and F. J. García de Abajo, Polaritons in van der Waals materials, *Science* **354**, aag1992 (2016), publisher: American Association for the Advancement of Science.
 - [54] R. Ruppin and R. Englman, Optical phonons of small crystals, *Reports on Progress in Physics* **33**, 149 (1970).
 - [55] A. A. Govyadinov, A. Konečná, A. Chuvilin, S. Vélez, I. Dolado, A. Y. Nikitin, S. Lopatin, F. Casanova, L. E. Hueso, J. Aizpurua, and R. Hillenbrand, Probing low-energy hyperbolic polaritons in van der Waals crystals with an electron microscope, *Nature Communications* **8**, 10.1038/s41467-017-00056-y (2017).
 - [56] N. Li, X. Guo, X. Yang, R. Qi, T. Qiao, Y. Li, R. Shi, Y. Li, K. Liu, Z. Xu, L. Liu, F. J. García de Abajo, Q. Dai, E.-G. Wang, and P. Gao, Direct observation of highly confined phonon polaritons in suspended monolayer hexagonal boron nitride, *Nature Materials* **20**, 43–48 (2021).
 - [57] A. Konečná, J. Li, J. H. Edgar, F. J. García de Abajo, and J. A. Hachtel, Revealing Nanoscale Confinement Effects on Hyperbolic Phonon Polaritons with an Electron Beam, *Small* **17**, 2103404 (2021).
 - [58] X. Li, G. Haberfehlner, U. Hohenester, O. Stéphan, G. Kothleitner, and M. Kociak, Three-dimensional vectorial imaging of surface phonon polaritons, *Science* **371**, 1364–1367 (2021), publisher: American Association for the Advancement of Science.
 - [59] R. Egoavil, N. Gauquelin, G. T. Martinez, S. Van Aert, G. Van Tendeloo, and J. Verbeeck, Atomic resolution mapping of phonon excitations in STEM-EELS experiments, *Ultramicroscopy* **147**, 1–7 (2014).
 - [60] F. Hage, D. Kepaptsoglou, Q. Ramasse, and L. Allen, Phonon Spectroscopy at Atomic Resolution, *Physical Review Letters* **122**, 016103 (2019).
 - [61] K. Venkatraman, B. D. A. Levin, K. March, P. Rez, and P. A. Crozier, Vibrational spectroscopy at atomic resolution with electron impact scattering, *Nature Physics* **15**, 1237–1241 (2019).
 - [62] C. Dwyer, T. Aoki, P. Rez, S. L. Y. Chang, T. C. Lovejoy, and O. L. Krivanek, Electron-Beam Mapping of Vibrational Modes with Nanometer Spatial Resolution, *Phys. Rev. Lett.* **117**, 256101 (2016).
 - [63] F. S. Hage, Q. M. Ramasse, and L. J. Allen, Contrast reversal in atomic-scale phonon spectroscopic imaging, *Physical Review B* **102**, 214111 (2020).

- [64] F. S. Hage, G. Radtke, D. M. Kepaptsoglou, M. Lazzeri, and Q. M. Ramasse, Single-atom vibrational spectroscopy in the scanning transmission electron microscope, *Science* **367**, 1124–1127 (2020).
- [65] M. Xu, D.-L. Bao, A. Li, M. Gao, D. Meng, A. Li, S. Du, G. Su, S. J. Pennycook, S. T. Pantelides, and W. Zhou, Single-atom vibrational spectroscopy with chemical-bonding sensitivity, *Nature Materials* **22**, 612–618 (2023).
- [66] X. Yan, C. Liu, C. A. Gadre, L. Gu, T. Aoki, T. C. Lovejoy, N. Dellby, O. L. Krivanek, D. G. Schlom, R. Wu, and X. Pan, Single-defect phonons imaged by electron microscopy, *Nature* **589**, 65–69 (2021).
- [67] Z. Cheng, R. Li, X. Yan, G. Jernigan, J. Shi, M. E. Liao, N. J. Hines, C. A. Gadre, J. C. Idrobo, E. Lee, K. D. Hobart, M. S. Goorsky, X. Pan, T. Luo, and S. Graham, Experimental observation of localized interfacial phonon modes, *Nature Communications* **12**, 6901 (2021).
- [68] Y.-H. Li, R.-S. Qi, R.-C. Shi, J.-N. Hu, Z.-T. Liu, Y.-W. Sun, M.-Q. Li, N. Li, C.-L. Song, L. Wang, Z.-B. Hao, Y. Luo, Q.-K. Xue, X.-C. Ma, and P. Gao, Atomic-scale probing of heterointerface phonon bridges in nitride semiconductor, *Proceedings of the National Academy of Sciences* **119**, e2117027119 (2022).
- [69] E. R. Hoglund, D.-L. Bao, A. O’Hara, S. Makarem, Z. T. Piontkowski, J. R. Matson, A. K. Yadav, R. C. Haislmaier, R. Engel-Herbert, J. F. Ihlefeld, J. Ravichandran, R. Ramesh, J. D. Caldwell, T. E. Beechem, J. A. Tomko, J. A. Hachtel, S. T. Pantelides, P. E. Hopkins, and J. M. Howe, Emergent interface vibrational structure of oxide superlattices, *Nature* **601**, 556–561 (2022).
- [70] E. R. Hoglund, D.-L. Bao, A. O’Hara, T. W. Pfeifer, M. S. B. Hoque, S. Makarem, J. M. Howe, S. T. Pantelides, P. E. Hopkins, and J. A. Hachtel, Direct Visualization of Localized Vibrations at Complex Grain Boundaries, *Advanced Materials* **35**, 2208920 (2023).
- [71] R. Senga, Y.-C. Lin, S. Morishita, R. Kato, T. Yamada, M. Hasegawa, and K. Suenaga, Imaging of isotope diffusion using atomic-scale vibrational spectroscopy, *Nature* **603**, 68–72 (2022).
- [72] F. S. Hage, T. P. Hardcastle, A. J. Scott, R. Brydson, and Q. M. Ramasse, Momentum- and space-resolved high-resolution electron energy loss spectroscopy of individual single-wall carbon nanotubes, *Physical Review B* **95**, 195411 (2017).
- [73] F. S. Hage, R. J. Nicholls, J. R. Yates, D. G. McCulloch, T. C. Lovejoy, N. Dellby, O. L. Krivanek, K. Refson, and Q. M. Ramasse, Nanoscale momentum-resolved vibrational spectroscopy, *Science Advances* **4**, aar7495 (2018).
- [74] R. Senga, K. Suenaga, P. Barone, S. Morishita, F. Mauri, and T. Pichler, Position and momentum mapping of vibrations in graphene nanostructures, *Nature* **573**, 247–250 (2019).
- [75] R. Qi, N. Li, J. Du, R. Shi, Y. Huang, X. Yang, L. Liu, Z. Xu, Q. Dai, D. Yu, and P. Gao, Four-dimensional vibrational spectroscopy for nanoscale mapping of phonon dispersion in BN nanotubes, *Nature Communications* **12**, 1179 (2021), number: 1 Publisher: Nature Publishing Group.

- [76] R. Qi, R. Shi, Y. Li, Y. Sun, M. Wu, N. Li, J. Du, K. Liu, C. Chen, J. Chen, F. Wang, D. Yu, E.-G. Wang, and P. Gao, Measuring phonon dispersion at an interface, *Nature* **599**, 399–403 (2021).
- [77] C. A. Gadre, X. Yan, Q. Song, J. Li, L. Gu, H. Huyan, T. Aoki, S.-W. Lee, G. Chen, R. Wu, and X. Pan, Nanoscale imaging of phonon dynamics by electron microscopy, *Nature* **606**, 292–297 (2022).
- [78] M. J. Lagos, A. Trügler, U. Hohenester, and P. E. Batson, Mapping vibrational surface and bulk modes in a single nanocube, *Nature* **543**, 529–532 (2017).
- [79] X. Yan, C. Liu, C. A. Gadre, S. Dai, L. Gu, K. Yu, T. Aoki, R. Wu, and X. Pan, Unexpected Strong Thermally Induced Phonon Energy Shift for Mapping Local Temperature, *Nano Letters* **19**, 7494–7502 (2019).
- [80] K. Venkatraman, P. Rez, K. March, and P. A. Crozier, The influence of surfaces and interfaces on high spatial resolution vibrational EELS from SiO₂, *Microscopy* **67**, i14–i23 (2018).
- [81] S. M. Collins, D. M. Kepaptsoglou, J. Hou, C. W. Ashling, G. Radtke, T. D. Bennett, P. A. Midgley, and Q. M. Ramasse, Functional Group Mapping by Electron Beam Vibrational Spectroscopy from Nanoscale Volumes, *Nano Letters* **20**, 1272–1279 (2020).
- [82] H. Yoshioka, Effect of Inelastic Waves on Electron Diffraction, *Journal of the Physical Society of Japan* **12**, 618–628 (1957).
- [83] C. R. Hall and P. B. Hirsch, Effect of thermal diffuse scattering on propagation of high energy electrons through crystals, *Proceedings of the Royal Society of London. Series A. Mathematical and Physical Sciences* **286**, 158–177 (1965).
- [84] R. F. Loane, P. Xu, and J. Silcox, Thermal vibrations in convergent-beam electron diffraction, *Acta Crystallographica Section A: Foundations of Crystallography* **47**, 267–278 (1991).
- [85] F. J. García de Abajo, Optical excitations in electron microscopy, *Reviews of Modern Physics* **82**, 209–275 (2010).
- [86] A. Konečná, *Theoretical description of low-energy excitations in nanostructures as probed by fast electrons*, PhD Thesis, University of the Basque Country (2019).
- [87] G. Radtke, D. Taverna, M. Lazzeri, and E. Balan, First-Principles Vibrational Electron Energy Loss Spectroscopy of β -Guanine, *Physical Review Letters* **119**, 027402 (2017).
- [88] A. Konečná, K. Venkatraman, K. March, P. A. Crozier, R. Hillenbrand, P. Rez, and J. Aizpurua, Vibrational electron energy loss spectroscopy in truncated dielectric slabs, *Physical Review B* **98**, 205409 (2018).
- [89] G. Radtke, D. Taverna, N. Menguy, S. Pandolfi, A. Courac, Y. Le Godec, O. Krivanek, and T. Lovejoy, Polarization Selectivity in Vibrational Electron-Energy-Loss Spectroscopy, *Physical Review Letters* **123**, 256001 (2019).
- [90] R. F. Egerton, K. Venkatraman, K. March, and P. A. Crozier, Properties of Dipole-Mode Vibrational Energy Losses Recorded from a TEM Specimen, *Microscopy and Microanalysis* **26**, 1117–1123 (2020).

- [91] U. Hohenester, A. Trügler, P. E. Batson, and M. J. Lagos, Inelastic vibrational bulk and surface losses of swift electrons in ionic nanostructures, *Physical Review B* **97**, 165418 (2018).
- [92] R. J. Nicholls, F. S. Hage, D. G. McCulloch, Q. M. Ramasse, K. Refson, and J. R. Yates, Theory of momentum-resolved phonon spectroscopy in the electron microscope, *Physical Review B* **99**, 094105 (2019).
- [93] N. W. Ashcroft and N. D. Mermin, *Solid State Physics* (Brooks/Cole, Cengage learning, Belmont, USA, 1976).
- [94] B. Dörner, *Coherent inelastic neutron scattering in lattice dynamics*, Vol. 93 (Springer, Berlin, Heidelberg, 1982).
- [95] P. Brüesch, *Phonons: Theory and Experiments II: Experiments and Interpretation of Experimental Results*, edited by M. Cardona, P. Fulde, K. von Klitzing, and H.-J. Queisser, Vol. 65 (Springer Berlin Heidelberg, Berlin, Heidelberg, 1986).
- [96] P. C. H. Mitchell, S. F. Parker, A. J. Ramirez-Cuesta, and J. Tomkinson, *Vibrational Spectroscopy with Neutrons*, Vol. 3 (World Scientific, 2005).
- [97] E. Burkel, *Inelastic Scattering: of X-Rays with Very High Energy Resolution*, 125 (Springer-Verlag Springer e-books, Berlin, Heidelberg, 2006).
- [98] G. L. Squires, *Introduction to the Theory of Thermal Neutron Scattering*, 3rd ed. (Cambridge University Press, Cambridge, 2012).
- [99] L. Van Hove, Correlations in Space and Time and Born Approximation Scattering in Systems of Interacting Particles, *Physical Review* **95**, 249–262 (1954).
- [100] E. Hoglund, H. Walker, M. Hussain, D.-L. Bao, H. Ni, A. Mamun, J. Baxter, A. Khan, S. Pantelides, P. Hopkins, and J. Hachtel, *Non-equivalent Atomic Vibrations at Interfaces in a Polar Superlattice*, preprint (In Review, 2023).
- [101] H. Kohl and H. Rose, Theory of Image Formation by Inelastically Scattered Electrons in the Electron Microscope, in *Advances in Electronics and Electron Physics*, Vol. 65, edited by P. W. Hawkes (Academic Press, 1985) pp. 173–227.
- [102] A. Konečná, F. Iyikanat, and F. J. García de Abajo, Theory of Atomic-Scale Vibrational Mapping and Isotope Identification with Electron Beams, *ACS Nano* **15**, 9890–9899 (2021).
- [103] D. R. Yennie, D. G. Ravenhall, and R. N. Wilson, Phase-Shift Calculation of High-Energy Electron Scattering, *Physical Review* **95**, 500–512 (1954).
- [104] L. I. Schiff, Approximation Method for High-Energy Potential Scattering, *Physical Review* **103**, 443–453 (1956).
- [105] K. Ishizuka and N. Uyeda, A new theoretical and practical approach to the multislice method, *Acta Crystallographica Section A: Crystal Physics, Diffraction, Theoretical and General Crystallography* **33**, 740–749 (1977).
- [106] R. Glauber and V. Schomaker, The Theory of Electron Diffraction, *Physical Review* **89**, 667–671 (1953).
- [107] E. Zeitler and H. Olsen, Complex Scattering Amplitudes in Elastic Electron Scattering, *Physical Review* **162**, 1439–1447 (1967).
- [108] B. J. Malenka, Polarization in High-Energy Elastic Nucleon-Nucleus Scattering, *Physical Review* **95**, 522–526 (1954).

- [109] Z. L. Wang, *Elastic and Inelastic Scattering in Electron Diffraction and Imaging* (Plenum Press, New York, 1995).
- [110] J. M. Cowley and A. F. Moodie, The scattering of electrons by atoms and crystals. I. A new theoretical approach, *Acta Crystallographica* **10**, 609–619 (1957).
- [111] T. Mizoguchi, T. Miyata, and W. Olovsson, Excitonic, vibrational, and van der Waals interactions in electron energy loss spectroscopy, *Ultramicroscopy* **180**, 93–103 (2017).
- [112] Z. L. Wang, The ‘Frozen-Lattice’ Approach for Incoherent Phonon Excitation in Electron Scattering. How Accurate Is It?, *Acta Crystallographica Section A* **54**, 460–467 (1998).
- [113] D. Van Dyck, Is the frozen phonon model adequate to describe inelastic phonon scattering?, *Ultramicroscopy* **109**, 677–682 (2009).
- [114] T. Niermann, Scattering of fast electrons by lattice vibrations, *Physical Review B* **100**, 144305 (2019).
- [115] D. A. Muller and J. Silcox, Delocalization in inelastic scattering, *Ultramicroscopy* **59**, 195–213 (1995).
- [116] D. A. Muller, B. Edwards, E. J. Kirkland, and J. Silcox, Simulation of thermal diffuse scattering including a detailed phonon dispersion curve, *Ultramicroscopy* **86**, 371–380 (2001).
- [117] G. Möbus, T. Gemming, and P. Gumbsch, The Influence of Phonon Scattering on HREM Images, *Acta Crystallographica Section A* **54**, 83–90 (1998).
- [118] J. Biskupek, A. Chuvilin, and U. Kaiser, Evaluation of Frozen Phonons Models for Multislice Calculation of TDS, *Microscopy and Microanalysis* **13**, 130–131 (2007).
- [119] A. Rother, T. Gemming, and H. Lichte, The statistics of the thermal motion of the atoms during imaging process in transmission electron microscopy and related techniques, *Ultramicroscopy* **109**, 139–146 (2009).
- [120] R. Aveyard, R. Ferrando, R. L. Johnston, and J. Yuan, Modeling Nanoscale Inhomogeneities for Quantitative HAADF STEM Imaging, *Phys. Rev. Lett.* **113**, 075501 (2014).
- [121] A. Löfgren, P. Zeiger, V. Kocovski, and J. Ruzs, Influence of nuclear quantum effects on frozen phonon simulations of electron vortex beam HAADF-STEM images, *Ultramicroscopy* **164**, 62–69 (2016).
- [122] D. Pohl, S. Schneider, P. Zeiger, J. Ruzs, P. Tiemeijer, S. Lazar, K. Nielsch, and B. Rellinghaus, Atom size electron vortex beams with selectable orbital angular momentum, *Scientific Reports* **7**, 934 (2017).
- [123] F. F. Krause, D. Bredemeier, M. Schowalter, T. Mehrstens, T. Grieb, and A. Rosenauer, Using molecular dynamics for multislice TEM simulation of thermal diffuse scattering in AlGaN, *Ultramicroscopy* **189**, 124–135 (2018).
- [124] X. Chen, D. S. Kim, and J. M. LeBeau, A comparison of molecular dynamics potentials used to account for thermal diffuse scattering in multislice simulations, *Ultramicroscopy* , 113644 (2022).
- [125] B. D. Forbes and L. J. Allen, Modeling energy-loss spectra due to phonon excitation, *Physical Review B* **94**, 014110 (2016).

- [126] B. D. Forbes, A. V. Martin, S. D. Findlay, A. J. D’Alfonso, and L. J. Allen, Quantum mechanical model for phonon excitation in electron diffraction and imaging using a Born-Oppenheimer approximation, *Phys. Rev. B* **82**, 104103 (2010).
- [127] P. Rez and A. Singh, Lattice resolution of vibrational modes in the electron microscope, *Ultramicroscopy* **220**, 113162 (2021).
- [128] A. Amali and P. Rez, Theory of Lattice Resolution in High-angle Annular Dark-field Images, *Microscopy and Microanalysis* **3**, 28–46 (1997).
- [129] C. Dwyer, Prospects of spatial resolution in vibrational electron energy loss spectroscopy: Implications of dipolar scattering, *Physical Review B* **96**, 224102 (2017).
- [130] E. J. Kirkland, *Advanced Computing in Electron Microscopy*, 2nd ed. (Springer US, 2010).
- [131] K. Fujiwara, Relativistic Dynamical Theory of Electron Diffraction, *Journal of the Physical Society of Japan* **16**, 2226–2238 (1961).
- [132] J. W. Cooley and J. W. Tukey, An algorithm for the machine calculation of complex Fourier series, *Mathematics of Computation* **19**, 297–301 (1965).
- [133] D. v. Dyck, Improved methods for the high speed calculation of electron microscopic structure images, *physica status solidi (a)* **52**, 283–292 (1979).
- [134] D. V. Dyck, Fast computational procedures for the simulation of structure images in complex or disordered crystals: a new approach, *Journal of Microscopy* **119**, 141–152 (1980).
- [135] D. Van Dyck and W. Coene, The real space method for dynamical electron diffraction calculations in high resolution electron microscopy: I. Principles of the method, *Ultramicroscopy* **15**, 29–40 (1984).
- [136] W. Coene and D. Van Dyck, The real space method for dynamical electron diffraction calculations in high resolution electron microscopy: II. Critical analysis of the dependency on the input parameters, *Ultramicroscopy* **15**, 41–50 (1984).
- [137] W. Coene and D. van Dyck, The real space method for dynamical electron diffraction calculations in high resolution electron microscopy: III. A computational algorithm for the electron propagation with its practical applications, *Ultramicroscopy* **15**, 287–300 (1984).
- [138] C. Y. Cai, S. J. Zeng, H. R. Liu, and Q. B. Yang, Computational comparison of the conventional multislice method and the real space multislice method for simulating exit wavefunctions, *Micron* **40**, 313 (2009).
- [139] D. V. Dyck, Image Calculations in High-Resolution Electron Microscopy: Problems, Progress, and Prospects, in *Advances in Electronics and Electron Physics*, Vol. 65, edited by P. W. Hawkes (Academic Press, 1985) pp. 295–355.
- [140] P. A. Doyle and P. S. Turner, Relativistic Hartree–Fock X-ray and electron scattering factors, *Acta Crystallographica Section A: Crystal Physics, Diffraction, Theoretical and General Crystallography* **24**, 390–397 (1968).
- [141] A. Weickenmeier and H. Kohl, Computation of absorptive form factors for high-energy electron diffraction, *Acta Crystallographica Section A: Foundations of Crystallography* **47**, 590–597 (1991).

- [142] I. Lobato and D. Van Dyck, An accurate parameterization for scattering factors, electron densities and electrostatic potentials for neutral atoms that obey all physical constraints, *Acta Crystallographica Section A: Foundations and Advances* **70**, 636–649 (2014).
- [143] D. Rez, P. Rez, and I. Grant, Dirac–Fock calculations of X-ray scattering factors and contributions to the mean inner potential for electron scattering, *Acta Crystallographica Section A: Foundations of Crystallography* **50**, 481–497 (1994).
- [144] D. Waasmaier and A. Kirfel, New analytical scattering-factor functions for free atoms and ions, *Acta Crystallographica Section A* **51**, 416–431 (1995).
- [145] L.-M. Peng, Electron Scattering Factors of Ions and their Parameterization, *Acta Crystallographica Section A: Foundations of Crystallography* **54**, 481–485 (1998).
- [146] T. Gemming, G. Möbus, M. Exner, F. Ernst, and M. Rühle, Ab-initio HRTEM simulations of ionic crystals: a case study of sapphire, *Journal of Microscopy* **190**, 89–98 (1998).
- [147] S. Mogck, B. J. Kooi, J. T. M. De Hosson, and M. W. Finnis, Ab initio transmission electron microscopy image simulations of coherent Ag – MgO interfaces, *Physical Review B* **70**, 245427 (2004).
- [148] B. Deng, L. D. Marks, and J. M. Rondinelli, Charge defects glowing in the dark, *Ultramicroscopy* **107**, 374–381 (2007).
- [149] J. C. Meyer, S. Kurasch, H. J. Park, V. Skakalova, D. Künzel, A. Groß, A. Chuvilin, G. Algara-Siller, S. Roth, T. Iwasaki, U. Starke, J. H. Smet, and U. Kaiser, Experimental analysis of charge redistribution due to chemical bonding by high-resolution transmission electron microscopy, *Nature Materials* **10**, 209–215 (2011).
- [150] S. Kurasch, J. C. Meyer, D. Künzel, A. Groß, and U. Kaiser, Simulation of bonding effects in HRTEM images of light element materials, *Beilstein Journal of Nanotechnology* **2**, 394–404 (2011).
- [151] W. L. Wang and E. Kaxiras, Efficient calculation of the effective single-particle potential and its application in electron microscopy, *Physical Review B* **87**, 085103 (2013).
- [152] S. Borghardt, F. Winkler, Z. Zanolli, M. J. Verstraete, J. Barthel, A. H. Tavabi, R. E. Dunin-Borkowski, and B. E. Kardynal, Quantitative Agreement between Electron-Optical Phase Images of WSe₂ and Simulations Based on Electrostatic Potentials that Include Bonding Effects, *Physical Review Letters* **118**, 086101 (2017).
- [153] T. Susi, J. Madsen, U. Ludacka, J. J. Mortensen, T. J. Pennycook, Z. Lee, J. Kotakoski, U. Kaiser, and J. C. Meyer, Efficient first principles simulation of electron scattering factors for transmission electron microscopy, *Ultramicroscopy* **197**, 16–22 (2019).
- [154] J. Madsen, T. J. Pennycook, and T. Susi, ab initio description of bonding for transmission electron microscopy, *Ultramicroscopy* **231**, 113253 (2021).
- [155] M. Ceriotti, *A novel framework for enhanced molecular dynamics based on the generalized Langevin equation*, PhD Thesis, ETH Zurich, Zurich (2010).
- [156] C. Sevik, A. Kinaci, J. B. Haskins, and T. Cagin, Characterization of thermal transport in low-dimensional boron nitride nanostructures, *Phys.*

- Rev. B **84**, 085409 (2011).
- [157] J. H. Los, J. M. H. Kroes, K. Albe, R. M. Gordillo, M. I. Katsnelson, and A. Fasolino, Extended Tersoff potential for boron nitride: Energetics and elastic properties of pristine and defective h-BN, *Physical Review B* **96**, 184108 (2017).
 - [158] I. Leven, T. Maaravi, I. Azuri, L. Kronik, and O. Hod, Interlayer Potential for Graphene/h-BN Heterostructures, *Journal of Chemical Theory and Computation* **12**, 2896–2905 (2016).
 - [159] W. Ouyang, D. Mandelli, M. Urbakh, and O. Hod, Nanoserpents: Graphene Nanoribbon Motion on Two-Dimensional Hexagonal Materials, *Nano Letters* **18**, 6009–6016 (2018).
 - [160] W. Ouyang, I. Azuri, D. Mandelli, A. Tkatchenko, L. Kronik, M. Urbakh, and O. Hod, Mechanical and Tribological Properties of Layered Materials under High Pressure: Assessing the Importance of Many-Body Dispersion Effects, *Journal of Chemical Theory and Computation* **16**, 666–676 (2020).
 - [161] M. Rupp, Machine learning for quantum mechanics in a nutshell, *International Journal of Quantum Chemistry* **115**, 1058–1073 (2015).
 - [162] C. Chen and S. P. Ong, A universal graph deep learning interatomic potential for the periodic table, *Nature Computational Science* **2**, 718–728 (2022).
 - [163] S. Takamoto, C. Shinagawa, D. Motoki, K. Nakago, W. Li, I. Kurata, T. Watanabe, Y. Yayama, H. Iriguchi, Y. Asano, T. Onodera, T. Ishii, T. Kudo, H. Ono, R. Sawada, R. Ishitani, M. Ong, T. Yamaguchi, T. Kataoka, A. Hayashi, N. Charoenphakdee, and T. Ibuka, Towards universal neural network potential for material discovery applicable to arbitrary combination of 45 elements, *Nature Communications* **13**, 2991 (2022).
 - [164] B. Deng, P. Zhong, K. Jun, J. Riebesell, K. Han, C. J. Bartel, and G. Ceder, CHGNet as a pretrained universal neural network potential for charge-informed atomistic modelling, *Nature Machine Intelligence* **5**, 1031–1041 (2023).
 - [165] J. von Plato, Boltzmann’s ergodic hypothesis, *Archive for History of Exact Sciences* **42**, 71–89 (1991).
 - [166] S. Nosé, A molecular dynamics method for simulations in the canonical ensemble, *Molecular Physics* **52**, 255–268 (1984).
 - [167] W. G. Hoover, Canonical dynamics: Equilibrium phase-space distributions, *Physical Review A* **31**, 1695–1697 (1985).
 - [168] M. Ceriotti, G. Bussi, and M. Parrinello, Colored-Noise Thermostats à la Carte, *Journal of Chemical Theory and Computation* **6**, 1170–1180 (2010).
 - [169] G. Bussi and M. Parrinello, Accurate sampling using Langevin dynamics, *Physical Review E* **75**, 056707 (2007).
 - [170] P. H. Hünenberger, Thermostat Algorithms for Molecular Dynamics Simulations, in *Advanced Computer Simulation: Approaches for Soft Matter Sciences I*, edited by C. Dr. Holm and K. Prof. Dr. Kremer (Springer, Berlin, Heidelberg, 2005) pp. 105–149.
 - [171] T. Schneider and E. Stoll, Molecular-dynamics study of a three-dimensional one-component model for distortive phase transitions, *Physical Review B* **17**, 1302–1322 (1978).

- [172] S. Plimpton, Fast Parallel Algorithms for Short-Range Molecular Dynamics, *Journal of Computational Physics* **117**, 1 – 19 (1995).
- [173] M. Ceriotti and M. Parrinello, The δ -thermostat: selective normal-modes excitation by colored-noise Langevin dynamics, *Procedia Computer Science* **1**, 1607–1614 (2010).
- [174] M. Ceriotti, G. Bussi, and M. Parrinello, Nuclear Quantum Effects in Solids Using a Colored-Noise Thermostat, *Phys. Rev. Lett.* **103**, 030603 (2009).
- [175] M. Ceriotti and M. Parrinello, The δ -thermostat: selective normal-modes excitation by colored-noise Langevin dynamics, *Procedia Computer Science* **1**, 1607–1614 (2010).
- [176] C. Lee, D. Vanderbilt, K. Laasonen, R. Car, and M. Parrinello, Ab initio studies on the structural and dynamical properties of ice, *Physical Review B* **47**, 4863–4872 (1993).
- [177] A. Carreras, A. Togo, and I. Tanaka, DynaPhoPy: A code for extracting phonon quasiparticles from molecular dynamics simulations, *Computer Physics Communications* **221**, 221–234 (2017).
- [178] M. Born and K. Huang, *Dynamical Theory of Crystal Lattices* (Oxford University Press, Oxford, 1962).
- [179] P. Brüesch, *Phonons: Theory and Experiments I*, edited by M. Cardona, P. Fulde, and H.-J. Queisser, Vol. 34 (Springer Berlin Heidelberg, Berlin, Heidelberg, 1982).
- [180] A. Togo and I. Tanaka, First principles phonon calculations in materials science, *Scripta Materialia* **108**, 1–5 (2015).
- [181] J. Barthel, Dr. Probe: A software for high-resolution STEM image simulation, *Ultramicroscopy* **193**, 1–11 (2018).
- [182] A. De Backer, G. T. Martinez, A. Rosenauer, and S. Van Aert, Atom counting in HAADF STEM using a statistical model-based approach: Methodology, possibilities, and inherent limitations, *Ultramicroscopy* **134**, 23–33 (2013).
- [183] X. Gonze and C. Lee, Dynamical matrices, Born effective charges, dielectric permittivity tensors, and interatomic force constants from density-functional perturbation theory, *Physical Review B* **55**, 10355–10368 (1997).
- [184] F. L. Thiemann, P. Rowe, E. A. Müller, and A. Michaelides, Machine Learning Potential for Hexagonal Boron Nitride Applied to Thermally and Mechanically Induced Rippling, *The Journal of Physical Chemistry C* **124**, 22278–22290 (2020).
- [185] W. F. Goh, T. L. Yoon, and S. A. Khan, Molecular dynamics simulation of thermodynamic and thermal transport properties of strontium titanate with improved potential parameters, *Computational Materials Science* **60**, 123–129 (2012).
- [186] R. He, H. Wu, L. Zhang, X. Wang, F. Fu, S. Liu, and Z. Zhong, Structural phase transitions in SrTiO₃ from deep potential molecular dynamics, *Physical Review B* **105**, 064104 (2022).
- [187] J. Zeng, D. Zhang, D. Lu, P. Mo, Z. Li, Y. Chen, M. Rynik, L. Huang, Z. Li, S. Shi, Y. Wang, H. Ye, P. Tuo, J. Yang, Y. Ding, Y. Li, D. Tisi, Q. Zeng, H. Bao, Y. Xia, J. Huang, K. Muraoka, Y. Wang, J. Chang, F. Yuan, S. L.

- Bore, C. Cai, Y. Lin, B. Wang, J. Xu, J.-X. Zhu, C. Luo, Y. Zhang, R. E. A. Goodall, W. Liang, A. K. Singh, S. Yao, J. Zhang, R. Wentzcovitch, J. Han, J. Liu, W. Jia, D. M. York, W. E. R. Car, L. Zhang, and H. Wang, DeePMD-kit v2: A software package for deep potential models, *The Journal of Chemical Physics* **159**, 054801 (2023).
- [188] I.-C. Lin, M. Haruta, T. Nemoto, M. Goto, Y. Shimakawa, and H. Kurata, Extraction of Anisotropic Thermal Vibration Factors for Oxygen from the Ti L_{2,3}-Edge in SrTiO₃, *The Journal of Physical Chemistry C* 10.1021/acs.jpcc.3c02035 (2023).
- [189] J. J. Sakurai and J. Napolitano, *Modern Quantum Mechanics* (Cambridge University Press, 2017).
- [190] H. Friedrich, *Scattering Theory* (Springer, Berlin, Heidelberg, 2016).
- [191] M. Born and R. Oppenheimer, Zur Quantentheorie der Molekeln, *Annalen der Physik* **389**, 457–484 (1927).
- [192] K. Sturm, Dynamic Structure Factor: An Introduction, *Zeitschrift für Naturforschung A* **48**, 10.1515/zna-1993-1-244 (1993).
- [193] L.-M. Peng and J. M. Cowley, Errors arising from numerical use of the Mott formula in electron image simulation, *Acta Crystallographica Section A* **44**, 1–6 (1988).
- [194] N. F. Mott and W. L. Bragg, The scattering of electrons by atoms, *Proceedings of the Royal Society of London. Series A, Containing Papers of a Mathematical and Physical Character* **127**, 658–665 (1930).
- [195] H. Bethe, Zur Theorie des Durchgangs schneller Korpuskularstrahlen durch Materie, *Annalen der Physik* **397**, 325–400 (1930).
- [196] J. A. Ibers, Atomic scattering amplitudes for electrons, *Acta Crystallographica* **11**, 178–183 (1958).
- [197] A. A. Maradudin, G. H. Weiss, and E. W. Montroll, *Theory of lattice dynamics in the harmonic approximation* (Academic Press, New York, 1963).

Acronyms

O	Oxygen	60
BF	Bright Field	26
BN	Boron Nitride	19
BO	Born-Oppenheimer	23
DF	Dark Field	50
FT	Fourier Transform	28
LO	Longitudinal Optical	17
MD	Molecular Dynamics	31
Sr	Strontium	60
Ti	Titanium	60
TO	Transverse Optical	17
ADF	Annular Dark Field	13
APB	Anti-Phase Boundary	53
CCD	Charge-Coupled Device	13
CMS	Conventional Multislice	36
DFE	Dynamic Form Factor	23
DFT	Density Functional Theory	39
DWF	Debye Waller Factor	28
EEL	Electron Energy Loss	13
FFT	Fast Fourier Transform	37
GLE	Generalized Langevin Equation	34
hBN	hexagonal Boron Nitride	16
IAM	Independent Atom Model	23
IAP	Interatomic Potential	39
FDT	Fluctuation Dissipation Theorem	40
MSD	Mean-Square Displacement	46
PhP	Phonon Polariton	17
POA	Phase Object Approximation	27
QEP	Quantum Excitations of Phonons	31
QHO	Quantum Harmonic Oscillator	67
SNR	Signal-to-Noise Ratio	16
STO	Strontium Titanate SrTiO_3	59
TDS	Thermal Diffuse Scattering	21
TEM	Transmission Electron Microscope/Microscopy	11
vdW	van der Waals	17
VPS	Vibrational Power Spectrum	43
ZLP	Zero-loss Peak	14

AQHO	Anisotropic Quantum Harmonic Oscillator	54
DFPT	Density Functional Perturbation Theory	24
EELS	Electron Energy Loss Spectroscopy/Spectrum	11
FPMS	Frozen Phonon Multislice	30
HERE	High Energy Resolution Electron Energy Loss Spectroscopy	16
HPhP	Hyperbolic Phonon Polariton	17
MDFF	Mixed Dynamic Formfactor	25
MLIP	Machine Learned Interatomic Potential	39
LPDOS	Local Phonon Density of States	43
PDOS	Phonon Density of States	24
RSMS	Real Space Multislice	37
STEM	Scanning Transmission Electron Microscope/Microscopy	11
WPOA	Weak Phase Object Approximation	28
DDSCS	Double Differential Scattering Cross Section	22
ELNES	Energy-Loss Near Edge Structure	30
HAADF	High Angle Annular Dark Field	13
FRFPMS	Frequency-Resolved Frozen Phonon Multislice	11

List of Natural Constants

The following natural constants are used within this dissertation:

c	Speed of light in a vacuum
e	Electron charge
h	Planck constant
\hbar	Reduced Planck constant $\hbar = \frac{h}{2\pi}$
k_B	Boltzmann constant
m_e	Electron mass
ϵ_0	Vacuum permittivity

Appendix A.

Inelastic quantum mechanical scattering theory

We consider in this appendix, how time-independent scattering theory as developed in the classic text book *Modern Quantum Mechanics* by J. J. Sakurai [189] is applied to the problem of inelastic electron scattering on a sample. The basic principle is thereby fully analogous to the treatment of inelastic scattering of an electron on an atom, but instead of a single atom, we consider a target made of a collection of atoms.

Within time-independent scattering theory, the interaction is treated as a perturbation of the (time-independent) *free* or *non-interacting* system described by a Hamiltonian \hat{H}_0 by a (time-independent) interaction \hat{H}_{inter} . Thus the total Hamiltonian of the system reads

$$\hat{H} = \hat{H}_0 + \hat{H}_{\text{inter}}. \quad (\text{A.1})$$

The experimental reality of scattering experiments is that a particle is shot at a target/sample and a detector measures the state of the particle after interaction. Thus the setup of scattering experiments requires that the system is at large distances and at times long before the interaction in an (initial) energy eigenstate $|i\rangle$ of \hat{H}_0 , meaning that the interaction \hat{H}_{inter} is sufficiently localized in space. Furthermore measurement of the state of the scattering particle happens at times long after the interaction and the system will again be subject to only \hat{H}_0 . Thus one is interested in the transition rate of an (asymptotic) initial state $|i\rangle$ scattering into an (asymptotic) final state $|f\rangle$, which are both taken to be solutions to the free-particle Schrödinger equation, i.e.,

$$\hat{H}_0 |i\rangle = E_i |i\rangle \quad (\text{A.2a})$$

$$\hat{H}_0 |f\rangle = E_f |f\rangle. \quad (\text{A.2b})$$

Note that $|i\rangle$ and $|f\rangle$ are not necessarily states of only the scattering particle, but they are in general composite (many-body) states of the scattering particle and the target. This raises the question of *distinguishability* and we assume here that the scattering particle is *distinguishable* from the target/sample. Furthermore one has in general control over the moment of

the incident particles, which are subject to only the free space Hamiltonian \hat{H}_{beam} before interaction. For these reasons, we write

$$|i\rangle = |\mathbf{k}, \Phi_i\rangle =: |\mathbf{k}\rangle \otimes |\Phi_i\rangle \quad (\text{A.3a})$$

$$\hat{H}_0 = \hat{H}_{\text{beam}} + \hat{H}_{\text{sample}} \quad (\text{A.3b})$$

where

$$\hat{H}_{\text{beam}} |\mathbf{k}\rangle = \frac{\hbar^2 \mathbf{k}^2}{2m} |\mathbf{k}\rangle =: E_{\mathbf{k}} |\mathbf{k}\rangle \quad (\text{A.4a})$$

$$\hat{H}_{\text{sample}} |\Phi_i\rangle = E_{\Phi_i} |\Phi_i\rangle. \quad (\text{A.4b})$$

Here \hat{H}_{sample} is the Hamiltonian governing the sample states $|\Phi_i\rangle$.

The DDSCS for the transition $|i\rangle \rightarrow |f\rangle$, i.e., the ratio of the incoming probability current \mathbf{j}_i to the outgoing probability current \mathbf{j}_f through a spherical surface element $\mathbf{k}' r^2 d\Omega_{\mathbf{k}'}/k'$ in direction \mathbf{k}' , can with these preliminary considerations be written in the form [189, 190]

$$\frac{d^2 \sigma_{i \rightarrow f}}{d\Omega_{\mathbf{k}'} d\Delta E} = \frac{k'}{k} |f_{i \rightarrow f}(\mathbf{k}, \mathbf{k}')|^2 \delta(E_{\Phi_f} - E_{\Phi_i} - \Delta E) \quad (\text{A.5})$$

where the energy loss reads $\Delta E = E_{\mathbf{k}'} - E_{\mathbf{k}}$ and the scattering amplitude reads

$$f_{i \rightarrow f}(\mathbf{k}, \mathbf{k}') = \frac{(2\pi)^2 m_e}{\hbar^2} \langle \mathbf{k}', \Phi_f | \hat{T} | \mathbf{k}, \Phi_i \rangle, \quad (\text{A.6})$$

which is the (in general complex) amplitude of a spherically outgoing wave $e^{ik'r}/r$ far away from the scatterer

$$\psi_{i \rightarrow f}(\mathbf{r}) \stackrel{r \rightarrow \infty}{\sim} \frac{1}{(2\pi)^{3/2}} e^{i\mathbf{k} \cdot \mathbf{r}} + f(\mathbf{k}, \mathbf{k}') \frac{e^{ik'r}}{r}, \quad (\text{A.7})$$

where $\psi_{i \rightarrow f}(\mathbf{r})$ is the scattering particle wave function associated with the transition $|i\rangle \rightarrow |f\rangle$ and the first term $e^{i\mathbf{k} \cdot \mathbf{r}}$ is the incoming wave in normalization

$$\langle \mathbf{r} | \mathbf{k} \rangle = \frac{1}{(2\pi)^{3/2}} e^{i\mathbf{k} \cdot \mathbf{r}}. \quad (\text{A.8})$$

Furthermore the so-called \hat{T} -matrix satisfies the recursive definition ¹

$$\hat{T} = \hat{H}_{\text{inter}} + \hat{H}_{\text{inter}} \frac{1}{E_i - \hat{H}_0 + i\varepsilon} \hat{T}, \quad (\text{A.9})$$

where ε is a small real quantity, whose limit needs to be taken to zero at the end of a calculation.

¹We limit ourselves here to the case of scattering from the infinite past to the infinite future ($+i\varepsilon$). One could equivalently use $-i\varepsilon$ and consider the scattering process happening from the infinite future to the infinite past.

Note that the form of the DDSCS in eq. (A.5) takes only the ratio of the scattered probability current to the incident probability current into account and totally neglects the probability current associated with the interference of the incident wave and the scattered wave [190]. Said differently, this form of the DDSCS considers only *scattered* waves, but totally neglects *unscattered* waves. As such this form of the DDSCS is not adequate for describing the number of counts detected in a scattering experiment in the forward direction $\mathbf{k} = \mathbf{k}'$ for zero energy loss $\Delta E = 0$, since the particle beam contains in this case unscattered particles.

Before we conclude this appendix, we write down some further results from time-independent scattering theory, which will prove useful to the discussion in the main text. One can define the *scattered state* $|\psi_i^{(+)}\rangle$, which satisfies ²

$$\hat{H}_{\text{inter}} |\psi_i^{(+)}\rangle = \hat{T} |i\rangle \quad (\text{A.10})$$

and also the recursive Lippmann-Schwinger equation

$$|\psi_i^{(+)}\rangle = |i\rangle + \frac{1}{E_i - \hat{H}_0 + i\varepsilon} \hat{H}_{\text{inter}} |\psi_i^{(+)}\rangle. \quad (\text{A.11})$$

The state $|\psi_i^{(+)}\rangle$ encodes the entire solution of the scattering problem and is equivalent to the initial state $|i\rangle$ in the absence of interaction ($\hat{H}_{\text{inter}} = 0$).

²Consistent with the previous footnote, we consider here only the case of $+i\varepsilon$, i.e., scattering from the infinite past to the infinite future.

Appendix B.

Inelastic electron-matter scattering

We continue in this appendix the discussion of the DDSCS associated with a transition $|i\rangle \rightarrow |f\rangle$ of appendix A. We explicitly limit ourselves here to the interaction of an electron with the full many-body system of the sample. The Hamiltonian of this combined beam electron-sample system under study can be written as

$$\hat{H} = \hat{H}_{\text{beam}} + \hat{H}_{\text{elec}} + \hat{H}_{\text{nuc}} + \hat{H}_{\text{inter}} = \hat{H}_0 + \hat{H}_{\text{inter}}, \quad (\text{B.1})$$

where

$$\hat{H}_{\text{beam}} = \frac{\hbar^2 \mathbf{k}^2}{2m} \quad (\text{B.2a})$$

$$\hat{H}_{\text{elec}} = \sum_{\lambda=1}^{N_e} \frac{\hat{\mathbf{p}}_{\lambda}^2}{2m_e} + \frac{e^2}{4\pi\epsilon_0} \left[\frac{1}{2} \sum_{\substack{\lambda, \lambda'=1 \\ \lambda \neq \lambda'}}^{N_e, N_e} \frac{1}{|\hat{\mathbf{r}}_{\lambda} - \hat{\mathbf{r}}_{\lambda'}|} - \sum_{\kappa=1}^{N_e, N} \frac{Z_{\kappa}}{|\hat{\mathbf{r}}_{\lambda} - \hat{\mathbf{R}}_{\kappa}|} \right] \quad (\text{B.2b})$$

$$\hat{H}_{\text{nuc}} = \sum_{\kappa=1}^N \frac{\hat{\mathbf{p}}_{\kappa}^2}{2m_{\kappa}} + \frac{e^2}{8\pi\epsilon_0} \sum_{\substack{\kappa, \kappa'=1 \\ \kappa \neq \kappa'}}^{N, N} \frac{Z_{\kappa}}{|\hat{\mathbf{R}}_{\kappa} - \hat{\mathbf{R}}_{\kappa'}|} + E_{\chi_0}(\{\hat{\mathbf{R}}_{\kappa}\}) \quad (\text{B.2c})$$

$$:= \sum_{\kappa=1}^N \frac{\hat{\mathbf{p}}_{\kappa}^2}{2m_{\kappa}} + E_{\text{BO}}(\{\hat{\mathbf{R}}_{\kappa}\}) \quad (\text{B.2d})$$

$$\hat{H}_{\text{inter}} = \frac{e^2}{4\pi\epsilon_0} \left[\sum_{\lambda=1}^{N_e} \frac{1}{|\hat{\mathbf{r}} - \hat{\mathbf{r}}_{\lambda}|} - \sum_{\kappa=1}^N \frac{Z_{\kappa}}{|\hat{\mathbf{r}} - \hat{\mathbf{R}}_{\kappa}|} \right] \quad (\text{B.2e})$$

are the Hamiltonian operators of the beam electron, the electronic structure of the sample, the nuclei of the sample, and the interaction between the beam and the sample, respectively. Here $\{\hat{\mathbf{R}}_{\kappa}\}$ are the N position operators of the nuclei, $\{\hat{\mathbf{r}}_{\lambda}\}$ are the N_e position operators of the electrons in the sample. We have tacitly assumed the BO approximation [191], which allows to separate the nuclear and electronic degrees of freedom, such that we have the following eigenvalue equations

$$\hat{H}_{\text{beam}} |\mathbf{k}\rangle = \frac{\hbar^2 \mathbf{k}^2}{2m} |\mathbf{k}\rangle =: E_{\mathbf{k}} |\mathbf{k}\rangle \quad (\text{B.3a})$$

$$\hat{H}_{\text{elec}} |\chi_0(\{\mathbf{R}_{\kappa}\})\rangle = E_{\chi_0}(\{\mathbf{R}_{\kappa}\}) |\chi_0(\{\mathbf{R}_{\kappa}\})\rangle \quad (\text{B.3b})$$

$$\hat{H}_{\text{nuc}} |\phi\rangle = E_{\phi} |\phi\rangle \quad (\text{B.3c})$$

for the electron beam, the electronic structure and the nuclei. The so-called BO surface $E_{\text{BO}}(\{\hat{\mathbf{R}}_{\kappa}\})$ is the potential hyper surface, on which the dynamics of the nuclei unfolds. Following appendix A, the initial state, the final state, and the energy difference between initial and final states read then

$$|i\rangle = |\mathbf{k}, \chi_0(\{\mathbf{R}_{\kappa}\}), \phi_i\rangle \equiv |\mathbf{k}'\rangle \otimes |\chi_0(\{\mathbf{R}_{\kappa}\})\rangle \otimes |\phi_i\rangle \quad (\text{B.4a})$$

$$\langle f| = \langle \mathbf{k}', \chi_0(\{\mathbf{R}_{\kappa}\}), \phi_f| \equiv \langle \mathbf{k}'| \otimes \langle \chi_0(\{\mathbf{R}_{\kappa}\})| \otimes \langle \phi_f| \quad (\text{B.4b})$$

$$E_f - E_i = E_{\mathbf{k}'} - E_{\mathbf{k}} + E_{\phi_f} - E_{\phi_i} = E_{\phi_f} - E_{\phi_i} - \Delta E, \quad (\text{B.4c})$$

since we are interested in vibrational excitations, i.e., excitations in which the beam loses energy ΔE to the nuclei of the sample. We neglect here electronic transitions and assume that the electronic structure follows the motion of nuclei adiabatically according to the BO approximation. Note that this is good approximation for insulators and semiconductors, which do not host electronic transitions at vibrational energies, but is a bad assumption for metals, in which a continuum of electronic states exists close to the Fermi-level, which gives rise to electronic transitions, which overlap with the energies of vibrational transitions.

The DDSCS for transition $|i\rangle \rightarrow |f\rangle$ becomes then for our combined system of beam electron and sample

$$\frac{d^2\sigma_{i \rightarrow f}}{d\Omega_{\mathbf{k}'} d\Delta E} = \frac{k'}{k} |f_{i \rightarrow f}(\mathbf{k}, \mathbf{k}')|^2 \delta(E_{\phi_f} - E_{\phi_i} - \Delta E) \quad (\text{B.5})$$

where the scattering amplitude reads

$$f_{i \rightarrow f}(\mathbf{k}, \mathbf{k}') = \frac{(2\pi)^2 m_e}{\hbar^2} \langle \mathbf{k}', \chi_0(\{\mathbf{R}_{\kappa}\}), \phi_f | \hat{T} | \mathbf{k}, \chi_0(\{\mathbf{R}_{\kappa}\}), \phi_i \rangle. \quad (\text{B.6})$$

We evaluate the DDSCS for transition $|i\rangle \rightarrow |f\rangle$ in appendix C.

Appendix C.

First order Born approximation

In first-order Born approximation, the T -matrix becomes simply

$$\hat{T} = \hat{H}_{\text{inter}} \quad (\text{C.1})$$

and we then need to solve for

$$f_{i \rightarrow f}(\mathbf{k}, \mathbf{k}') = \frac{(2\pi)^2 m_e}{\hbar^2} \langle \mathbf{k}', \chi_0(\{\mathbf{R}_\kappa\}), \phi_f | \hat{H}_{\text{inter}} | \mathbf{k}, \chi_0(\{\mathbf{R}_\kappa\}), \phi_i \rangle \quad (\text{C.2})$$

and the quantity of interest reads thus

$$\begin{aligned} & \langle \mathbf{k}', \chi_0(\{\mathbf{R}_\kappa\}), \phi_f | \hat{H}_{\text{inter}} | \mathbf{k}, \chi_0(\{\mathbf{R}_\kappa\}), \phi_i \rangle \\ &= \int \frac{d^3 \mathbf{r}}{(2\pi)^3} e^{-i(\mathbf{k}' - \mathbf{k}) \cdot \mathbf{r}} \langle \chi_0(\{\hat{\mathbf{R}}_\kappa\}), \phi_f | \hat{H}_{\text{inter}}(\mathbf{r}) | \chi_0(\{\hat{\mathbf{R}}_\kappa\}), \phi_i \rangle \end{aligned} \quad (\text{C.3})$$

i.e., we have the Fourier transform of a matrix element of the interaction potential. Let's consider first the matrix element

$$\begin{aligned} & \langle \chi_0(\{\hat{\mathbf{R}}_\kappa\}), \phi_f | \hat{H}_{\text{inter}}(\mathbf{r}) | \chi_0(\{\hat{\mathbf{R}}_\kappa\}), \phi_i \rangle \\ &= \frac{e^2}{4\pi\epsilon_0} \left[\sum_{\lambda=1}^{N_e} \left\langle \chi_0(\{\hat{\mathbf{R}}_\kappa\}), \phi_f \left| \frac{1}{|\mathbf{r} - \hat{\mathbf{r}}_\lambda|} \right| \chi_0(\{\hat{\mathbf{R}}_\kappa\}), \phi_i \right\rangle - \right. \\ & \quad \left. - \sum_{\kappa=1}^N \left\langle \phi_f \left| \frac{Z_\kappa}{|\mathbf{r} - \hat{\mathbf{R}}_\kappa|} \right| \phi_i \right\rangle \right], \end{aligned} \quad (\text{C.4})$$

since the operator of the nuclear positions $\hat{\mathbf{R}}_\kappa$ does not operate on the electronic state $|\chi_0(\{\hat{\mathbf{R}}_\kappa\})\rangle$. We now consider the first term:

$$\begin{aligned} & \sum_{\lambda=1}^{N_e} \left\langle \chi_0(\{\hat{\mathbf{R}}_\kappa\}), \phi_f \left| \frac{1}{|\mathbf{r} - \hat{\mathbf{r}}_\lambda|} \right| \chi_0(\{\hat{\mathbf{R}}_\kappa\}), \phi_i \right\rangle \\ &= \sum_{\lambda=1}^{N_e} \left\langle \phi_f \left| \int d^3 \mathbf{r}_1 \dots \int d^3 \mathbf{r}_{N_e} \frac{1}{|\mathbf{r} - \mathbf{r}_\lambda|} \chi_0^*(\{\mathbf{r}_\lambda\}, \{\hat{\mathbf{R}}_\kappa\}) \chi_0(\{\mathbf{r}_\lambda\}, \{\hat{\mathbf{R}}_\kappa\}) \right| \phi_i \right\rangle \\ &= \left\langle \phi_f \left| \int d^3 \tilde{\mathbf{r}} \frac{\rho_e(\tilde{\mathbf{r}}, \{\hat{\mathbf{R}}_\kappa\})}{|\mathbf{r} - \tilde{\mathbf{r}}|} \right| \phi_i \right\rangle, \end{aligned} \quad (\text{C.5})$$

where we have used the fact that the integrals over $\{\mathbf{r}_\lambda\}$ evaluate to the same value for each λ , since the electrons of the sample are indistinguishable, and that the definition of the electron density reads

$$\begin{aligned} \rho_e(\tilde{\mathbf{r}}, \{\hat{\mathbf{R}}_\kappa\}) \\ = N_e \int d^3\mathbf{r}_2 \dots \int d^3\mathbf{r}_{N_e} \chi_0^*(\tilde{\mathbf{r}}, \{\mathbf{r}_\lambda\}_{\lambda \neq 1}, \{\hat{\mathbf{R}}_\kappa\}) \chi_0(\tilde{\mathbf{r}}, \{\mathbf{r}_\lambda\}_{\lambda \neq 1}, \{\hat{\mathbf{R}}_\kappa\}). \end{aligned} \quad (\text{C.6})$$

Note that $\{\mathbf{r}_\lambda\}_{\lambda \neq 1}$ is here only a short hand notation for the set of electron coordinates for $\lambda = 2, \dots, N_e$. Thus we find

$$\begin{aligned} \langle \chi_0(\{\hat{\mathbf{R}}_\kappa\}), \phi_f | \hat{H}_{\text{inter}}(\mathbf{r}) | \chi_0(\{\hat{\mathbf{R}}_\kappa\}), \phi_i \rangle \\ = \frac{e^2}{4\pi\epsilon_0} \left\langle \phi_f \left| \left[\int d^3\tilde{\mathbf{r}} \frac{\rho_e(\tilde{\mathbf{r}}, \{\hat{\mathbf{R}}_\kappa\})}{|\mathbf{r} - \tilde{\mathbf{r}}|} - \sum_{\kappa=1}^N \frac{Z_\kappa}{|\mathbf{r} - \hat{\mathbf{R}}_\kappa|} \right] \right| \phi_i \right\rangle. \end{aligned} \quad (\text{C.7})$$

Equation (C.2) becomes then

$$\begin{aligned} f_{i \rightarrow f}(\mathbf{k}, \mathbf{k}') \\ = \frac{m_e e^2}{2(2\pi)^2 \hbar^2 \epsilon_0} \left[\left\langle \phi_f \left| \int d^3\tilde{\mathbf{r}} \int d^3\mathbf{r} e^{-i\mathbf{q} \cdot \mathbf{r}} \frac{\rho_e(\tilde{\mathbf{r}}, \{\hat{\mathbf{R}}_\kappa\})}{|\mathbf{r} - \tilde{\mathbf{r}}|} \right| \phi_i \right\rangle - \right. \\ \left. - \sum_{\kappa=1}^N \left\langle \phi_f \left| \int d^3\mathbf{r} e^{-i\mathbf{q} \cdot \mathbf{r}} \frac{Z_\kappa}{|\mathbf{r} - \hat{\mathbf{R}}_\kappa|} \right| \phi_i \right\rangle \right], \end{aligned} \quad (\text{C.8})$$

where we have defined the momentum transfer

$$\mathbf{q} = \mathbf{k}' - \mathbf{k}. \quad (\text{C.9})$$

We compute the FT of the Coulomb potential using

$$\lim_{\mu \rightarrow 0} \left[\int d^3\mathbf{r} \frac{e^{-\mu|\mathbf{r}|}}{|\mathbf{r}|} e^{-i\mathbf{q} \cdot \mathbf{r}} \right] = \frac{4\pi}{q^2}, \quad (\text{C.10})$$

where we have defined $q = |\mathbf{q}|$. We obtain

$$\begin{aligned} f_{i \rightarrow f}(\mathbf{k}, \mathbf{k}') &= \frac{m_e e^2}{2\pi \hbar^2 \epsilon_0} \frac{1}{q^2} \left[\left\langle \phi_f \left| \int d^3\mathbf{r} e^{-i\mathbf{q} \cdot \mathbf{r}} \rho_e(\mathbf{r}, \{\hat{\mathbf{R}}_\kappa\}) \right| \phi_i \right\rangle - \right. \\ &\quad \left. - \sum_{\kappa=1}^N Z_\kappa \left\langle \phi_f \left| e^{-i\mathbf{q} \cdot \hat{\mathbf{R}}_\kappa} \right| \phi_i \right\rangle \right] \\ &= \frac{m_e e^2}{2\pi \hbar^2 \epsilon_0} \frac{1}{q^2} \left\langle \phi_f \left| \left[\rho_e(\mathbf{q}, \{\hat{\mathbf{R}}_\kappa\}) - \sum_{\kappa=1}^N Z_\kappa e^{-i\mathbf{q} \cdot \hat{\mathbf{R}}_\kappa} \right] \right| \phi_i \right\rangle \\ &=: \frac{m_e e^2}{2\pi \hbar^2 \epsilon_0} \frac{1}{q^2} \langle \phi_f | \rho_{\text{tot}}(\mathbf{q}, \{\hat{\mathbf{R}}_\kappa\}) | \phi_i \rangle, \end{aligned} \quad (\text{C.11})$$

where $\rho_e(\mathbf{q}, \{\hat{\mathbf{R}}_\kappa\})$ is the spatial FT of the electronic charge density and $\rho_{\text{tot}}(\mathbf{q}, \{\hat{\mathbf{R}}_\kappa\})$ the spatial FT of the total charge density for a certain configuration of the nuclei $\hat{\mathbf{R}}_\kappa$. The cross section for transition $i \rightarrow f$ reads then

$$\frac{d^2\sigma_{i \rightarrow f}}{d\Omega_{\mathbf{q}} d\Delta E} = \frac{m_e^2 e^4}{(2\pi)^2 \hbar^4 \epsilon_0^2} \frac{k'}{k} \frac{1}{q^4} |\langle \phi_f | \rho_{\text{tot}}(\mathbf{q}, \{\hat{\mathbf{R}}_\kappa\}) | \phi_i \rangle|^2 \delta(E_{\phi_f} - E_{\phi_i} - \Delta E). \quad (\text{C.12})$$

This DDSCS is associated with a specific transition $|i\rangle \rightarrow |f\rangle$, but that does not really represent the experimental situation in most cases as we will see in appendix D.

Appendix D.

Thermal averaging of the DDSCS

We have generally no control over the final state $|f\rangle$ of the target, but all transitions, which are permitted by energy conservation and the considered scattering geometry will contribute. Thus we need to sum the DDSCS in eq. (C.12) over final states $|f\rangle$. Furthermore the crystal is in thermal equilibrium with the environment, which means that we also need to take the thermal average of eq. (C.12) over initial states i . We will consider therefore in the following

$$\begin{aligned} \frac{d^2\sigma}{d\Omega_{\mathbf{q}} d\Delta E} &= \frac{m_e^2 e^4}{(2\pi)^2 \hbar^4 \epsilon_0^2} \frac{k'}{k} \frac{1}{q^4} \times \\ &\times \sum_{\phi_i, \phi_f} \frac{e^{-\beta E_{\phi_i}}}{Z} |\langle \phi_f | \rho_{\text{tot}}(\mathbf{q}, \{\hat{\mathbf{R}}_{\kappa}\}) | \phi_i \rangle|^2 \delta(E_{\phi_f} - E_{\phi_i} - \Delta E) \end{aligned} \quad (\text{D.1})$$

where the partition function reads

$$Z = \sum_{\phi_i} e^{-\beta E_{\phi_i}}. \quad (\text{D.2})$$

Following van Hove [99], we can rewrite ³

$$\begin{aligned} &\sum_{\phi_i, \phi_f} \frac{e^{-\beta E_{\phi_i}}}{Z} |\langle \phi_f | \rho_{\text{tot}}(\mathbf{q}, \{\hat{\mathbf{R}}_{\kappa}\}) | \phi_i \rangle|^2 \delta(E_{\phi_f} - E_{\phi_i} - \Delta E) \\ &= \int \frac{dt}{2\pi\hbar} e^{-i\Delta E t/\hbar} \sum_{\phi_i, \phi_f} \frac{e^{-\beta E_{\phi_i}}}{Z} \langle \phi_i | \rho_{\text{tot}}^{\dagger} | \phi_f \rangle \langle \phi_f | \rho_{\text{tot}} | \phi_i \rangle e^{i(E_{\phi_f} - E_{\phi_i})t/\hbar} \\ &= \int \frac{dt}{2\pi\hbar} e^{-i\Delta E t/\hbar} \sum_{\phi_i, \phi_f} \frac{e^{-\beta E_{\phi_i}}}{Z} \langle \phi_i | \rho_{\text{tot}}^{\dagger} | \phi_f \rangle \langle \phi_f | e^{iE_{\phi_f} t/\hbar} \rho_{\text{tot}} e^{-iE_{\phi_i} t/\hbar} | \phi_i \rangle \\ &= \int \frac{dt}{2\pi\hbar} e^{-i\Delta E t/\hbar} \sum_{\phi_i} \frac{e^{-\beta E_{\phi_i}}}{Z} \langle \phi_i | \rho_{\text{tot}}^{\dagger} \rho_{\text{tot}}(t) | \phi_i \rangle \\ &= \int \frac{dt}{2\pi\hbar} e^{-i\Delta E t/\hbar} \langle \rho_{\text{tot}}^{\dagger}(\mathbf{q}, \{\hat{\mathbf{R}}_{\kappa}\}) \rho_{\text{tot}}(\mathbf{q}, \{\hat{\mathbf{R}}_{\kappa}(t)\}) \rangle_T, \end{aligned} \quad (\text{D.3})$$

³We suppress the argument $\mathbf{q}, \{\hat{\mathbf{R}}_{\kappa}\}$ in some lines to save space.

where we have defined the inverse temperature $\beta = (k_B T)^{-1}$, used the completeness of the basis $\sum_{\phi_f} |\phi_f\rangle \langle \phi_f| = 1$, and used that the action of the time evolution operator $\hat{U}(t, 0)$ is

$$\hat{U}(t, 0) |\phi_i\rangle = e^{-i\hat{H}_{\text{nuc}}t/\hbar} |\phi_i\rangle = e^{-iE_{\phi_i}t/\hbar} |\phi_i\rangle \quad (\text{D.4a})$$

$$\langle \phi_f | \hat{U}^\dagger(t, 0) = \langle \phi_f | e^{i\hat{H}_{\text{nuc}}t/\hbar} = \langle \phi_f | e^{iE_{\phi_f}t/\hbar} \quad (\text{D.4b})$$

$$\rho_{\text{tot}}(\mathbf{q}, \{\hat{\mathbf{R}}_\kappa(t)\}) = \hat{U}^\dagger(t, 0) \rho_{\text{tot}}(\mathbf{q}, \{\hat{\mathbf{R}}_\kappa\}) \hat{U}(t, 0) \quad (\text{D.4c})$$

Equation (D.3) is a key relation within the first order Born treatment of inelastic scattering by electrons. It relates the DDSCS to the FT of a space and time correlation function

$$S(\mathbf{r}, t) = \int \frac{d\mathbf{q}}{(2\pi)^3} e^{i\mathbf{q} \cdot \mathbf{r}} \langle \rho_{\text{tot}}^\dagger(\mathbf{q}, \{\hat{\mathbf{R}}_\kappa\}) \rho_{\text{tot}}(\mathbf{q}, \{\hat{\mathbf{R}}_\kappa(t)\}) \rangle_T. \quad (\text{D.5})$$

of the total charge density. We note that a similar expression would arise for electronic excitations, but considering different initial and final states of the electronic structure instead of the nuclei [192]. Overall we have managed to formally consider all possible final states and to thermally average the DDSCS over initial states in this section. The final DDSCS can thus be written as (c.f. Ref. [92])

$$\frac{d^2\sigma}{d\Omega_{\mathbf{q}} d\Delta E} = \frac{m_e^2 e^4}{(2\pi)^2 \hbar^4 \epsilon_0^2} \frac{k'}{k} \frac{1}{q^4} S(\mathbf{q}, \Delta E), \quad (\text{D.6})$$

where we define the DFF

$$S(\mathbf{q}, \Delta E) := \int \frac{dt}{2\pi\hbar} e^{-i\Delta E t/\hbar} \langle \rho_{\text{tot}}^\dagger(\mathbf{q}, \{\hat{\mathbf{R}}_\kappa\}) \rho_{\text{tot}}(\mathbf{q}, \{\hat{\mathbf{R}}_\kappa(t)\}) \rangle_T. \quad (\text{D.7})$$

We will limit ourselves to crystals in appendix E, but it is worthwhile to point out that we have made minimal assumptions about the sample up to this point. Furthermore we will evaluate the thermal average of the interaction in appendix G within the IAM, which we describe in appendix F.

Appendix E.

The DDSCS for a crystal

We assume now that the nuclei have periodically arranged equilibrium positions and write

$$\hat{\mathbf{R}}_{\kappa} \rightarrow \hat{\mathbf{R}}_{jl} = \hat{\mathbf{R}}_{jl}^0 + \hat{\mathbf{U}}_{jl}, \quad (\text{E.1})$$

where $\hat{\mathbf{R}}_{jl}^0$ is a vector to the equilibrium position of the j -th basis atom in the l -th unit cell of the lattice and $\hat{\mathbf{U}}_{jl}$ is the displacement from equilibrium. We furthermore assume the harmonic approximation as described in sec. 3.3, i.e., we expand the BO surface $E_{\text{BO}}(\{\hat{\mathbf{R}}_{jl}\})$ in powers of the displacement $\hat{\mathbf{U}}_{jl}$ and terminate after the harmonic term. Using the definitions in sec. 3.3, we can write the thermal average in eq. (D.7) as

$$\begin{aligned} & \langle \rho_{\text{tot}}^{\dagger}(\mathbf{q}, \{\hat{\mathbf{R}}_{jl}\}) \rho_{\text{tot}}(\mathbf{q}, \{\hat{\mathbf{R}}_{jl}(t)\}) \rangle_T \\ &= \frac{1}{Z} \sum_{\mathbf{n}} e^{-\beta E_{\mathbf{n}}} \langle \mathbf{n} | \rho_{\text{tot}}^{\dagger}(\mathbf{q}, \{\hat{\mathbf{R}}_{jl}\}) \rho_{\text{tot}}(\mathbf{q}, \{\hat{\mathbf{R}}_{jl}(t)\}) | \mathbf{n} \rangle. \end{aligned} \quad (\text{E.2})$$

Thus we need to evaluate terms of the form

$$\langle \mathbf{n} | \rho_{\text{tot}}^{\dagger}(\mathbf{q}, \{\hat{\mathbf{R}}_{jl}\}) \rho_{\text{tot}}(\mathbf{q}, \{\hat{\mathbf{R}}_{jl}(t)\}) | \mathbf{n} \rangle. \quad (\text{E.3})$$

In the crystal, the total charge density becomes

$$\rho_{\text{tot}}(\mathbf{q}, \{\hat{\mathbf{R}}_{jl}(t)\}) = \left[\rho_e(\mathbf{q}, \{\hat{\mathbf{R}}_{jl}(t)\}) - \sum_{j,l=1}^{N_{\text{uc}}, N_{\text{ba}}} Z_{jl} e^{-i\mathbf{q} \cdot \hat{\mathbf{R}}_{jl}(t)} \right]. \quad (\text{E.4})$$

The electron density $\rho_e(\mathbf{q}, \{\hat{\mathbf{R}}_{jl}(t)\})$ has without further assumptions a non-trivial dependence on the nuclear coordinates, so it is not straightforward to proceed with the evaluation from here. We introduce in appendix F the IAM in order to simplify the electron density and continue with the evaluation of the thermal average in equation (E.2) in appendix G.

Appendix F.

The Independent Atom Model

One classic approximation, the so-called Independent Atom Model (IAM), to circumvent the difficulties associated with the dependence of the electron density on the nuclear positions $\{\mathbf{R}_\kappa\}$ at the cost of neglecting details of the bonding is to assume that the electronic state $|\chi_0\rangle$ can be written as a product of electronic states of each atom, i.e.,

$$|\chi_0(\{\mathbf{R}_\kappa\})\rangle \approx \prod_{\kappa=1}^N |\chi_{0,\kappa}\rangle, \quad (\text{F.1})$$

where $|\chi_{0,\kappa}\rangle$ is the solution to the atomic problem

$$\hat{H}_{\text{elec},\kappa} |\chi_{0,\kappa}\rangle = E_{\text{elec},\kappa}^0 |\chi_{0,\kappa}\rangle. \quad (\text{F.2})$$

The atomic Hamiltonian reads here

$$\hat{H}_{\text{elec},\kappa} = \sum_{\lambda=1}^{N_{e,\kappa}} \frac{\hat{\mathbf{p}}_\lambda^2}{2m_e} + \frac{e^2}{4\pi\epsilon_0} \sum_{\lambda=1}^{N_{e,\kappa}} \frac{Z_\kappa}{|\hat{\mathbf{r}}_\lambda - \mathbf{R}_\kappa|} + \frac{e^2}{8\pi\epsilon_0} \sum_{\substack{\lambda,\lambda'=1 \\ \lambda \neq \lambda'}}^{N_{e,\kappa}, N_{e,\kappa}} \frac{1}{|\hat{\mathbf{r}}_\lambda - \hat{\mathbf{r}}_{\lambda'}|}. \quad (\text{F.3})$$

The electron density can then be written as a simple sum of the electron densities of all atoms, i.e.,

$$\rho_e(\mathbf{q}, \{\hat{\mathbf{R}}_\kappa\}) = \sum_{\kappa=1}^N e^{-i\mathbf{q} \cdot \hat{\mathbf{R}}_\kappa} \rho_{e,\kappa}(\mathbf{q}), \quad (\text{F.4})$$

where

$$\rho_{e,\kappa}(\mathbf{q}) = \int d^3\mathbf{r} e^{-i\mathbf{q} \cdot \mathbf{r}} \rho_{e,\kappa}(\mathbf{r}) =: f_{X,\kappa}(\mathbf{q}) \quad (\text{F.5})$$

is the spatial FT of the electron density

$$\rho_{e,\kappa}(\mathbf{r}) = N_{e,\kappa} \int d^3\mathbf{r}_2 \dots \int d^3\mathbf{r}_{N_{e,\kappa}} \chi_{0,\kappa}^*(\mathbf{r}, \{\mathbf{r}_\lambda\}) \chi_{0,\kappa}(\mathbf{r}, \{\mathbf{r}_\lambda\}) \quad (\text{F.6})$$

associated with the κ -th atom, also known as the atomic X-ray scattering factor $f_{X,\kappa}(\mathbf{q})$. Since a free atom is spherically symmetric, the ground state electron density satisfies

$$\rho_{e,\kappa}(\mathbf{r}) = \rho_{e,\kappa}(r) \implies f_{X,\kappa}(\mathbf{q}) = f_{X,\kappa}(q). \quad (\text{F.7})$$

We note that $\rho_{e,\kappa}(r)$ is real and even, which implies that $f_{X,\kappa}(q)$ is real and even, i.e.

$$f_{X,\kappa}^*(q) = f_{X,\kappa}(q). \quad (\text{F.8})$$

Returning to appendix D, we can write the thermal average in eq. (D.7) within the IAM as

$$\begin{aligned} & \langle \rho_{\text{tot}}^\dagger(\mathbf{q}, \{\hat{\mathbf{R}}_\kappa\}) \rho_{\text{tot}}(\mathbf{q}, \{\hat{\mathbf{R}}_\kappa(t)\}) \rangle_T \\ &= \left\langle \sum_{\kappa, \kappa'=1}^N e^{-i\mathbf{q} \cdot (\hat{\mathbf{R}}_\kappa(t) - \hat{\mathbf{R}}_{\kappa'})} [f_{X,\kappa}(q) - Z_\kappa] [f_{X,\kappa'}(q) - Z_{\kappa'}] \right\rangle_T \quad (\text{F.9}) \\ &= \frac{(2\pi)^2 \hbar^4 \epsilon_0^2}{m_e^2 e^4} q^4 \sum_{\kappa, \kappa'=1}^N f_{e,\kappa}(q) f_{e,\kappa'}(q) \langle e^{-i\mathbf{q} \cdot (\hat{\mathbf{R}}_\kappa(t) - \hat{\mathbf{R}}_{\kappa'})} \rangle_T, \end{aligned}$$

where we have used eq. (F.8) and the Mott-Bethe formula⁴ [194, 195]

$$f_{e,\kappa}(q) = \frac{m_e e^2}{2\pi \hbar^2 \epsilon_0} \left(\frac{Z_\kappa - f_{X,\kappa}(q)}{q^2} \right). \quad (\text{F.10})$$

$f_{e,\kappa}(q)$ is the so-called *electron atomic scattering factor*. Thus the DFF in equation (D.6) reads in the IAM

$$S(\mathbf{q}, \Delta E) = \frac{(2\pi)^2 \hbar^4 \epsilon_0^2}{m_e^2 e^4} q^4 \tilde{S}(\mathbf{q}, \Delta E), \quad (\text{F.11})$$

where

$$\tilde{S}(\mathbf{q}, \Delta E) := \int \frac{dt}{2\pi \hbar} e^{-i\Delta E t / \hbar} \sum_{\kappa, \kappa'=1}^N f_{e,\kappa}(q) f_{e,\kappa'}(q) \langle e^{-i\mathbf{q} \cdot (\hat{\mathbf{R}}_\kappa(t) - \hat{\mathbf{R}}_{\kappa'})} \rangle_T, \quad (\text{F.12})$$

and the DDSCS becomes simply

$$\frac{d^2 \sigma}{d\Omega_{\mathbf{q}} d\Delta E} = \frac{k'}{k} \tilde{S}(\mathbf{q}, \Delta E). \quad (\text{F.13})$$

Before concluding this appendix, we will consider as a last step the limit of $q \rightarrow 0$. For a charge neutral atom, i.e.,

$$Z_\kappa = \int_0^\infty (4\pi r^2 \rho_{e,\kappa}(r)) dr, \quad (\text{F.14})$$

⁴One should be careful when using the Mott formula to derive electron scattering factors from X-ray scattering factors for practical calculations, since numerical errors can lead to incorrect small q behavior [193].

we have [196]

$$\begin{aligned}
\lim_{q \rightarrow 0} f_{e,\kappa}(q) &= \lim_{q \rightarrow 0} \frac{m_e e^2}{2\pi \hbar^2 \epsilon_0} \left(\frac{Z_\kappa - f_{X,\kappa}(q)}{q^2} \right) \\
&= \lim_{q \rightarrow 0} \frac{m_e e^2}{2\pi \hbar^2 \epsilon_0} \left(\frac{Z_\kappa - \int_0^\infty dr e^{-iqr} (4\pi r^2 \rho_{e,\kappa}(r))}{q^2} \right) \\
&= \lim_{q \rightarrow 0} \frac{m_e e^2}{2\pi \hbar^2 \epsilon_0} \left(\frac{Z_\kappa - \int_0^\infty dr (1 - iqr - \frac{1}{2}q^2 r^2) (4\pi r^2 \rho_{e,\kappa}(r))}{q^2} \right) \\
&= \lim_{q \rightarrow 0} \frac{m_e e^2}{4\pi \hbar^2 \epsilon_0} \left(\int_0^\infty dr r^2 (4\pi r^2 \rho_{e,\kappa}(r)) \right) \\
&= \frac{m_e e^2}{\hbar^2 \epsilon_0} Z_\kappa \langle r^2 \rangle_\kappa
\end{aligned} \tag{F.15}$$

where

$$\langle r \rangle_\kappa = \frac{\int_0^\infty r (4\pi r^2 \rho_{e,\kappa}(r)) dr}{\int_0^\infty (4\pi r^2 \rho_{e,\kappa}(r)) dr} = 0 \tag{F.16}$$

and

$$\langle r^2 \rangle_\kappa = \frac{\int_0^\infty r^2 (4\pi r^2 \rho_{e,\kappa}(r)) dr}{\int_0^\infty (4\pi r^2 \rho_{e,\kappa}(r)) dr}. \tag{F.17}$$

For an ion, the electron scattering factor becomes strictly speaking divergent in the limit of $q \rightarrow 0$, since

$$Z_\kappa \neq \int_0^\infty (4\pi r^2 \rho_{e,\kappa}(r)) dr. \tag{F.18}$$

In practice numerical ionic scattering factors are not truly divergent, but one has a rather different small q behavior of the ionic electron scattering factor compared with the neutral electron scattering factor for the same nuclear charge. See also the related discussion in Refs. [74, 92]. In appendix G we will see how the thermodynamic average in equation (F.12) is evaluated within the IAM.

Appendix G.

The DDSCS of a crystal in the IAM

We start with eq. (F.12) expressed for the crystal, i.e.,

$$\tilde{S}(\mathbf{q}, \Delta E) = \int \frac{dt}{2\pi\hbar} e^{-i\Delta Et/\hbar} \sum_{j,j'=1}^N f_{e,j}(q) f_{e,j'}(q) \left\langle e^{-i\mathbf{q}\cdot(\hat{\mathbf{R}}_{jl}(t)-\hat{\mathbf{R}}_{j'l'}(0))} \right\rangle_T. \quad (\text{G.1})$$

Using relation (E.1), the thermal average becomes

$$\left\langle e^{-i\mathbf{q}\cdot[\hat{\mathbf{R}}_{jl}(t)-\hat{\mathbf{R}}_{j'l'}(0)]} \right\rangle_T = e^{-i\mathbf{q}\cdot[\hat{\mathbf{R}}_{jl}^0-\hat{\mathbf{R}}_{j'l'}^0]} \left\langle e^{-i\mathbf{q}\cdot[\hat{\mathbf{U}}_{jl}(t)-\hat{\mathbf{U}}_{j'l'}(0)]} \right\rangle_T. \quad (\text{G.2})$$

Within the harmonic approximation it can be shown that [93, 197]

$$\begin{aligned} \left\langle e^{-i\mathbf{q}\cdot[\hat{\mathbf{U}}_{jl}(t)-\hat{\mathbf{U}}_{j'l'}(0)]} \right\rangle_T &= e^{-\frac{1}{2}\langle[\mathbf{q}\cdot(\hat{\mathbf{U}}_{jl}(t)-\hat{\mathbf{U}}_{j'l'}(0))]^2\rangle_T} \\ &= e^{-\frac{1}{2}\langle(\mathbf{q}\cdot\hat{\mathbf{U}}_{jl}(t))^2\rangle_T} e^{-\frac{1}{2}\langle(\mathbf{q}\cdot\hat{\mathbf{U}}_{j'l'}(0))^2\rangle_T} \times \\ &\quad \times e^{\langle[\mathbf{q}\cdot\hat{\mathbf{U}}_{jl}(t)][\mathbf{q}\cdot\hat{\mathbf{U}}_{j'l'}(0)]\rangle_T}, \end{aligned} \quad (\text{G.3})$$

which simplifies our calculation to the computation of the three factors above. Using the conventions laid out in section 3.3, we start with realizing that

$$\begin{aligned} \langle(\mathbf{q}\cdot\hat{\mathbf{U}}_{jl}(t))^2\rangle_T &= \left\langle \sum_{\alpha\beta} q_\alpha q_\beta \hat{U}_{\alpha jl}^\dagger(t) \hat{U}_{\beta jl}(t) \right\rangle_T \\ &= \frac{\hbar}{2N_{\text{uc}}m_j} \sum_{\alpha\beta} q_\alpha q_\beta \sum_{\substack{\mathbf{k}_0, \mathbf{k}'_0 \\ \nu, \nu'}} \left[e^{i(\mathbf{k}_0-\mathbf{k}'_0)\cdot\mathbf{R}_{jl}^0} \epsilon_{\alpha j \mathbf{k}_0 \nu}^* \epsilon_{\beta j \mathbf{k}'_0 \nu'} \times \right. \\ &\quad \left. \times \langle \hat{u}_{\mathbf{k}_0 \nu}^\dagger(t) \hat{u}_{\mathbf{k}'_0 \nu'}(t) \rangle_T \right], \end{aligned} \quad (\text{G.4})$$

where we have used that only the mode displacement operators act on Fock states $|\mathbf{n}\rangle$ inside the thermal average. We will see that the average is actually

time-independent in the following, but let's first boil the expressions a bit further down and write

$$\begin{aligned} \langle \hat{u}_{\mathbf{k}_0\nu}^\dagger(t) \hat{u}_{\mathbf{k}'_0\nu'}(t) \rangle_T &= \frac{1}{\sqrt{\omega_{\mathbf{k}_0\nu} \omega_{\mathbf{k}'_0\nu'}}} \left\langle \left[\hat{a}_{\mathbf{k}_0\nu} e^{-i\omega_{\mathbf{k}_0\nu}t} + \hat{a}_{-\mathbf{k}_0\nu}^\dagger e^{i\omega_{\mathbf{k}_0\nu}t} \right]^* \times \right. \\ &\quad \left. \times \left[\hat{a}_{\mathbf{k}'_0\nu'} e^{-i\omega_{\mathbf{k}'_0\nu'}t} + \hat{a}_{-\mathbf{k}'_0\nu'}^\dagger e^{i\omega_{\mathbf{k}'_0\nu'}t} \right] \right\rangle_T. \quad (\text{G.5}) \end{aligned}$$

We thus see that we need to evaluate the expression

$$\begin{aligned} &\left\langle \left[\hat{a}_{\mathbf{k}_0\nu}^\dagger e^{i\omega_{\mathbf{k}_0\nu}t} + \hat{a}_{-\mathbf{k}_0\nu} e^{-i\omega_{\mathbf{k}_0\nu}t} \right] \left[\hat{a}_{\mathbf{k}'_0\nu'} e^{-i\omega_{\mathbf{k}'_0\nu'}t} + \hat{a}_{-\mathbf{k}'_0\nu'}^\dagger e^{i\omega_{\mathbf{k}'_0\nu'}t} \right] \right\rangle_T \\ &= \sum_{\mathbf{n}} \frac{e^{-\beta E_{\mathbf{n}}}}{Z} \langle \mathbf{n} | \left[\hat{a}_{\mathbf{k}_0\nu}^\dagger \hat{a}_{\mathbf{k}'_0\nu'} e^{i(\omega_{\mathbf{k}_0\nu} - \omega_{\mathbf{k}'_0\nu'})t} + \right. \\ &\quad \left. + \hat{a}_{-\mathbf{k}_0\nu} \hat{a}_{-\mathbf{k}'_0\nu'}^\dagger e^{-i(\omega_{\mathbf{k}_0\nu} - \omega_{\mathbf{k}'_0\nu'})t} \right] | \mathbf{n} \rangle \\ &= \delta_{\mathbf{k}_0\mathbf{k}'_0} \delta_{\nu\nu'} \sum_{\mathbf{n}} \frac{e^{-\beta E_{\mathbf{n}}}}{Z} \left[n_{\mathbf{k}_0\nu} e^{i(\omega_{\mathbf{k}_0\nu} - \omega_{\mathbf{k}'_0\nu'})t} + \right. \\ &\quad \left. + (n_{-\mathbf{k}_0\nu} + 1) e^{-i(\omega_{\mathbf{k}_0\nu} - \omega_{\mathbf{k}'_0\nu'})t} \right], \quad (\text{G.6}) \end{aligned}$$

where we have neglected terms of two phonon creation or annihilation operators, since their contribution would vanish between states $\langle \mathbf{n} | \dots | \mathbf{n} \rangle$. We have furthermore used eq. (3.39) to obtain the phonon occupation numbers. The sum $\sum_{\mathbf{n}}$ runs over all possible occupation numbers, particularly all possible values of $n_{\mathbf{k}_0\nu}$ and $n_{-\mathbf{k}_0\nu}$. Thus we can write the average of the phonon mode displacements as

$$\begin{aligned} &\langle \hat{u}_{\mathbf{k}_0\nu}^\dagger(t) \hat{u}_{\mathbf{k}'_0\nu'}(t) \rangle_T \\ &= \frac{\delta_{\mathbf{k}_0\mathbf{k}'_0} \delta_{\nu\nu'}}{\sqrt{\omega_{\mathbf{k}_0\nu} \omega_{\mathbf{k}'_0\nu'}}} \left[\langle n_{\mathbf{k}_0\nu} \rangle_T e^{i(\omega_{\mathbf{k}_0\nu} - \omega_{\mathbf{k}'_0\nu'})t} + \right. \\ &\quad \left. + (\langle n_{\mathbf{k}_0\nu} \rangle_T + 1) e^{-i(\omega_{\mathbf{k}_0\nu} - \omega_{\mathbf{k}'_0\nu'})t} \right], \quad (\text{G.7}) \end{aligned}$$

where we have used that $n_{\mathbf{k}_0\nu} = n_{-\mathbf{k}_0\nu}$, which follows from eq. (3.45). We then find

$$\begin{aligned} \langle (\mathbf{q} \cdot \hat{\mathbf{U}}_{jl}(t))^2 \rangle_T &= \frac{\hbar}{2N_{\text{uc}} m_j} \sum_{\alpha\beta} q_\alpha q_\beta \sum_{\mathbf{k}_0,\nu} \left[\epsilon_{\alpha j \mathbf{k}_0\nu}^* \epsilon_{\beta j \mathbf{k}_0\nu} \frac{2\langle n_{\mathbf{k}_0\nu} \rangle_T + 1}{\omega_{\mathbf{k}_0\nu}} \right] \\ &= \frac{\hbar}{2N_{\text{uc}} m_j} \sum_{\mathbf{k}_0,\nu} \left[\frac{2\langle n_{\mathbf{k}_0\nu} \rangle_T + 1}{\omega_{\mathbf{k}_0\nu}} |\mathbf{q} \cdot \boldsymbol{\epsilon}_{j \mathbf{k}_0\nu}|^2 \right], \quad (\text{G.8}) \end{aligned}$$

which is independent of l and independent of time, implying

$$\langle (\mathbf{q} \cdot \hat{\mathbf{U}}_{jl}(t))^2 \rangle_T \equiv \langle (\mathbf{q} \cdot \hat{\mathbf{U}}_{j1}(0))^2 \rangle_T =: 2W_j(\mathbf{q}, T). \quad (\text{G.9})$$

Here we have defined the exponent $W_j(\mathbf{q}, T)$ of the DWF $e^{-2W_j(\mathbf{q}, T)}$ of the j -th basis atom.

It is enlightening to recognize the resemblance between eqs. (G.8) and (3.50). Returning to eq. (G.3), we are left with computing the average

$$\begin{aligned} & \langle [\mathbf{q} \cdot \hat{\mathbf{U}}_{jl}(t)] [\mathbf{q} \cdot \hat{\mathbf{U}}_{j'l'}(0)] \rangle_T \\ &= \left\langle \sum_{\alpha\beta} q_\alpha q_\beta \hat{U}_{\alpha jl}(t) \hat{U}_{\beta j'l'}(0) \right\rangle_T \\ &= \frac{\hbar}{2N_{\text{uc}}} \sum_{\alpha\beta} q_\alpha q_\beta \sum_{\mathbf{k}_0, \mathbf{k}'_0} \left[e^{i(\mathbf{k}_0 \cdot \mathbf{R}_{jl}^0 + \mathbf{k}'_0 \cdot \mathbf{R}_{j'l'}^0)} \frac{\epsilon_{\alpha j \mathbf{k}_0 \nu} \epsilon_{\beta j' \mathbf{k}'_0 \nu'}}{\sqrt{m_j m_{j'}}} \times \right. \\ & \quad \left. \times \langle \hat{u}_{\mathbf{k}_0 \nu}(t) \hat{u}_{\mathbf{k}'_0 \nu'}(0) \rangle_T \right] \end{aligned} \quad (\text{G.10})$$

and analogously to the previous calculation, we need to evaluate

$$\begin{aligned} & \left\langle \left[\hat{a}_{\mathbf{k}_0 \nu} e^{-i\omega_{\mathbf{k}_0 \nu} t} + \hat{a}_{-\mathbf{k}_0 \nu}^\dagger e^{i\omega_{\mathbf{k}_0 \nu} t} \right] \left[\hat{a}_{\mathbf{k}'_0 \nu'} + \hat{a}_{-\mathbf{k}'_0 \nu'}^\dagger \right] \right\rangle_T \\ &= \sum_{\mathbf{n}} \frac{e^{-\beta E_{\mathbf{n}}}}{Z} \langle \mathbf{n} | \left[\hat{a}_{\mathbf{k}_0 \nu} \hat{a}_{-\mathbf{k}'_0 \nu'}^\dagger e^{-i\omega_{\mathbf{k}_0 \nu} t} + \right. \\ & \quad \left. + \hat{a}_{-\mathbf{k}_0 \nu}^\dagger \hat{a}_{\mathbf{k}'_0 \nu'} e^{i\omega_{\mathbf{k}_0 \nu} t} \right] | \mathbf{n} \rangle \\ &= \delta_{\mathbf{k}_0, -\mathbf{k}'_0} \delta_{\nu \nu'} \sum_{\mathbf{n}} \frac{e^{-\beta E_{\mathbf{n}}}}{Z} \left[n_{\mathbf{k}_0 \nu} e^{i\omega_{\mathbf{k}_0 \nu} t} + \right. \\ & \quad \left. + (n_{\mathbf{k}_0 \nu} + 1) e^{-i\omega_{\mathbf{k}_0 \nu} t} \right] \\ &= \delta_{\mathbf{k}_0, -\mathbf{k}'_0} \delta_{\nu \nu'} \left[\langle n_{\mathbf{k}_0 \nu} \rangle_T e^{i\omega_{\mathbf{k}_0 \nu} t} + \right. \\ & \quad \left. + (\langle n_{\mathbf{k}_0 \nu} \rangle_T + 1) e^{-i\omega_{\mathbf{k}_0 \nu} t} \right], \end{aligned} \quad (\text{G.11})$$

which allows us to obtain the result

$$\begin{aligned}
& \langle [\mathbf{q} \cdot \hat{\mathbf{U}}_{jl}(t)] [\mathbf{q} \cdot \hat{\mathbf{U}}_{j'l'}(0)] \rangle_T \\
&= \frac{\hbar}{2N_{\text{uc}}} \sum_{\alpha\beta} q_\alpha q_\beta \sum_{\mathbf{k}_0, \mathbf{k}'_0} \left[e^{i(\mathbf{k}_0 \cdot \mathbf{R}_{jl}^0 + \mathbf{k}'_0 \cdot \mathbf{R}_{j'l'}^0)} \frac{\epsilon_{\alpha j \mathbf{k}_0 \nu}}{\sqrt{m_j m_{j'}}} \frac{\epsilon_{\beta j' \mathbf{k}'_0 \nu'}}{\sqrt{\omega_{\mathbf{k}_0 \nu} \omega_{\mathbf{k}'_0 \nu'}}} \frac{\delta_{\mathbf{k}_0, -\mathbf{k}'_0} \delta_{\nu \nu'}}{\sqrt{\omega_{\mathbf{k}_0 \nu} \omega_{\mathbf{k}'_0 \nu'}}} \times \right. \\
&\quad \left. \times \left[\langle n_{\mathbf{k}_0 \nu} \rangle_T e^{i\omega_{\mathbf{k}_0 \nu} t} + (\langle n_{\mathbf{k}_0 \nu} \rangle_T + 1) e^{-i\omega_{\mathbf{k}_0 \nu} t} \right] \right] \\
&= \frac{\hbar}{2N_{\text{uc}}} \sum_{\alpha\beta} q_\alpha q_\beta \sum_{\mathbf{k}_0, \nu} \left[e^{i\mathbf{k}_0 \cdot (\mathbf{R}_{jl}^0 - \mathbf{R}_{j'l'}^0)} \frac{\epsilon_{\alpha j \mathbf{k}_0 \nu}}{\sqrt{m_j m_{j'}}} \frac{\epsilon_{\beta j' -\mathbf{k}_0 \nu}}{\omega_{\mathbf{k}_0 \nu}} \frac{1}{\omega_{\mathbf{k}_0 \nu}} \times \right. \\
&\quad \left. \times \left[\langle n_{\mathbf{k}_0 \nu} \rangle_T e^{i\omega_{\mathbf{k}_0 \nu} t} + (\langle n_{\mathbf{k}_0 \nu} \rangle_T + 1) e^{-i\omega_{\mathbf{k}_0 \nu} t} \right] \right] \\
&= \frac{\hbar}{2N_{\text{uc}}} \sum_{\mathbf{k}_0, \nu} \left[e^{i\mathbf{k}_0 \cdot (\mathbf{R}_{jl}^0 - \mathbf{R}_{j'l'}^0)} \frac{(\mathbf{q} \cdot \boldsymbol{\epsilon}_{j \mathbf{k}_0 \nu})(\mathbf{q} \cdot \boldsymbol{\epsilon}_{j' \mathbf{k}_0 \nu}^*)}{\sqrt{m_j m_{j'}}} \frac{1}{\omega_{\mathbf{k}_0 \nu}} \times \right. \\
&\quad \left. \times \left[\langle n_{\mathbf{k}_0 \nu} \rangle_T e^{i\omega_{\mathbf{k}_0 \nu} t} + (\langle n_{\mathbf{k}_0 \nu} \rangle_T + 1) e^{-i\omega_{\mathbf{k}_0 \nu} t} \right] \right], \quad (\text{G.12})
\end{aligned}$$

where we have used that $\epsilon_{\beta j - \mathbf{k}_0 \nu} = \epsilon_{\beta j \mathbf{k}_0 \nu}^*$. Overall we find that the thermal average of the exponential operator in eq. (G.1) reads

$$\begin{aligned}
& \left\langle e^{-i\mathbf{q} \cdot [\hat{\mathbf{R}}_{jl}(t) - \hat{\mathbf{R}}_{j'l'}(0)]} \right\rangle_T \\
&= \sum_{\substack{j, j'=1 \\ l, l'=1}}^{N_{\text{ba}}, N_{\text{uc}}} f_{ej}(q) f_{e, j'}(q) e^{-i\mathbf{q} \cdot [\mathbf{R}_{jl}^0 - \mathbf{R}_{j'l'}^0]} e^{-W_j(\mathbf{q}, T)} e^{-W_{j'}(\mathbf{q}, T)} \times \\
&\quad \times e^{\frac{\hbar}{2N_{\text{uc}}} \sum_{\mathbf{k}_0, \nu} e^{i(\mathbf{k}_0 \cdot \mathbf{R}_{jl}^0 - \mathbf{k}_0 \cdot \mathbf{R}_{j'l'}^0)} \frac{(\mathbf{q} \cdot \boldsymbol{\epsilon}_{j \mathbf{k}_0 \nu})(\mathbf{q} \cdot \boldsymbol{\epsilon}_{j' \mathbf{k}_0 \nu}^*)}{\sqrt{m_j m_{j'}}} \frac{\langle n_{\mathbf{k}_0 \nu} \rangle_T}{\omega_{\mathbf{k}_0 \nu}} e^{i\omega_{\mathbf{k}_0 \nu} t}} \quad (\text{G.13}) \\
&\quad \times e^{\frac{\hbar}{2N_{\text{uc}}} \sum_{\mathbf{k}_0, \nu} e^{i(\mathbf{k}_0 \cdot \mathbf{R}_{jl}^0 - \mathbf{k}_0 \cdot \mathbf{R}_{j'l'}^0)} \frac{(\mathbf{q} \cdot \boldsymbol{\epsilon}_{j \mathbf{k}_0 \nu})(\mathbf{q} \cdot \boldsymbol{\epsilon}_{j' \mathbf{k}_0 \nu}^*)}{\sqrt{m_j m_{j'}}} \frac{\langle n_{\mathbf{k}_0 \nu} \rangle_T + 1}{\omega_{\mathbf{k}_0 \nu}} e^{-i\omega_{\mathbf{k}_0 \nu} t}}.
\end{aligned}$$

Note that this expression is correct to all orders in phonon scattering within the Born approximation. We will consider in the following an expansion

of the exponentials. To that end we write

$$\tilde{S}(\mathbf{q}, \Delta E) = \int \frac{dt}{2\pi\hbar} e^{-i\Delta Et/\hbar} \sum_{\eta} \tilde{S}^{(\eta)}(\mathbf{q}, t), \quad (\text{G.14})$$

where

$$\begin{aligned} \tilde{S}^{(\eta)}(\mathbf{q}, t) &= \frac{\hbar\eta}{2\eta N_{\text{uc}}^{\eta} \eta!} \sum_{\substack{j,j'=1 \\ l,l'=1}}^{N_{\text{ba}}, N_{\text{uc}}} f_{ej}(q) f_{ej'}(q) e^{-i\mathbf{q} \cdot [\mathbf{R}_{jl}^0 - \mathbf{R}_{j'l'}^0]} \times \\ &\times e^{-W_j(\mathbf{q}, T)} e^{-W_{j'}(\mathbf{q}, T)} \times \\ &\times \left\{ \sum_{\mathbf{k}_0, \nu} e^{i(\mathbf{k}_0 \cdot \mathbf{R}_{jl}^0 - \mathbf{k}_0 \cdot \mathbf{R}_{j'l'}^0)} \frac{(\mathbf{q} \cdot \boldsymbol{\epsilon}_{j\mathbf{k}_0\nu})(\mathbf{q} \cdot \boldsymbol{\epsilon}_{j'\mathbf{k}_0\nu}^*)}{\sqrt{m_j m_{j'}}} \times \right. \\ &\times \left. \left[\frac{\langle n_{\mathbf{k}_0\nu} \rangle_T}{\omega_{\mathbf{k}_0\nu}} e^{i\omega_{\mathbf{k}_0\nu} t} + \frac{\langle n_{\mathbf{k}_0\nu} \rangle_T + 1}{\omega_{\mathbf{k}_0\nu}} e^{-i\omega_{\mathbf{k}_0\nu} t} \right] \right\}^{\eta}. \end{aligned} \quad (\text{G.15})$$

We consider the zero-th order

$$\begin{aligned} \tilde{S}^{(0)}(\mathbf{q}, t) &= \sum_{\substack{j,j'=1 \\ l,l'=1}}^{N_{\text{ba}}, N_{\text{uc}}} f_{ej}(q) f_{ej'}(q) e^{-i\mathbf{q} \cdot [\mathbf{R}_{jl}^0 - \mathbf{R}_{j'l'}^0]} e^{-W_j(\mathbf{q}, T)} e^{-W_{j'}(\mathbf{q}, T)} \\ &= \left| \sum_{j,l=1}^{N_{\text{ba}}, N_{\text{uc}}} f_{ej}(q) e^{-i\mathbf{q} \cdot \hat{\mathbf{R}}_{jl}^0} e^{-W_j(\mathbf{q}, T)} \right|^2. \end{aligned} \quad (\text{G.16})$$

The sum over the lattice positions l can then be evaluated according to

$$\sum_l e^{-i\mathbf{q} \cdot \mathbf{R}_{jl}^0} = e^{-i\mathbf{q} \cdot \mathbf{R}_j^0} \sum_l e^{-i\mathbf{q} \cdot \mathbf{R}_l^0} = N_{\text{uc}} \sum_{\mathbf{G}} e^{-i\mathbf{G} \cdot \mathbf{R}_j^0} \delta_{\mathbf{q}, \mathbf{G}}, \quad (\text{G.17})$$

where $\delta_{\mathbf{q}, \mathbf{G}}$ is the Kronecker- δ and \mathbf{q} is not restricted to the first Brillouin zone, i.e.,

$$\mathbf{q} = \tilde{\mathbf{G}} + \mathbf{q}_0. \quad (\text{G.18})$$

Here $\tilde{\mathbf{G}}$ is a reciprocal lattice vector and \mathbf{q}_0 is a vector in the first Brillouin zone. We then see that the zero-th order is only non-zero at momentum

transfers corresponding to a reciprocal lattice vector:

$$\begin{aligned}\tilde{S}^{(0)}(\mathbf{q}, t) &= N_{\text{uc}}^2 \left| \sum_{j=1}^{N_{\text{ba}}} \sum_{\mathbf{G}} e^{-i\mathbf{G} \cdot \mathbf{R}_j^0} \delta_{\mathbf{q}, \mathbf{G}} f_{ej}(q) e^{-W_j(\mathbf{q}, T)} \right|^2 \\ &= N_{\text{uc}}^2 \sum_{\mathbf{G}} \delta_{\mathbf{q}, \mathbf{G}} \left| \sum_{j=1}^{N_{\text{ba}}} e^{-i\mathbf{G} \cdot \mathbf{R}_j^0} f_{ej}(G) e^{-W_j(\mathbf{G}, T)} \right|^2.\end{aligned}\quad (\text{G.19})$$

The corresponding zero-th order scattering cross section reads then according to eqs. (F.13) and (G.14) ⁵

$$\frac{d^2\sigma^{(0)}}{d\Omega_{\mathbf{q}} d\Delta E} = N_{\text{uc}}^2 \sum_{\mathbf{G}} \delta_{\mathbf{q}, \mathbf{G}} \left| \sum_{j=1}^{N_{\text{ba}}} e^{-i\mathbf{G} \cdot \mathbf{R}_j^0} f_{ej}(G) e^{-W_j(\mathbf{G}, T)} \right|^2 \delta(\Delta E). \quad (\text{G.20})$$

We realize that the zero-th order corresponds to elastic scattering on the target, since no energy-loss or -gain is associated with it.

As the last consideration for this appendix, we consider the first order of the expansion, i.e.,

$$\begin{aligned}\tilde{S}^{(1)}(\mathbf{q}, t) &= \frac{\hbar}{2N_{\text{uc}}} \sum_{\mathbf{k}_0, \nu} \left[\frac{\langle n_{\mathbf{k}_0 \nu} \rangle_T}{\omega_{\mathbf{k}_0 \nu}} e^{i\omega_{\mathbf{k}_0 \nu} t} + \frac{\langle n_{\mathbf{k}_0 \nu} \rangle_T + 1}{\omega_{\mathbf{k}_0 \nu}} e^{-i\omega_{\mathbf{k}_0 \nu} t} \right] \times \\ &\quad \times \left| \sum_{j,l=1}^{N_{\text{ba}}, N_{\text{uc}}} e^{-i(\mathbf{q}-\mathbf{k}_0) \cdot \mathbf{R}_{jl}^0} f_{ej}(q) e^{-W_j(\mathbf{q}, T)} \frac{(\mathbf{q} \cdot \boldsymbol{\epsilon}_{j\mathbf{k}_0 \nu})}{\sqrt{m_j}} \right|^2.\end{aligned}\quad (\text{G.21})$$

Using eq. (G.17), we can again carry out the lattice sums and obtain

$$\begin{aligned}\tilde{S}^{(1)}(\mathbf{q}, t) &= \frac{\hbar N_{\text{uc}}}{2} \sum_{\mathbf{k}_0, \nu} \left[\frac{\langle n_{\mathbf{k}_0 \nu} \rangle_T}{\omega_{\mathbf{k}_0 \nu}} e^{i\omega_{\mathbf{k}_0 \nu} t} + \frac{\langle n_{\mathbf{k}_0 \nu} \rangle_T + 1}{\omega_{\mathbf{k}_0 \nu}} e^{-i\omega_{\mathbf{k}_0 \nu} t} \right] \times \\ &\quad \times \left| \sum_{j=1}^{N_{\text{ba}}} \sum_{\mathbf{G}} e^{-i\mathbf{G} \cdot \mathbf{R}_j^0} \delta_{\mathbf{q}-\mathbf{k}_0, \mathbf{G}} f_{ej}(q) e^{-W_j(\mathbf{q}, T)} \frac{(\mathbf{q} \cdot \boldsymbol{\epsilon}_{j\mathbf{k}_0 \nu})}{\sqrt{m_j}} \right|^2,\end{aligned}$$

which can be rewritten as

$$\begin{aligned}\tilde{S}^{(1)}(\mathbf{q}, t) &= \frac{\hbar N_{\text{uc}}}{2} \sum_{\mathbf{G}, \nu} \delta_{\mathbf{q}-\mathbf{q}_0, \mathbf{G}} \left| \sum_{j=1}^{N_{\text{ba}}} e^{-i\mathbf{G} \cdot \mathbf{R}_j^0} f_{ej}(q) e^{-W_j(\mathbf{q}, T)} \frac{(\mathbf{q} \cdot \boldsymbol{\epsilon}_{j\mathbf{q}_0 \nu})}{\sqrt{m_j}} \right|^2 \times \\ &\quad \times \left[\frac{\langle n_{\mathbf{q}_0 \nu} \rangle_T}{\omega_{\mathbf{q}_0 \nu}} e^{i\omega_{\mathbf{q}_0 \nu} t} + \frac{\langle n_{\mathbf{q}_0 \nu} \rangle_T + 1}{\omega_{\mathbf{q}_0 \nu}} e^{-i\omega_{\mathbf{q}_0 \nu} t} \right],\end{aligned}\quad (\text{G.22})$$

⁵Note here that $\Delta E = 0$ and thus $k' = k$.

since only one unique decomposition of \mathbf{q} of the form of eq. (G.18) exists and the Kronecker- δ $\delta_{\mathbf{q}-\mathbf{k}_0, \mathbf{G}}$ forces $\mathbf{q}_0 = \mathbf{k}_0$. The corresponding first order DDSCS reads then according to eqs. (F.13) and (G.14)

$$\begin{aligned} \frac{d^2\sigma^{(1)}}{d\Omega_{\mathbf{q}} d\Delta E} &= \frac{\hbar N_{\text{uc}}}{2} \frac{k'}{k} \sum_{\mathbf{G}, \nu} \delta_{\mathbf{q}-\mathbf{q}_0, \mathbf{G}} \left| \sum_{j=1}^{N_{\text{ba}}} e^{-i\mathbf{G} \cdot \mathbf{R}_j^0} f_{ej}(q) e^{-W_j(\mathbf{q}, T)} \frac{(\mathbf{q} \cdot \boldsymbol{\epsilon}_{j\mathbf{q}_0\nu})}{\sqrt{m_j}} \right|^2 \times \\ &\times \left[\frac{\langle n_{\mathbf{q}_0\nu} \rangle_T + 1}{\omega_{\mathbf{q}_0\nu}} \delta(\hbar\omega_{\mathbf{q}_0\nu} - \Delta E) + \frac{\langle n_{\mathbf{q}_0\nu} \rangle_T}{\omega_{\mathbf{q}_0\nu}} \delta(\hbar\omega_{\mathbf{q}_0\nu} + \Delta E) \right]. \end{aligned} \quad (\text{G.23})$$

This expression makes it clear, that the first-order DDSCS corresponds to single phonon excitations, in which a single quantum of energy $\hbar\omega_{\mathbf{q}_0\nu}$ is gained or lost. Furthermore the momentum also needs to be conserved up to the *crystal momentum* \mathbf{G} as we have the requirement, that

$$\mathbf{q} - \mathbf{q}_0 = \mathbf{G}. \quad (\text{G.24})$$

Appendix H.

Momentum transfer in z-direction

The momentum transfer is defined as

$$\mathbf{q} = \mathbf{k}' - \mathbf{k}, \quad (\text{H.1})$$

where \mathbf{k} is the initial and \mathbf{k}' final wave vector of the electron. We take $\mathbf{k} \parallel \hat{\mathbf{z}}$ and write then

$$\mathbf{q} = (\mathbf{q}_\perp, q_z) = (\mathbf{k}'_\perp, k'_z - k), \quad (\text{H.2})$$

where we have separated out the component in the plane orthogonal to the incident wave vector in all vectors. Furthermore the scattering angle θ is defined via the relation

$$\cos(\theta) = \frac{\mathbf{k}' \cdot \mathbf{k}}{k'k} = \frac{k'_z}{k'}. \quad (\text{H.3})$$

and

$$\frac{k'}{k} = \sqrt{\frac{E_k - \Delta E}{E_k}}, \quad (\text{H.4})$$

where we have written the initial and final energies of the electron as

$$E_k = \frac{\hbar^2 k^2}{2m_e} \quad (\text{H.5a})$$

$$E_{k'} = \frac{\hbar^2 k'^2}{2m_e} = E_k - \Delta E \quad (\text{H.5b})$$

and defined the energy loss ΔE . Using these relations, we can work out the ratio of the absolute value of the z component to the absolute value of the in-plane component of the momentum transfer depending on the scattering angle θ

$$\frac{|\mathbf{q}_\perp|}{|q_z|} = \frac{|\sin(\theta)|}{\left| \cos(\theta) - \sqrt{\frac{E_k}{E_k - \Delta E}} \right|}. \quad (\text{H.6})$$

We plot this expression in Fig. 2.1 for an initial kinetic energy of 60 keV, and a large range of energy losses and scattering angles.

Appendix I.

Derivation of MSD in classical statistical mechanics

We note first the integrals

$$\int_{-\infty}^{\infty} \exp(-ax^2) dx = \frac{\sqrt{\pi}}{\sqrt{a}} \quad (\text{I.1})$$

and

$$\int_{-\infty}^{\infty} x^2 \exp(-ax^2) dx = \frac{\sqrt{\pi}}{2a^{3/2}} \quad (\text{I.2})$$

for $a > 0$. We then consider a classical 2D anisotropic harmonic oscillator with Hamiltonian

$$H(p_x, p_y, x, y) = \frac{p_x^2}{2M} + \frac{p_y^2}{2M} + \frac{M\omega_x^2 u_x^2}{2} + \frac{M\omega_y^2 u_y^2}{2} \quad (\text{I.3})$$

and we define the displacement $\mathbf{u}_{\perp} = (u_x, u_y)$. The classical partition function reads

$$\begin{aligned} Z &= \frac{1}{h^4} \int dp_x dp_y du_x du_y e^{-\beta H(p_x, p_y, u_x, u_y)} \\ &= \frac{1}{h^4} \left[\int dp_x e^{-\beta \frac{p_x^2}{2m}} \right] \left[\int dp_y e^{-\beta \frac{p_y^2}{2M}} \right] \times \\ &\quad \times \left[\int du_x e^{-\beta \frac{M\omega_x^2 u_x^2}{2}} \right] \left[\int du_y e^{-\beta \frac{M\omega_y^2 u_y^2}{2}} \right] \\ &= \frac{1}{h^4} \left[\frac{\sqrt{\pi} \sqrt{2M}}{\sqrt{\beta}} \right]^2 \left[\frac{\sqrt{2\pi}}{\sqrt{\beta} \sqrt{M\omega_x}} \right] \left[\frac{\sqrt{2\pi}}{\sqrt{\beta} \sqrt{M\omega_y}} \right] \\ &= \frac{1}{h^4} \left[\frac{2\pi}{\beta \omega_x} \right] \left[\frac{2\pi}{\beta \omega_y} \right], \end{aligned} \quad (\text{I.4})$$

where $\beta = 1/(k_B T)$ and h is the conventional normalization constant of classical statistical mechanics. We want to compute the MSD $\langle \mathbf{u}_{\perp}^2 \rangle_T$ in the

following and start with

$$\begin{aligned}
\langle \mathbf{u}_\perp \rangle_T &= \frac{1}{h^4} \int dp_x dp_y du_x du_y (u_x^2 + u_y^2) e^{-\beta H(p_x, p_y, u_x, u_y)} \\
&= \frac{1}{h^4} \int dp_x dp_y du_x du_y u_x^2 e^{-\beta H(p_x, p_y, u_x, u_y)} + \\
&\quad + \frac{1}{h^4} \int dp_x dp_y du_x du_y u_y^2 e^{-\beta H(p_x, p_y, u_x, u_y)} \\
&= \langle u_x^2 \rangle_T + \langle u_y^2 \rangle_T,
\end{aligned} \tag{I.5}$$

where we recognize that both quadruple integrals are essentially the same up to the name of the letter of the component of the displacement, so it suffices to compute the expectation value for a single displacement direction, i.e.,

$$\begin{aligned}
\langle u_x^2 \rangle_T &= \frac{1}{Z} \frac{1}{h^4} \int dp_x dp_y du_x du_y u_x^2 e^{-\beta H(p_x, p_y, u_x, u_y)} \\
&= \frac{1}{Z} \frac{1}{h^4} \underbrace{\left[\int dp_x e^{-\beta \frac{p_x^2}{2M}} \right] \left[\int dp_y e^{-\beta \frac{p_y^2}{2M}} \right]}_{\text{prod. of 2 integrals of form of eq. (I.1)}} \times \\
&\quad \times \underbrace{\left[\int du_x u_x^2 e^{-\beta \frac{M\omega_x^2 u_x^2}{2}} \right] \left[\int du_y e^{-\beta \frac{M\omega_y^2 u_y^2}{2}} \right]}_{\substack{\text{prod. of 1 integrals of form of eq. (I.1)} \\ \text{and 1 integral of form of eq. (I.2)}}} \times
\end{aligned} \tag{I.6}$$

Thus we find for the MSD

$$\begin{aligned}
\langle u_x^2 \rangle_T &= \left[\frac{\beta\omega_x}{2\pi} \right] \left[\frac{\beta\omega_y}{2\pi} \right] \left[\frac{2\pi M}{\beta} \right] \left[\frac{\sqrt{2\pi}}{\sqrt{\beta}\sqrt{M\omega_y}} \right] \left[\frac{\sqrt{\pi}2^{3/2}}{2(\beta M\omega_x^2)^{3/2}} \right] \\
&= \left[\frac{\omega_x}{2\pi} \right] \left[\frac{\sqrt{2\pi}}{\sqrt{\beta}} \right] \left[\frac{\sqrt{2\pi}}{\sqrt{\beta}M\omega_x^3} \right] \\
&= \frac{1}{\beta M\omega_x^2}.
\end{aligned} \tag{I.7}$$

We see that the MSD along one cartesian coordinate scales as $1/\omega^2$. The full 2D-MSD reads

$$\langle \mathbf{u}_\perp^2 \rangle_T = \frac{k_B T}{M} \left(\frac{1}{\omega_x^2} + \frac{1}{\omega_y^2} \right). \tag{I.8}$$

Acta Universitatis Upsaliensis

Digital Comprehensive Summaries of Uppsala Dissertations from the Faculty of Science and Technology 2348

Editor: The Dean of the Faculty of Science and Technology

A doctoral dissertation from the Faculty of Science and Technology, Uppsala University, is usually a summary of a number of papers. A few copies of the complete dissertation are kept at major Swedish research libraries, while the summary alone is distributed internationally through the series Digital Comprehensive Summaries of Uppsala Dissertations from the Faculty of Science and Technology. (Prior to January, 2005, the series was published under the title "Comprehensive Summaries of Uppsala Dissertations from the Faculty of Science and Technology".)



Distribution: publications.uu.se
urn:nbn:se:uu:diva-517225

ACTA UNIVERSITATIS
UPSALIENSIS
2024